A Nonlinear Control Algorithm for Fuel Optimal Attitude Control Using Reactions Jets

by

Fermín Noel García

Bachelor of Science in Mechanical Engineering
Massachusetts Institute of Technology
May 1997

Submitted to the Department of Mechanical Engineering
in partial fulfillment of the requirements for the degree of

Master of Science in Mechanical Engineering

at the

MASSACHUSETTS INSTITUTE OF TECHNOLOGY

May 1998 [June 1998]

Author .....
Department of Mechanical Engineering
May 8, 1998

Certified by .....
David L. Trumper
Rockwell International Associate Professor of Mechanical Engineering
Thesis Supervisor

Certified by .....
Dr. Lawrence C. Ng
LLNL supervisor
Thesis Supervisor

Accepted by .....
Ain A. Sonin
Chairman, Department Committee on Graduate Students

A Nonlinear Control Algorithm for Fuel Optimal Attitude Control Using Reaction Jets

by

Fermín Noel García

Submitted to the Department of Mechanical Engineering
on May 8, 1998, in partial fulfillment of the
requirements for the degree of
Master of Science in Mechanical Engineering

Abstract

We present the analysis and design of a weighted nonlinear time-fuel optimal control algorithm for spacecraft attitude dynamics using on-off gas jets. In the development of a controller, we explore four control algorithms within a single-step control framework where the step is the fundamental update time of the digital controller. The benchmark controller is a basic pulse-width modulator (PWM) with a proportional derivative controller driving the feedback loop. The second is a standard rate-ledge controller (RLC) with full-on or full-off pulse commands, while the third varies the duration of the RLC pulse commands based on the location of the states in the phase plane. The RLC algorithm is shown to well-approximate a continuous-time weighted time-fuel optimal controller. The fourth control algorithm consists of a combination of the variable-pulse RLC algorithm and a tracking-fuel optimal controller that reduces the residual error relative to the latter algorithm.

Experimental data from a dynamic air-bearing testbed at Lawrence Livermore National Laboratory are used to compare the four control algorithms. The PWM scheme proves to be robust to disturbances and unmodeled dynamics and quite fast, but yields excessive fuel consumption from frequent switching. The standard RLC algorithm gives poor closed-loop performance in the presence of unmodeled dynamics and ends up being equally as fuel costly as the PWM scheme. The third algorithm, the RLC with variable pulses, significantly improves the transient and steady-state responses of the first two controllers. Via parameter tuning, we observe that this modified RLC gives excellent steady-state fuel consumption as well as reasonably fast settling times. The fourth algorithm, although more fuel efficient than the PWM and standard RLC controllers, is less efficient than the variable RLC algorithm. Matlab simulations of the four control algorithms studied are corroborated by these test results.

Thesis Supervisor: David L. Trumper
Title: Rockwell International Associate Professor of Mechanical Engineering

Thesis Supervisor: Dr. Lawrence C. Ng
Title: LLNL supervisor

Acknowledgments

First of all, I wish to express my sincerest gratitude and appreciation to Professor David Trumper. His level of commitment and involvement in this thesis has been truly outstanding. The numerous discussions we had on alternative attitude control systems were critical to completing this work. His support and guidance have been instrumental in making this research project both profoundly interesting and successful. I am also indebted to Dr. Lawrence Ng at Lawrence Livermore National Laboratory (LLNL) for his mentorship and counsel. Without his technical expertise and years of experience as a leader in the field, much of this work could not have been possible. His undying perseverance and optimism took this thesis to unimaginably new heights.

Many thanks goes to all my colleagues in the Microsatellite group at LLNL. I am extremely grateful to Dr. Arno Ledebuhr and Joe Kordas, program leader and Deputy of the *MicroSat* group, for their encouragement and financial support. I also would like to extend my appreciation to Jeff Robinson, Eric Breitfeller, and Bruce Wilson. It was a pleasure to absorb their technical expertise and their advice on improving the *MicroSat* control system. Their practical knowledge and intuition have contributed abundantly to this thesis. A special thanks also goes to Phani Nukala for the countless hours he spent answering my never-ending questions about quaternions. He is truly a great asset to LLNL. Also, Bob Langland deserves a special thanks for being a key person in helping me find the right research project for this thesis. To the guys in the Precision Motion Control Lab, it has been way too much fun. Thank you all for the advice and all the great humor during the thesis crunch. Good luck to all of you in your respective career paths.

To my dearest Liz, I thank for all the moral support throughout the years. Her advice on all aspects of life truly opened my eyes to new worlds. Finally, I cannot forget my parents Fermín and María García. They have been with me every step of the way and never lost faith in the day that I would see the light at the end of the tunnel. For this, I am forever indebted.

For my beloved parents

Contents

List of Figures

List of Tables

Chapter 1

Introduction

Future spacecraft missions will require very precise and stabilized pointing and tracking capabilites over at least a part of their mission. Given the simplicity, reliability, agility, and weight savings advantage of pulse-modulated actuation devices such as on-off reaction jets, it is clear that spacecraft can benefit from using this mode of propulsion. These devices, however, have two main drawbacks. First, their inherent nonlinearity results, at best, in coarse attitude control. Finer attitude control is possible only when more costly and complicated linear actuation is used in conjunction with the on-off devices. Secondly, the bang-bang control nature of reaction jets typically produces steady-state limit cycle behavior in the absence of disturbances; a behavior that yields excess steady-state fuel consumption. It is thus a significant engineering challenge to utilize pulsed devices on spacecraft for quick and accurate attitude control while at the same time minimizing the fuel expenditure caused by the limit cycle oscillations. In this thesis, the control "slack" associated with reaction jets is compensated for by using a "smart" computer algorithm which uses rate and navigation data from an on-board inertial measurement unit for feedback.

1.1 Background

The design of control systems using on-off thrusters has been a much studied problem. The nearly universal design of these control systems uses specific switching logic that

commands a thruster firing for some time duration. Typically the logic takes desired control torques that are generated by a separate controller (such as PD, PID, etc) and converts them into sequences of pulse-width-modulated burn. Most applications add a deadzone width to prevent the jet valves from responding to noise in the gyro. The switching logic is usually employed for a single set of thrusters which are assumed to primarily produce rigid-body, single-axis motion of the spacecraft. Thus, in three axes attitude control each axis is controlled independently of each other and not necessarily with the same switching logic. The key issue plaguing the performance of this conventional method is a fuel "expensive" limit cycle in which the jets are cycled on excessively.

Several approaches have been taken to improve the limit cycle performance of a pulse-width-modulated attitude control system. Clark [3] has devised a scheme to improve the fuel efficiency of a limit cycle by overcoming the effects of time delays in the control loop. Clark's "inhibitor" control law is shown to yield reductions in fuel expenditure compared to the conventional proportional-derivative controller. A similar study of limit cycle efficiency was carried out by Freeman [5]. Freeman, however, looked at the hardware effects more closely. In his paper, Freeman assigns a figure of merit for limit cycle efficiency and derives explicit relations for the influence of relay hysteresis, gyro sensor nonlinearities (friction, hysteresis, backlash, quantization, etc) and feedback gains on the limit cycle. Furthermore, he shows that the main bottlenecks in obtaining good limit cycle efficiency are the thruster-off time lags and the gyro non-idealities.

The fuel-optimal and weighted-time-fuel optimal attitude control for spacecraft utilizing on-off jets has also been explored as a means of improving the limit cycle behavior. Athans [1] published one of the first analyses of time-fuel optimal control of spacecraft maneuvers. The analysis defines a family of time and fuel optimal phase plane curves switching curves which have an associated control command; namely either full-on or full-off. The algorithm, however, is awkward and difficult to implement in a digital computer. White [21] also defines a set of switching curves in the phase plane but they are more easily implemented in a digital control setting. White [21]

demonstrates a design analogy between optimal time-fuel control and the conventional rate-ledge relay controller [4, 13, 19]. The latter controller and some modifications are studied in this thesis. Other nonconventional approaches taken include application of nonlinear sliding control and feedback linearization to achieve robustness and stability [18, 19, 9]. In fact, Lee and Cochran [9] combine both feedback linearization and sliding mode control in order to achieve robust optimal attitude control of pointing maneuvers. They use sliding mode control to solve time optimal maneuver problems without the need for the calculus of variations.

Prior to this large amount of research, many optimization techniques have been developed for optimal control problems based on classical techniques that make use of the calculus of variations. Rao gives a thorough presentation of these techniques and how they apply to optimal control problems [14]. In most practical applications, however, these techniques have limited scope since many real world problems involve discrete and/or nondifferentiable objective functions which cannot be readily treated with classical theory. Since exact analytical solutions for most real-world problems can not be found using variational calculus, numerical techniques are the only way to solve the optimal control problem. The two-point boundary-value (TPBV) problems are of the most common type. The advent of high-speed digital computers have brought about many efficient optimization routines for solving TPBV problems. Hull [8] gives an overview of some standard numerical integration schemes used to solve optimal control problems that are first converted into parameter optimization problems. Even though present-day numerical solvers for optimization problems are better and faster, the methods still tend to be computationally intensive, especially when handling constrained problems.

More recent methods are being developed that do not require numerical solution schemes [9, 21]. Instead, these methods tend to consist mainly of physically-motivated arguments. Weisenberg [20] presents a historical perspective as well as a comparative study of some physically motivated optimal attitude control approaches for spacecraft with reaction jets. From his survey of the literature, three general approaches to attitude control are identified:

1. Controller based control

2. Variable pulse-width control

3. Phase-plane control

Each of these has its benefit and downside and it is up to the designer to choose appropriately among them. The following section describes the approach taken in this thesis and its relation to the Weisenberg perspective.

1.2 Thesis Overview

In this paper, the fuel optimal attitude controller that is developed uses a combination of all three approaches mentioned in the prior section and as such can be considered a hybrid in the "Weisenberg" sense. A constrained parameter optimization fomulation, a variable pulse-width command strategy, and a multi-logic phase-plane are all used in developing the "smart" algorithm that simultaneously eliminates the inefficient limit-cycle behavior and yields precise pointing and tracking.

The control strategy taken in the design of the "smart" algorithm is as follows:

1. Separate phase-planes are designed for shaping the optimal transient and steady state behavior.

2. Transient phase-plane switching curves are designed to bring the spacecraft attitude within a pre-defined phase-plane region in a time-fuel optimal fashion consistent with pre-selected designer objectives. These switching curves bound the bang-off-bang control action where the jets are either on or off for some fraction of the control cycle. The rate-ledge-controller (RLC) serves as the basic phase plane for this analysis.

3. A tracking-fuel optimization problem with constraints on the control variables is formulated to determine the control variables (jet pulse and turn-on time) that will give accurate and fuel-efficient steady-state behavior.

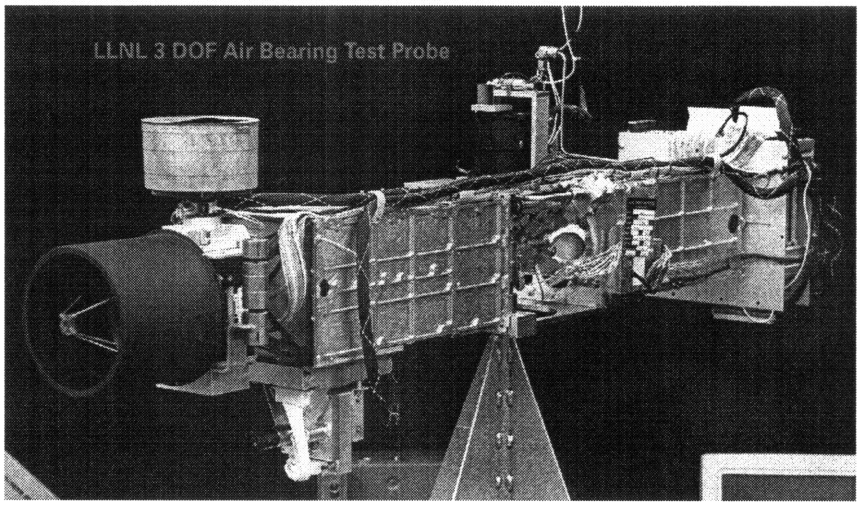

Figure 1-1: The dynamic air-bearing experimental setup at LLNL

4. Steady-state phase-plane switching curves, which represent the target region for the transient control logic, are determined from the constrained optimization solution for the optimal pulse-widths and turn-on times. A specific optimal pulse-width and turn-on time can be directly mapped to a corresponding switching curve in the steady-state phase-plane.

The nonlinear control law that results from the above methodologies is implemented in the dynamic air-bearing test setup at Lawrence Livermore National Laboratory that is shown in Figure 1-1. In addition to the nonlinear controller, a conventional proportional-derivative controller with a standard pulse-width-modulation scheme is also designed and implemented in the experimental setup of Figure 1-1.

1.3 Thesis Organization

Chapter 2 of this thesis derives a system model for the dynamics of a rigid spacecraft that serves as the basis for the control laws and discusses the design of a proportional-derivative (PD) controller for a linearized system model. The chapter also explains the conversion of a control torque to a jet burn of a certain duration via the concept of pulse-width-modulation. In Chapter 3, we briefly formulate the time-fuel optimal controller based on White's [21] study of the rate-ledge controller (RLC). This

standard RLC is then modified by adding short-pulse regions in the phase-plane. In Chapter 4, a tracking-fuel optimal control formulation and its corresponding phase-plane is fully developed. The real time implementation of the linear and nonlinear control algorithms and the description of the experimental setup is presented in Chapter 5. Chapter 6 compares and contrasts experimental and simulation results for all four controllers studied. In Chapter 7 we discuss conclusions and suggestions for further work. Appendix A discusses the formulation of the RLC from a continuous-time time-fuel optimal control formulation in more detail.

Chapter 2

Proportional Derivative Control

This chapter presents the development of a suitable model for the laboratory prototype vehicle and discusses the design of a proportional derivative (PD) controller with a pulse-width-modulating control scheme. We explain the overall control system viewpoint and how a nonlinear control element such as an on-off thruster affects the entire control system. It is shown that by treating the nonlinearity of on-off thrusters as a pulse-width-modulator, such as those found in power electronics, we can design a robust and stable attitude controller.

2.1 System model

Euler's equations of motion for the attitude dynamics of a rigid spacecraft with body axis at the center of mass are given as

$$\vec{\tau} = \dot{\vec{h}} + \vec{\omega} \times \vec{h} \tag{2.1}$$

$\vec{\tau}$ is the torque applied to the spacecraft about an arbitrary body axes, $\vec{\omega}$ is the vector of body rates with respect to the body axes, and $\vec{h}$ is the angular momentum vector with respect to the body axes.

The constitutive law governing rotational motion is given by

$$\vec{h} = \underline{\mathbf{I}}\,\vec{\omega} \tag{2.2}$$

where the matrix $\underline{\mathbf{I}}$ is the 3×3 inertia tensor for the spacecraft about its body axes. Equation (2.1) can be broken down into its components as follows:

$$\left.\begin{aligned} \tau_1 &= \dot{h}_1 + \omega_2 h_3 - \omega_3 h_2 \\ \tau_2 &= \dot{h}_2 + \omega_3 h_1 - \omega_1 h_3 \\ \tau_3 &= \dot{h}_3 + \omega_1 h_2 - \omega_2 h_1 \end{aligned}\right\} \tag{2.3}$$

If the body rates, $\vec{\omega}$, are assumed small, (2.1) and (2.3) simplify to

$$\vec{\tau} = \dot{\vec{h}} \tag{2.4}$$

in vector form. Using (2.2) and (2.3) and assuming the products of inertia, elements I_{ij}, to be small compared to the moments of inertia, elements I_{jj}, (2.3) simplifies further to

$$\left.\begin{aligned} \tau_1 &= I_{11}\,\dot{\omega}_1 \\ \tau_2 &= I_{22}\,\dot{\omega}_2 \\ \tau_3 &= I_{33}\,\dot{\omega}_3 \end{aligned}\right\} \tag{2.5}$$

Equation (2.5) is the decoupled linear approximation for the angular dynamics of a spacecraft. Furthermore, it is an accurate representation of the prototype vehicle in the laboratory as well as a very useful model for simple control analysis and will be adopted for the design of all the controllers examined in this thesis.

2.2 PD controller design

The design of a PD controller can be thought of as an addition of a first-order dynamics to the system of (2.5). In that we mean that a spring and a damper configuration

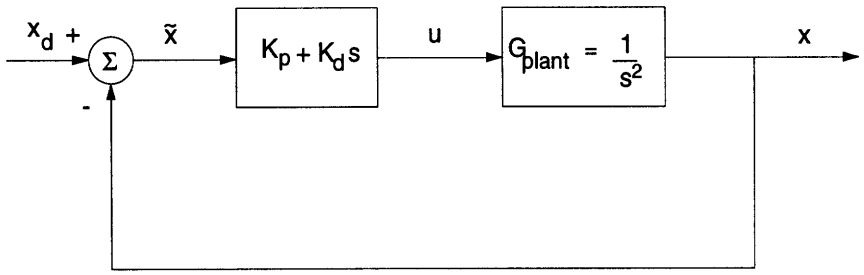

Figure 2-1: Conceptual schematic of a proportional derivative controller. The block diagram is shown here with the Laplace variable, s. In an actual implementation, differentiation of the state, x, to obtain the control input, u, is not done. Instead, the derivative term is either measured directly or estimated using an observer.

is added to the system so as to "tune" the closed-loop dynamics according to design specifications. This first order system can be expressed as

$$u = K_p\tilde{x} + K_d\dot{\tilde{x}} \tag{2.6}$$

where $\tilde{x}$ and $\dot{\tilde{x}}$ are the state errors, K_p is the proportional gain (the stiffness of a linear spring), K_d is the derivative gain (the damping constant of a linear damper), and u is the control input to the system. In our application we define the following specific variables

$$\left.\begin{aligned} \theta &= x \\ \omega &= \dot{x} \end{aligned}\right\} \tag{2.7}$$

where θ is the angular position and ω is the angular body rate. The state errors are determined by subtracting the states from the desired states. A block diagram for the PD controller is shown in Figure 2-1. Using the model described by (2.5) and (2.6) we can write the closed loop dynamics of the spacecraft as

$$\left.\begin{aligned} I_{11}\ddot{\theta}_1 + K_d\dot{\theta}_1 + K_p\theta_1 - K_p\theta_{d1} &= 0 \\ I_{22}\ddot{\theta}_2 + K_d\dot{\theta}_2 + K_p\theta_2 - K_p\theta_{d2} &= 0 \\ I_{33}\ddot{\theta}_3 + K_d\dot{\theta}_3 + K_p\theta_3 - K_p\theta_{d3} &= 0 \end{aligned}\right\} \tag{2.8}$$

where we assumed that the desired angular rates are zero and that θ_{di} are the desired attitudes in each axis (roll, pitch, yaw) respectively. The values for the gains K_p and K_d are then selected so as to shape the dynamics given by (2.8) and yield a desired behavior. The parameters that completely describe the behavior of this system are the damping ratio,ζ, and the bandwidth, ω_n. These are given as

$$\left.\begin{aligned} \omega_{ni} &= \sqrt{K_p/I_{ii}} \\ \zeta_i &= K_d/(2\omega_{ni}I_{ii}) \end{aligned}\right\} \tag{2.9}$$

where the $i's$ refer to the respective body axes. In the results chapter we discuss the choice of gains for the dynamic air-bearing prototype and examine the closed loop dynamics.

2.3 Pulse-Width-Modulation

The concept of pulse-width-modulation (PWM) is used readily in power electronics design. PWM is most commonly seen in power switching converters but the idea of applying it to spacecraft control is also quite common and useful. The central idea in using PWM in a spacecraft control scheme is the versatility it gives to the crude on-off thrusters during attitude maneuvers. For instance, since on-off jets can only provide a constant thrust level, the idea of controlling the length of the thrust duration allows refinement of the crudeness of the on-off actuation. The standard pulse-width-modulation scheme in spacecraft takes as input the control effort requested by a controller such as that of (2.6) and converts it into an equivalent thruster burn time. The conversion is done by approximating the average impulse over a control period instead of matching the required thrust level. A schematic of the pulse-width-modulation averaging scheme is shown in Figure 2-2. Note that the approximation is equivalent to forcing the areas under the two different thrusts to be equal if possible. Only when there is saturation in the commanded control effort ($u > F_{jet}$) can the the areas not be equal.

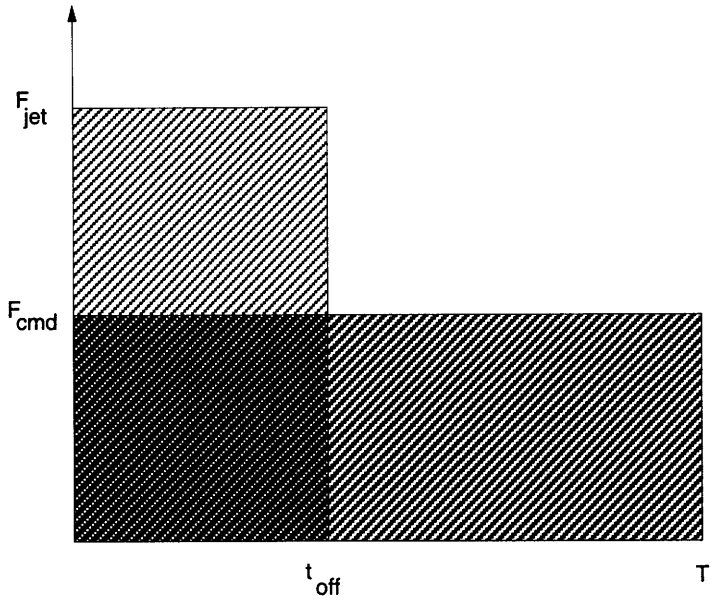

Figure 2-2: Impulse approximation using a pulse-width-modulator with duty cycle p/T.

2.3.1 Overview of PWM control

In this thesis, a PD controller is used to feed commands to a pulse-width-modulating scheme. The impulse approximation can be expressed as

$$F_{jet}\, p = uT \tag{2.10}$$

where F_{jet} is the constant thrust rate of the jet, p is the pulse-width of the thrust burn that is commanded, and T is the control period. Note that p is restricted to $0 \leq p \leq T$. This expression is equivalent to setting the areas in Figure 2-2 equal to each other. The duration of the burn, p, can be expressed as

$$p = \begin{cases} uT/F_{jet} & u < F_{jet} \\ T & \text{otherwise.} \end{cases} \tag{2.11}$$

Figure 2-3 shows this pulse-width modulation scheme graphically. Thus, the pulse-width-modulation scheme outputs a thruster burn as a linear function of the commanded control torque such that the impulse imparted upon the spacecraft is identical

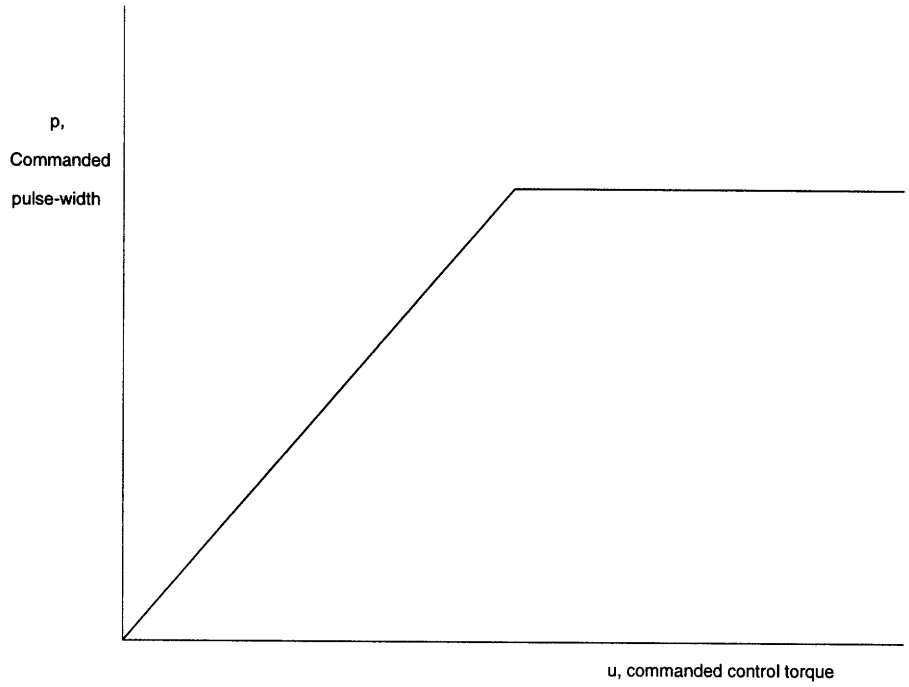

Figure 2-3: Commanded pulse width is plotted versus the commanded control effort from a proportional-derivative controller.

to the case where a full range of thrust levels exist. When the commanded control torque exceeds the maximum thrusting capability of the jets, then the thruster burn is always of duration T. Assuming the cycle time, T, is short enough, the PWM scheme has the effect of eliminating the relay characteristic of the reaction jets, but does nothing to fix the saturation problem. Another downside to the PWM control scheme is the existence of limit cycles in the system response of the spacecraft. This limit cycling directly results in poor fuel efficiency. In order to improve upon this performance we can set a deadzone limit to the pulse-width so that fuel is not consumed as frequently. With this deadzone included in the control, Figure 2-3 now appears as shown in Figure 2-4. This deadzone also prevents the PWM logic from reacting to sensor noise. This, however, only ameliorates the limit cycle but can not eliminate it without it sacrificing significant pointing accuracy and stability. Clark has [3] developed a somewhat more efficient PWM scheme that takes into account time delays in the system. We will forego using this control scheme because, as we will see further, the plant bandwidth is much lower than the controller bandwidth. This makes the effect of time delays almost insignificant for this study.

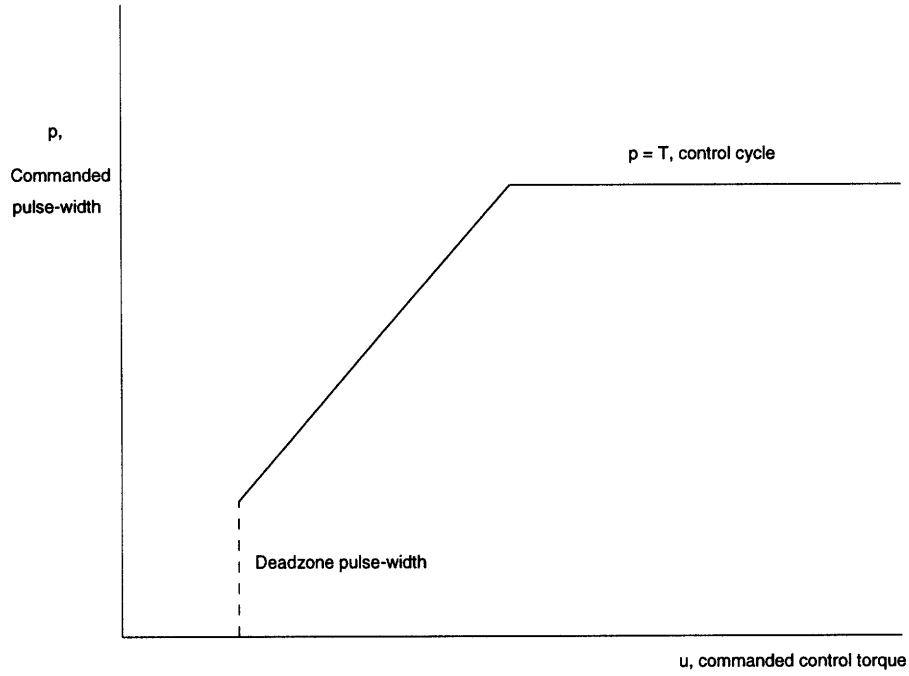

Figure 2-4: Schematic of PWM control with a deadzone. The addition of a deadzone reduces the frequency of limit cycling and improves fuel efficiency.

Chapter 3

Time-Fuel Optimal Controller Formulation

In this chapter we first formulate the continuous-time time-fuel TPBV problem for attitude dynamcis studied by White [21]. This formulation is followed by the presentation of the RLC control scheme and its analogy to the TPBV formulation. A modification of the standard RLC is presented and the associated system behavior is examined. The control scheme will presented for single axis control only since it can easlily be extended to all axes control by assuming decoupled rotations only. For more details on the ensuing analysis of the RLC refer to White [21] or Weisenberg [20].

3.1 Problem statement

Consider the well-known optimal weighted time-fuel problem with the performance index:

$$J = \int_0^{t_{final}} (\lambda + |u|)dt \tag{3.1}$$

where λ is a weighting factor and u is the applied control input. Increasing the weighting factor puts more emphasis on minimizing the time response (increasing system bandwidth) than on minimizing the control effort. The solution to this time-

fuel optimal control problem consists of finding a control effort u that minimizes (3.1) subject to the system dynamics. In solving this problem we use the same linear second-order dynamics developed in Chapter 2 for the PD controller. In the ensuing chapters, these dynamics are shown to well approximate the system in the laboratory.

3.2 Problem formulation

3.2.1 The two-point boundary-value problem (TPBV)

The two-point boundary-value problem as defined in the literature is the intermediate step in solving an optimal control problem. It is an intermediate step because it finds the solution to a coupled system of differential equations which is required in order to solve for a final differential equation that gives the optimal control u. The coupled differential equations are solved given two points or conditions: an initial system state and a final costate. The coupled differential equations are the system state equation and the costate equation. The differential equation in u is referred to as the stationarity equation. In this section we examine this two-point boundary-value problem in order to arrive at the time-fuel optimal switching control laws for attitude control of the linear dynamics of (2.5). For a more extensive explanation of the TPBV problem see Lewis [10].

The system model for the attitude dynamics of a single axis is given by

$$\left.\begin{aligned} \dot{\theta} &= \omega \\ \dot{\omega} &= u \end{aligned}\right\} \tag{3.2}$$

where θ is the angular position, ω is the body rate about the axis of rotation, and u is the control input. To accurately represent the characteristics of the reaction jets, it will be assumed that the control input can only take on the values $u = +1, -1, 0$. Note that (3.2) can be made identical to (2.5) if we express the control input as $u = \frac{\tau}{I}$, where τ is the control torque magnitude and I is the moment of inertia about the

body axis of rotation. The solution, u, thus has to satisfy (3.2) and simultaneously minimize the weighted time-fuel performance index of (3.1). Before solving the TPBV problem, the state, costate, and stationarity equation need to be defined. For this problem we choose the Hamiltonian to be

$$H = \lambda + |u| + p_1\dot{\theta} + p_2 u \tag{3.3}$$

where p_1 and p_2 are the corresponding costates. The costate and stationarity equations are defined as follows

$$\left.\begin{array}{rcll} \partial H/\partial x_i & = & p_i & \text{Costate equation} \\ \partial H/\partial p_i & = & x_i & \text{State equation} \end{array}\right\} \tag{3.4}$$

We can also rewrite the state equation in terms of the Hamiltonian as

$$\partial H/\partial u_i = 0 \quad \text{Stationarity equation} \tag{3.5}$$

where u_i in this expression is the i^{th} component of the control input vector. In the ensuing derivation, this subscript is left out because the variable u is a scalar control input, namely the commanded angular acceleration about an axis of interest. The TPBV problem consists of solving the expressions in (3.4) simultaneously. After having solved for the states and costates, the stationarity condition of (3.5) can now be solved. Solving the TPBV problem with the terminal constraint condition $\theta(t_{final}) = 0$ and using Pontryagin's minimum principle, White [21] explicitly shows that the optimal control trajectories are represented by

$$\left.\begin{array}{rcll} \theta & = & \frac{1}{2}\dot{\theta}^2 + c_1 & \text{u} = +1 \\ \theta & = & -\frac{1}{2}\dot{\theta}^2 + c_2 & \text{u} = \text{-1} \\ \theta & = & c_3 t + c_4 & \text{u} = 0 \end{array}\right\} \tag{3.6}$$

where c_1, c_2, c_3, and c_4 are all constants of integration that are determined from the

initial conditions $(\theta_0, \dot{\theta}_0)$. Likewise, the optimal switching curves are given by

$$\left.\begin{array}{lcll} \theta & = & \frac{\lambda+4}{2\lambda}\dot{\theta}^2 & \text{from u = +1 to u = 0} \\ \theta & = & -\frac{\lambda+4}{2\lambda}\dot{\theta}^2 & \text{from u = -1 to u = 0} \end{array}\right\} \tag{3.7}$$

Equation (3.7) represents the optimal locations on the phase plane for switching the control logic from $u = \pm 1$ to $u = 0$. Equation (3.6) describes the optimal way to approach the optimal switching curves of (3.7). A sketch of (3.6) and (3.7) is shown in Figure 3-1 for a given choice of $\lambda = 1$. This figure demonstrates how the time-fuel switching curves bound the region of zero-control-effort. The upper curve (the lower one when rotated into the fourth quadrant) is the optimal time switching curve. This curve maps out the time optimal trajectory of a state vector initially anywhere on the curve. The lower switching curve is the optimal fuel switching curve since it defines exactly when (or where in the state space point of view) the control effort is turned off. The trajectories starting at states A, B, and C show the optimal approach to the state space origin. At initial state A, the optimal control is $u = +1$ until hitting the positive fuel switching curve. At C, $u = -1$ is the optimal control and the switching curve is now the negative fuel curve. Moreover, the larger the time weight λ is the closer the fuel switching curve gets to the time optimal curve in Figure 3-1 (possibly putting state B in the $u = -1$ region). This increases the importance of achieving faster time responses and consequently making the zero-control-effort region smaller. This, of course, results in increased fuel consumption. The effect of varying λ on the time-fuel switching curves is shown in Figure 3-2.

If the terminal constraint on the position is deadband limited, a change of variable in the Hamiltonian optimality equations (3.4) and (3.5) can be done to shift the origin of the phase plane of Figure 3-1 from $\theta = 0$, $\dot{\theta} = 0$ to the region $\theta = \pm\theta_{db}$, $\dot{\theta} = 0$. Note that θ_{db}, in this case, is half the allowable deadzone width. The resultant phase plane configuration is shown in Figure 3-3. This phase plane describes the time-fuel optimal switching curves translated for a nonzero terminal condition for position. Since the goal of the control law is to maintain the attitude θ within the deadband,

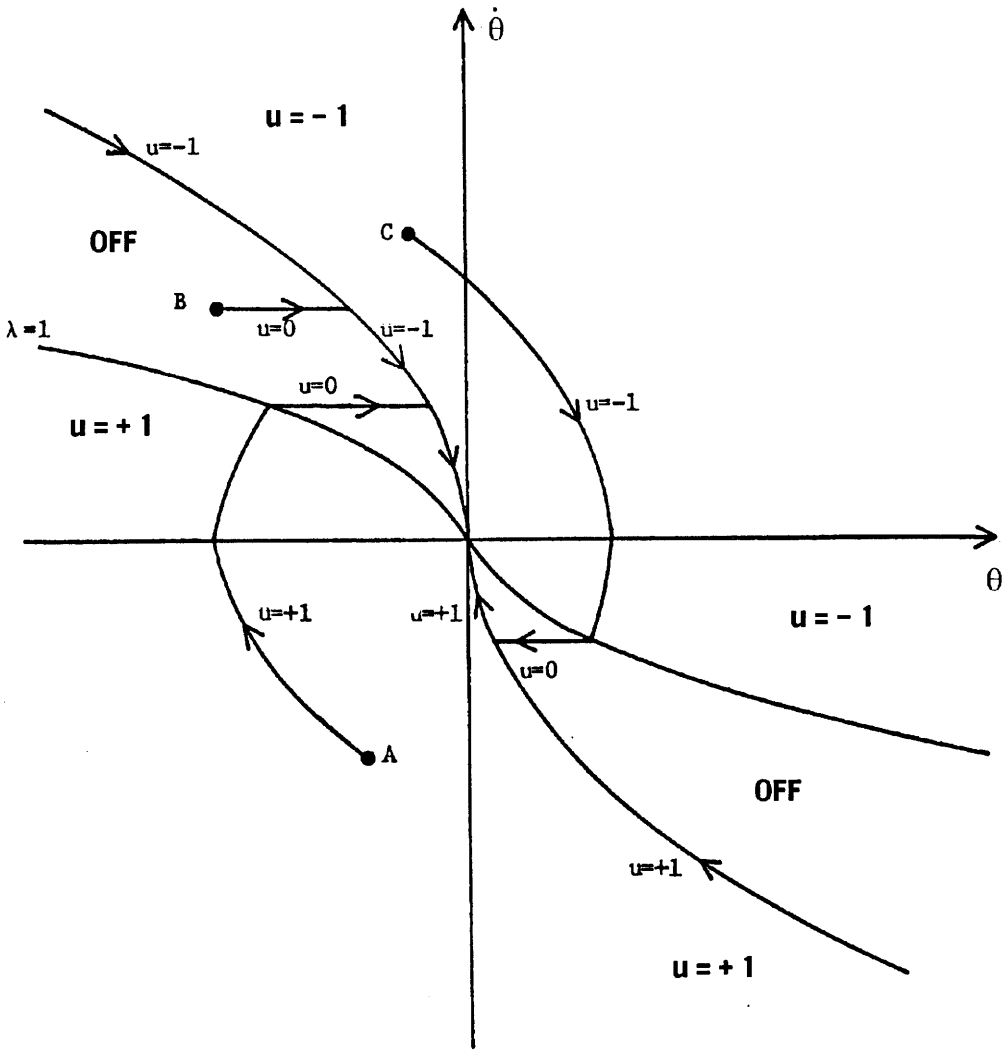

Figure 3-1: Time-fuel optimal switching curves with terminal constraint $|\theta_{final}| = 0$. This figure is adapted from Weisenberg [20].

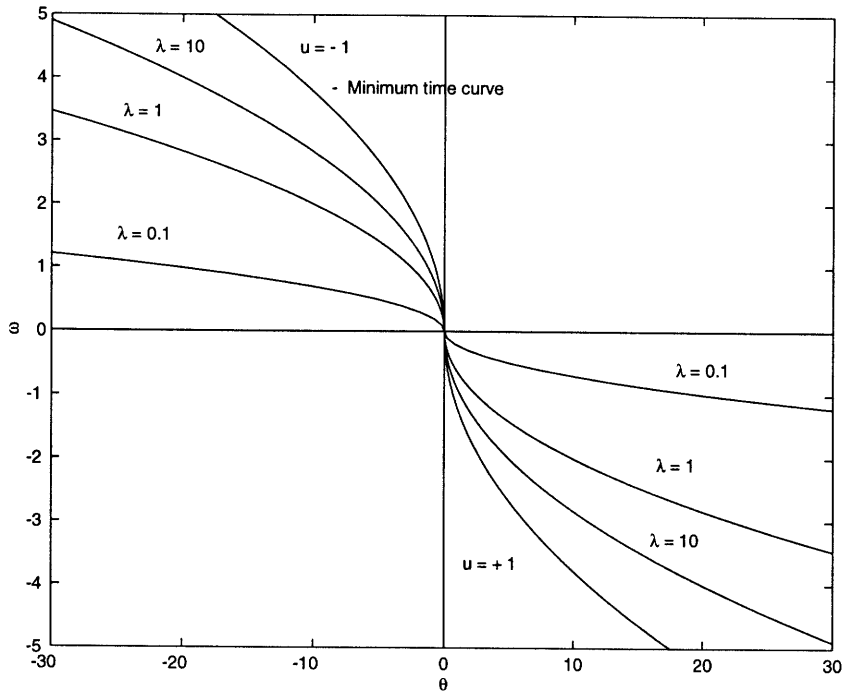

Figure 3-2: Figure of the time-fuel switching curves derived in continuous time for various choices of λ.

θ_{db}, the inner fuel switching curves of Figure 3-3 are ignored. These inner switching curves, B-F and C-G, correspond to a fixed value of λ and define when to switch from $u = \pm 1$ to $u = 0$. The internal minimum-time optimal switching curves, A-B-C and E-F-J, could also be omitted because any overshoot resulting from a $u = \pm 1$ control action drives the system out of the deadzone region. Hence, we are left with the phase plane, A-B-C and D-E-F, sketched in Figure 3-4 to represent optimal time-fuel attitude control with a predefined deadband. The remaining overlayed phase plane of Figure 3-4 is discussed in the next section.

Therefore, starting anywhere on the phase plane there is a specific curve that takes the initial state into the $u = 0$ deadband region, if not already there. While in the deadband region the spacecraft coasts if the rates are nonzero or remains very stable if the rates are nulled out. Floyd [4] has noted some problems with using the phase plane mentioned above in Figure 3-4 for discrete time control because of its inherent formulation in continuous time. The effects of the finite sampling time is seen to degrade the optimality of the control in Figure 3-1. White [21] discusses an approximate discrete time phase plane control logic to the parabolic switching curves

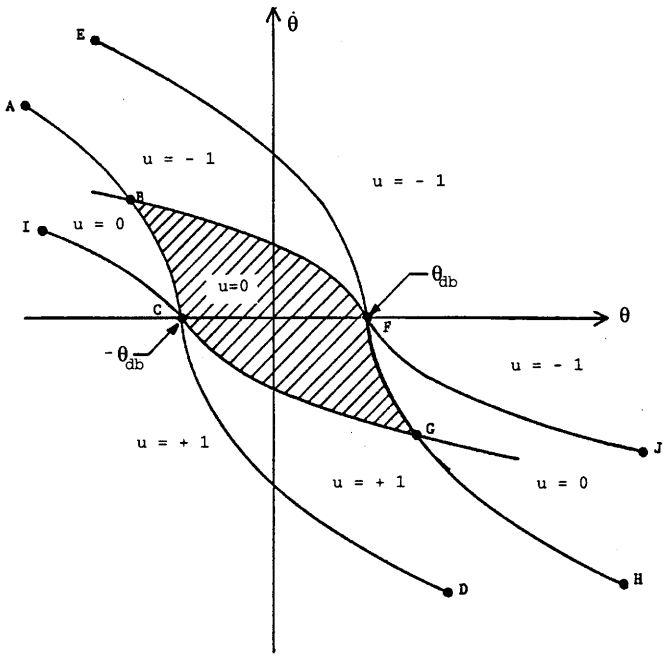

Figure 3-3: Time-fuel optimal switching curves in continuous time with deadband θ_{db}. This figure is adapted from Weisenberg [20].

depicted in Figure 3-4 that is simple to implement in a computer.

3.2.2 Standard RLC control scheme

The alternative time-fuel optimal phase plane studied by White is referred to as the rate-ledge-controller (RLC) in the spacecraft control literature and is shown in Figure 3-4 defined by the switching curves G-H-I-J and K-L-M-N. For more clarity, the RLC phase plane is presented separately in Figure 3-5. In White [21] the RLC is shown to well-approximate the continuous time optimal controller of the prior section (See Appendix A for the details of this approximation) in a least squares sense. This similarity is also observed in Figure 3-4. We will use and implement this phase plane in the dynamic air-bearing testbed. The RLC was initially designed for simulations of SkyLab and yielded good results. It is not as common a controller as are pulse-width-modulation schemes but, as will be seen in later chapters, it can improve the fuel efficiency of spacecraft significantly due to its rate nulling characteristics.

The RLC generally limits tight-pointing capabilities because of the prescence of

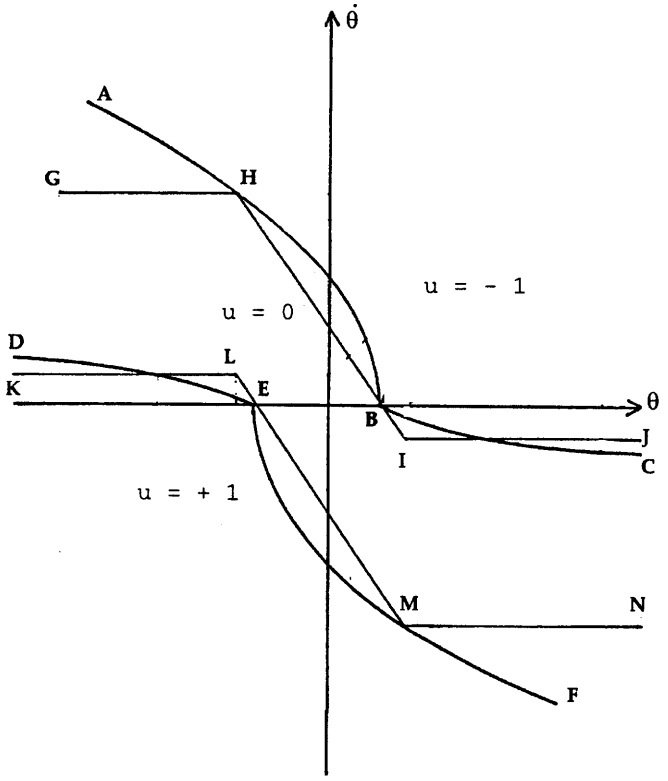

Figure 3-4: Time-fuel optimal switching curves in continuous time with deadband θ_{db}. Also shown overlayed is the rate-ledge-controller presented in section 3.2.2. This schematic is taken from White [21].

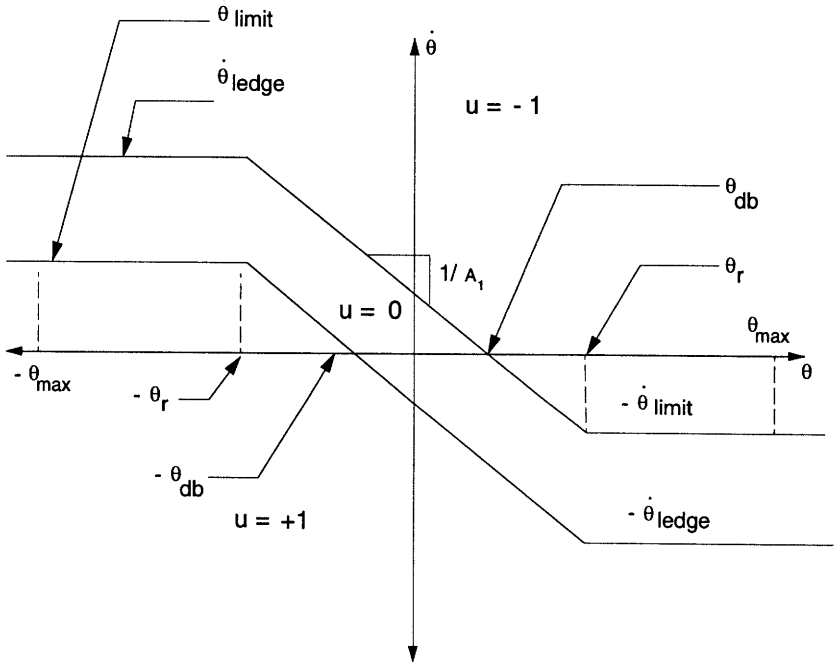

Figure 3-5: Rate-ledge controller with deadband θ_{db}.

a deadband. Thus, in this thesis the RLC is used to guide a spacecraft's attitude in a time-fuel optimal sense to a region where a more precise control system can take over. This control system is discussed in detail in the next chapter.

The system trajectories for the RLC with full-on pulse regions are shown in Figure 3-6. These curves are drawn for arbitrary initial conditions. Note also that the first and second quadrants of the phase plane primarily correspond to negative thrust and the remaining two quadrants have primarily positive thrust as required by the physics of the problem (see Figure 3-5 for the labeling of the thrust regions). Any state starting on a specific system curve shown will remain on that curve unless there is a disturbance. A close up of Figure 3-6 near the origin of the state space is shown in Figure 3-7. These curves are based on a discrete controller acting on a discretized model of (3.2). Therefore, these curves are exact only at the sampling instances ($T = 50$ ms), unlike the curves of Figure 3-1 which describe the continuous time behavior without regard to sampling effects. The effect of finite sampling time can be seen in the variable switching delays when passing through the switching boundaries.

3.2.3 RLC with short-pulse regions

In practice, the standard RLC control algorithm developed in section 3.2.2 could give poor steady-state performance. The main problem consists of large attitude excursions away from the state space origin due to the full-on cycles. Weisenberg [20] suggests an interesting modification to the standard RLC with full-on regions. The modification replaces the full-on regions near the origin with proportionately shorter pulse regions. This modified RLC phase plane is shown in Figure 3-8.

The different regions are chosen according to the characteristics of the specific system that is being controlled. The ± 3 regions, for instance, could correspond to a pulse-width lasting a full sampling period. Regions ± 1 and ± 2 are associated with shorter pulses. This controller has been known to give improved steady-state performance and thus increased fuel efficiency (refer to Weisenberg [20]). The behavior of the system under this control scheme is a clear improvement over the standard RLC

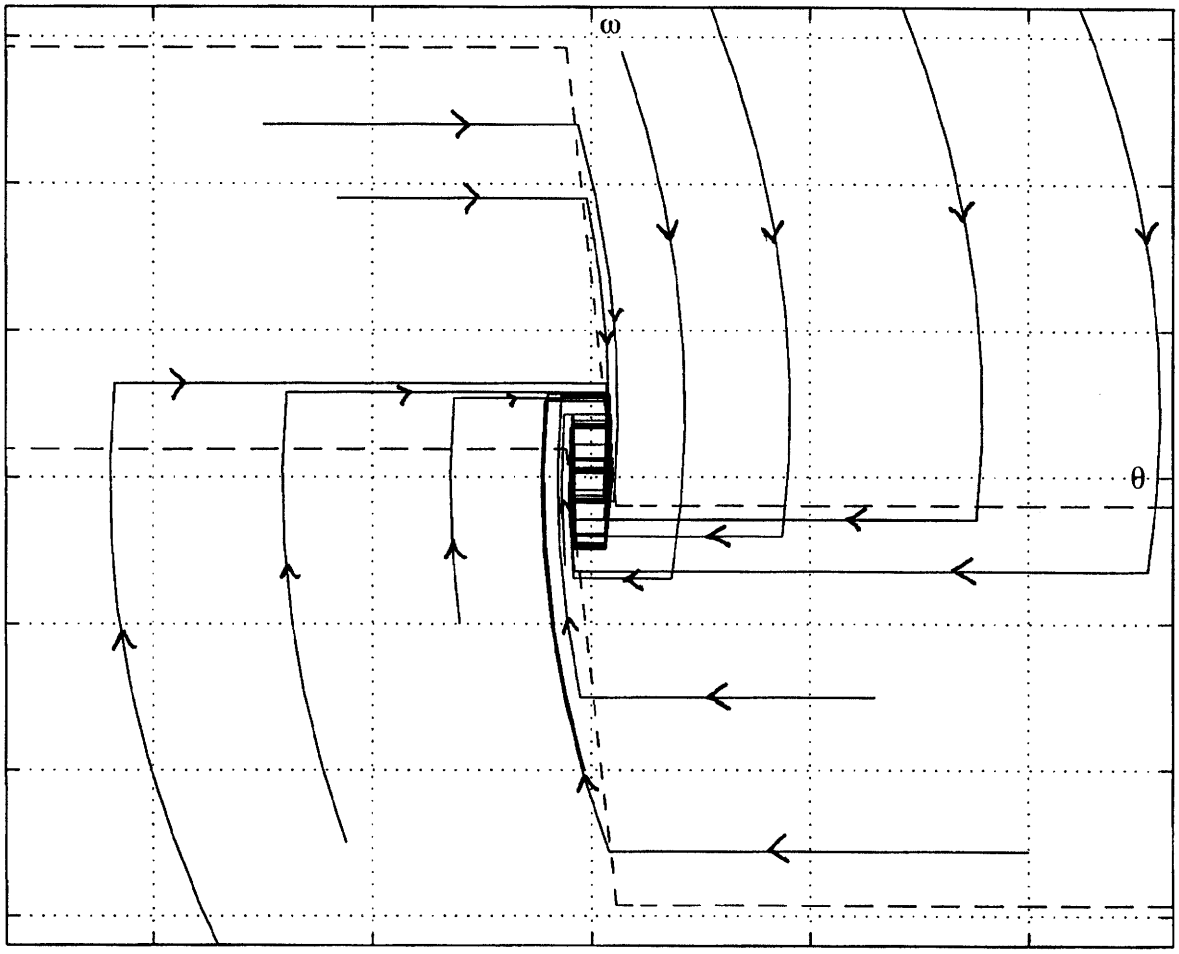

Figure 3-6: System trajectories using the standard RLC scheme when starting from arbitrary initial conditions. Dashed lines show switching curves. System is under discrete-time control with a sample rate of 20 Hz.

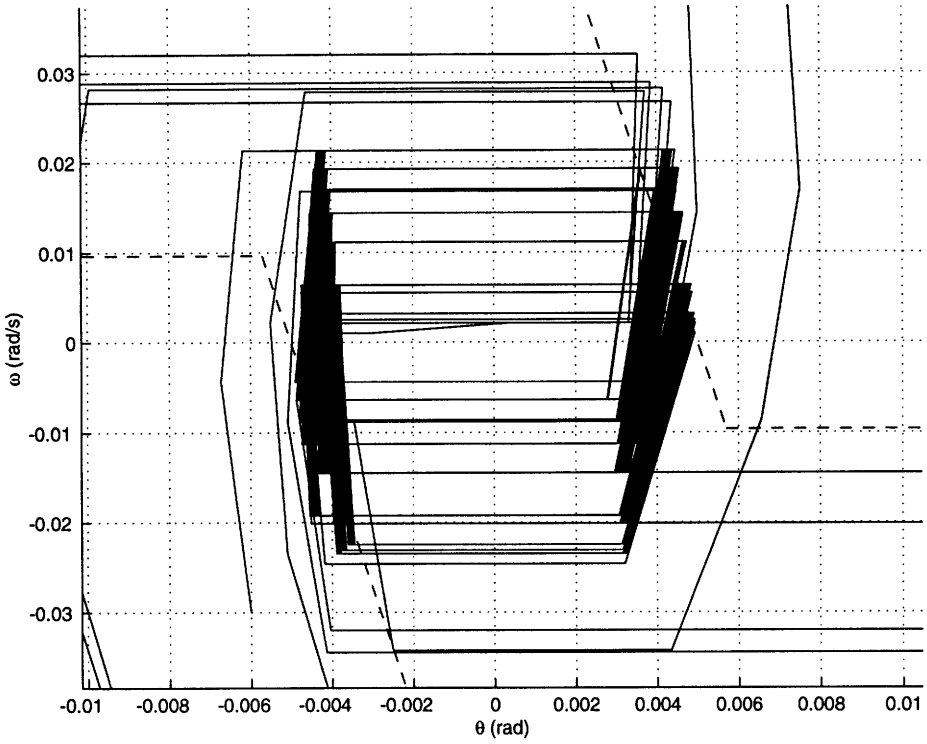

Figure 3-7: This figure zooms in near the origin of the phase plane of Figure 3-6 and clearly illustrates the limit cycle present when using the standard RLC control scheme. The system trajectories here start from arbitrary initial conditions. Dashed lines show the RLC switching curves. System is under discrete-time control with a sample rate of 20 Hz.

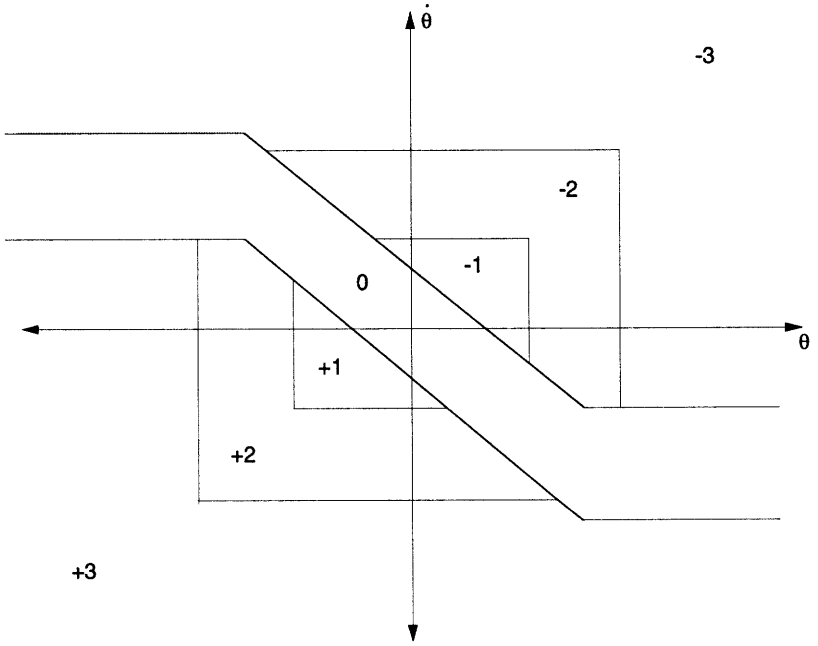

Figure 3-8: Rate-ledge controller with short-pulse regions near the origin.

as will be demonstrated.

The state trajectories for the RLC with short-pulse regions is given in Figure 3-9. These trajectories show the response of the system to a commanded pulse of width equal to one full control cycle, half the control cycle, or the minimum allowable pulse width. The abrupt changes in curvature of the system curves are caused by passing through to a different pulse region. Note that the curves look very similar to the curves in Figure 3-6 after they pass through the discontinuous pulse region. This makes sense since the system model is identical except for the magnitude of the control pulse that is exerted. As a result the RLC with short pulses causes longer system response but can significantly reduce the excessive limit cycle behavior seen in the standard RLC case. This improved response is shown more clearly in Figure 3-10.

3.3 Summary of RLC design

The standard RLC of Figure 3-5 is characterized by three parameters chosen by the designer to represent a desired time-fuel weighting. The parameters are θ_{db}, θ_{max}, and λ: the attitude deadband, maximum attitude command desired, and the time-fuel weighting factor of (3.1), respectively. The first two parameters can be directly described using the schematic for the standard RLC phase plane in Figure 3-5. The third parameter, λ, directly influences the size of the zero-control-effort region. The larger this parameter is, the narrower the zero-control-effort region becomes (Refer to Figure 3-11 for effect of λ on the shape of the RLC phase plane). With the selection of these parameters an equivalent RLC can be constructed that is analogous to the continuous time minimum time-fuel control problem with a time weighting of λ (Appendix A describes in detail the determination of the RLC parameters).

The RLC control scheme can be implemented in software by viewing it from a block-diagram perspective. A schematic of the block diagram equivalent of the RLC is shown in Figure 3-12. Note that this block diagram implements the RLC explained in the previous section because it limits the output, θ, to θ_r and then also limits

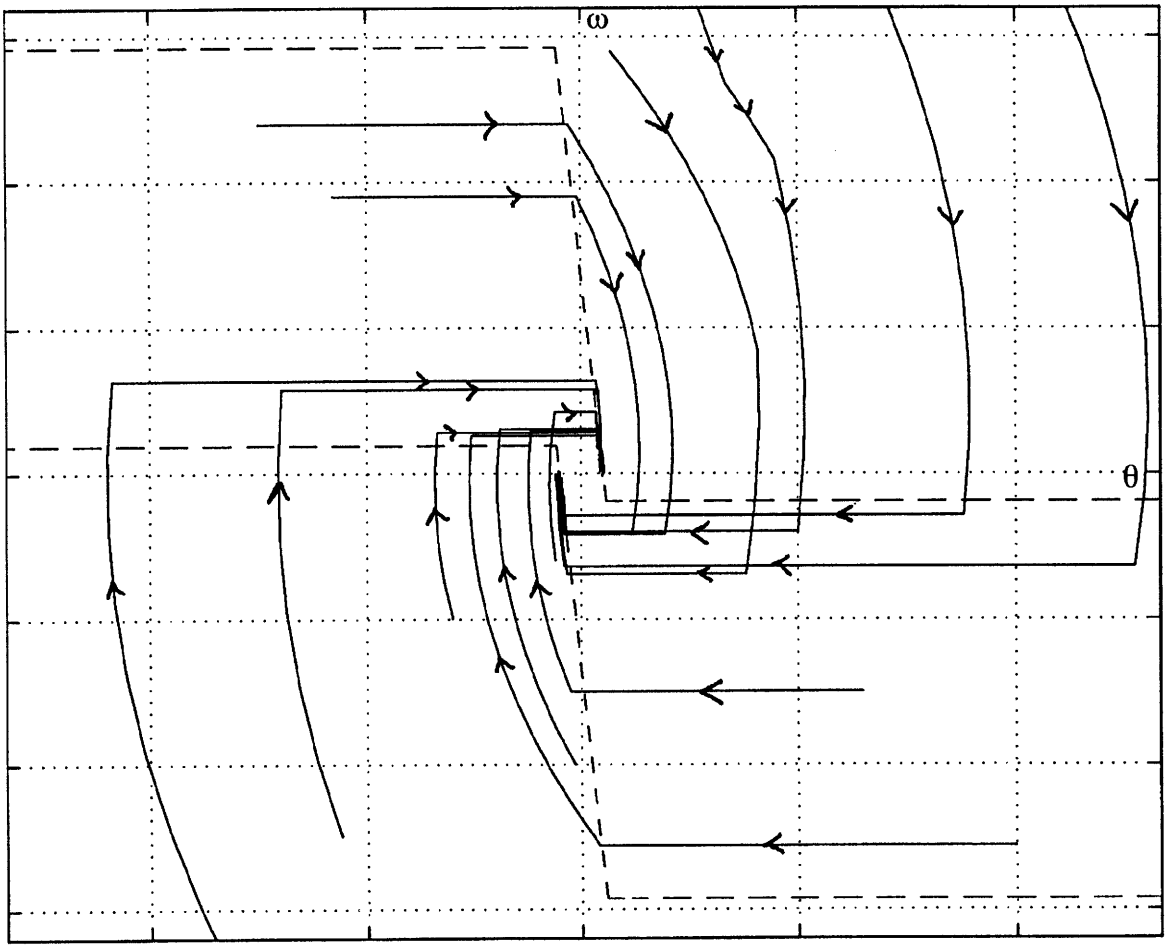

Figure 3-9: The system trajectories for the RLC with short-pulse regions when starting at an arbitrary initial state. Dashed lines show switching curves. System is under discrete-time control with a sample rate of 20 Hz.

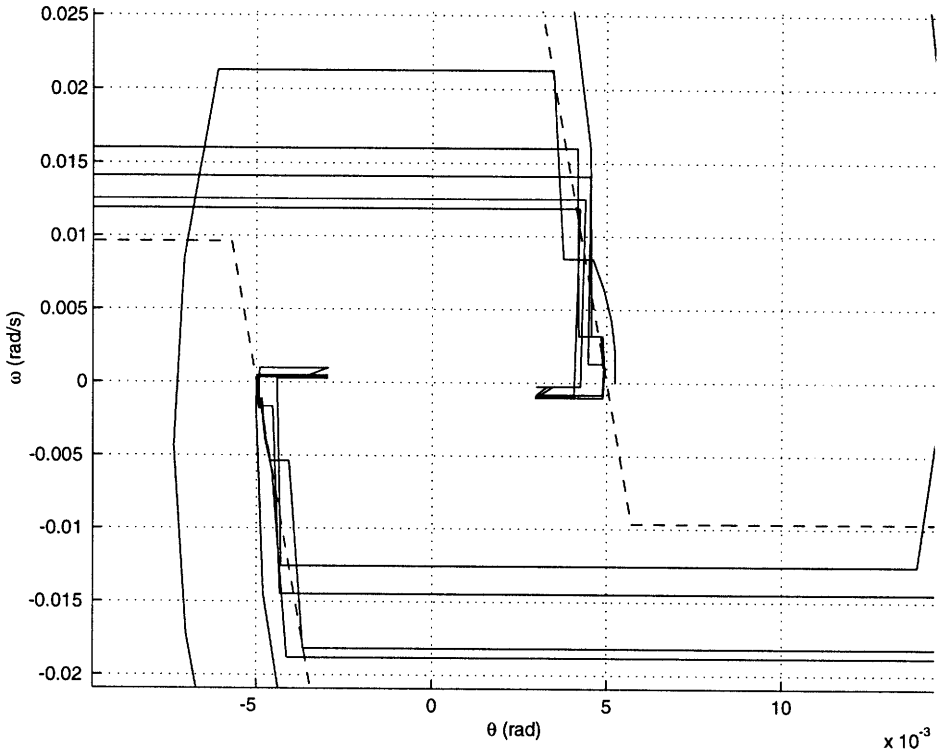

Figure 3-10: This figure zooms in near the origin of the phase plane of Figure 3-9 and clearly illustrates improved steady state performance when using the short-pulse RLC control scheme. The system trajectories here also start from arbitrary initial conditions. Dashed lines show the RLC switching curves. System is under discrete-time control with a sample rate of 20 Hz.

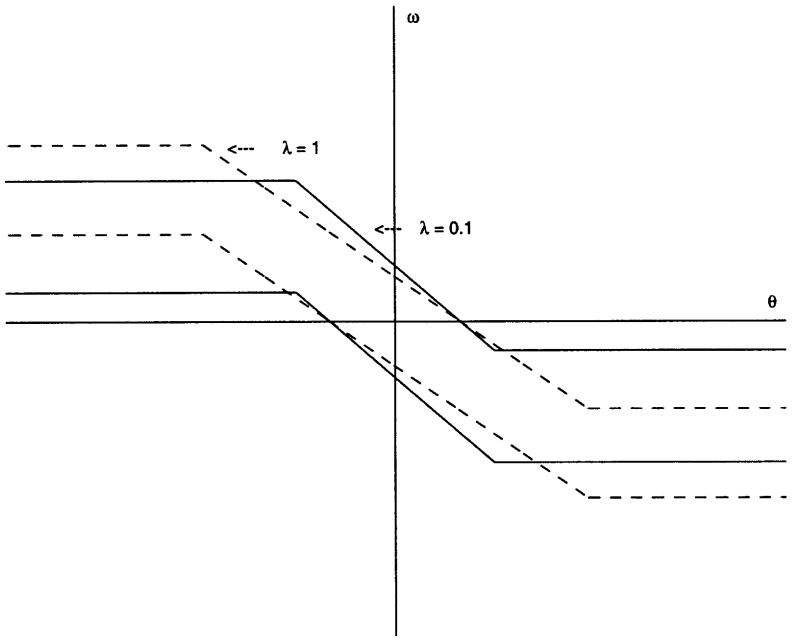

Figure 3-11: Schematic of standard RLC showing the effect of the time weighting parameter, λ, on the phase plane shape. Note that the phase plane in dashed lines has a tenfold larger value of λ than the other phase plane, and thus is the less fuel efficient. The phase plane corresponding to the smaller λ has a wider zero-control-effort region and a greater difference between the ledge values, $\dot{\theta}_{limit}$ and $\dot{\theta}_{ledge}$. The slope of the deadband lines, $1/A_1$, also decreases as λ increases.

the error signal to stay within the deadzone. The term A_1 serves as the rate gain term that influences the rate dynamics. A larger A_1 gives more emphasis to the rate component of the error signal thereby increasing the possibility for more frequent on-times. In the RLC phase plane, the same increase in A_1 reduces the slope of the lines bounding the $u = 0$ region (see Appendix A for details) and thus increases the size of the $u = \pm 1$ regions. The increase in the size of the $u = \pm 1$ region in the RLC clearly produces more frequent pulsing from the jets.

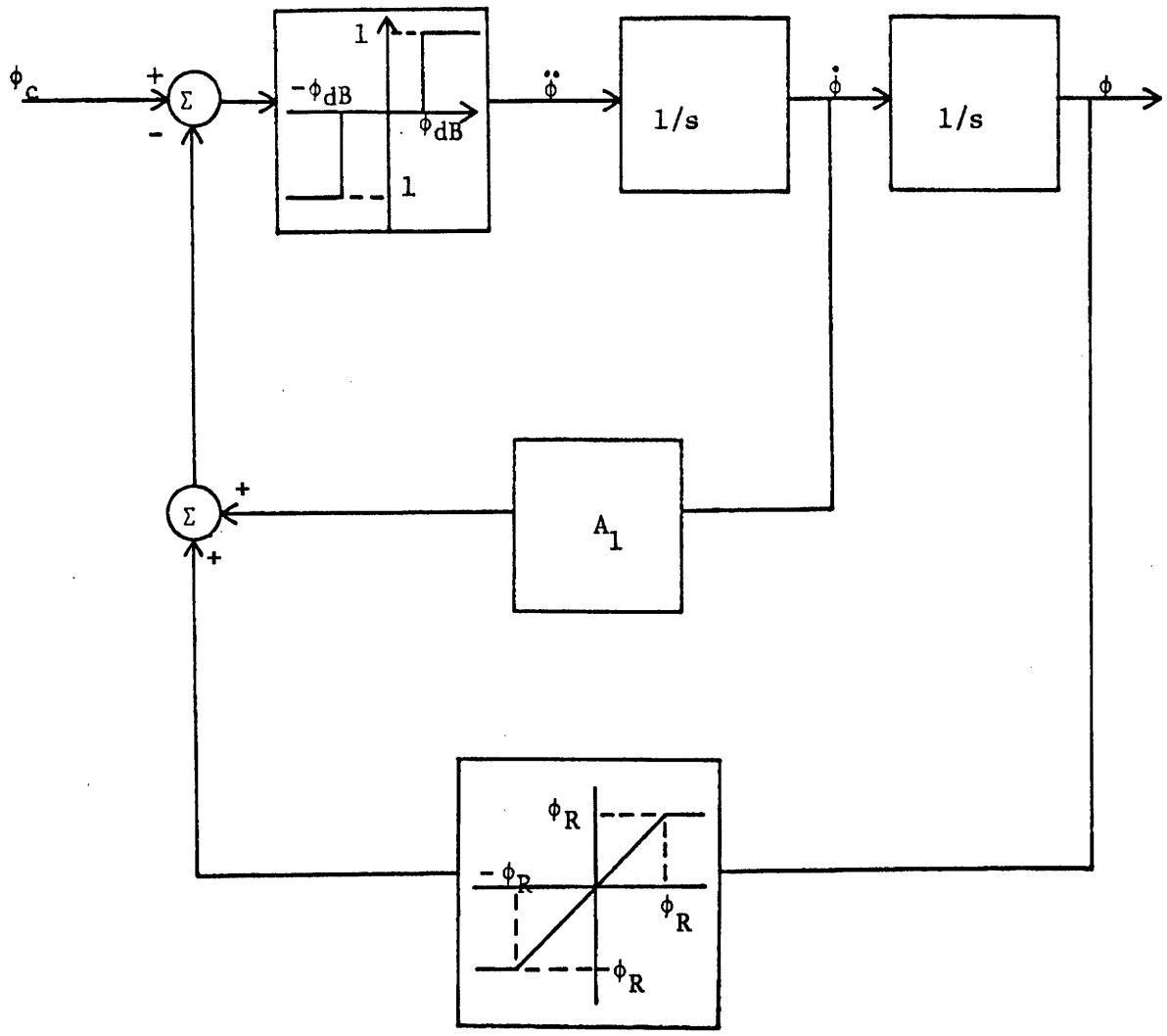

Figure 3-12: Single-axis RLC control system. This schematic is implemented in the laboratory computer for the control of the dynamic air-bearing prototype. The variable ϕ corresponds to θ defined thoughout this chapter. This schematic is taken from Weisenberg [20].

Chapter 4

Tracking-Fuel Optimal Controller Formulation

In this chapter we present the formulation of the tracking-fuel optimal controller used during steady-state attitude control [1]. The principal role of this controller is to refine the pointing capability of the RLC control scheme. The RLC control scheme can drive the attitude errors close to zero, depending on the size of the deadband chosen, but for an extremely tight pointing accuracy of less than 1 mrad (0.058^o) a more refined algorithm such as the tracking-fuel formulation is required. In simulation, the tracking-fuel controller can null out attitude errors as small as 5×10^{-4} rad while the RLC can only tighten the pointing to about $1 - 5$ mrad. Refer to Chapter 6 for simulations of this control algorithm and comparisons with the RLC scheme. At the end of the chapter a phase plane viewpoint of this tracking-fuel formulation is presented and it is related to the optimal control variables defined.

4.1 Model refinement

The model for the attitude/rate dynamics of a jet pulsed spacecraft can be refined to include the nonlinear characteristics of on-off reaction jet actuation. The decoupled

[1] The fundamental ideas that make up the core of this chapter have been inspired by Dr. Lawrence Ng.

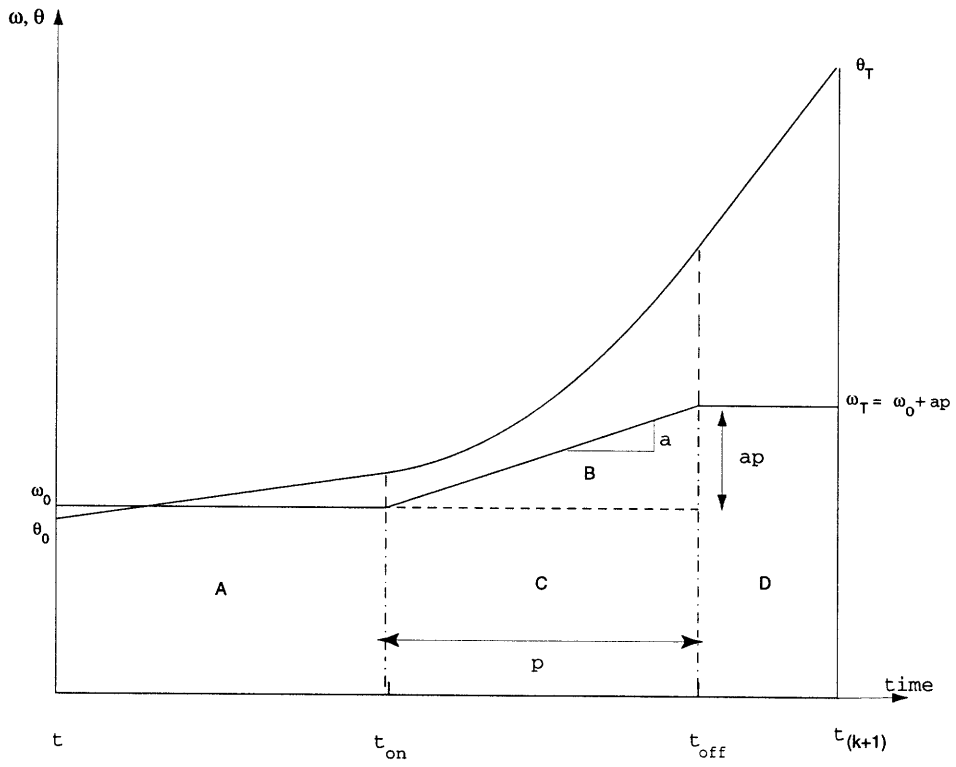

Figure 4-1: Schematic of the control cycle and description of intersample behavior of spacecraft attitude and rate

linear approximation, (2.5), for the angular dynamics of a spacecraft is still considered in developing this new model, but the nonlinearity of the relay behavior of the jets are now accounted for. Thus, the new model is inherently nonlinear. In this thesis we choose to derive this model directly in discrete-time so as to remain in the digital control domain entirely. The model can be described most clearly with reference to the schematic of Figure 4-1. From this schematic the dynamics can be described by looking at the effect of a thruster burn of magnitude a and duration p started at the instant t_{on} on the current attitude θ_o and rate ω_o. Note that the states are sampled every T seconds, but it is assumed that the burn can be started anywhere inside this time interval.

We can graphically determine the discrete-time relations for θ and ω from Figure 4-1 by noting that the change in rate over the sampling period is just the area under the pulse width of burn magnitude a while the change in angular position is the area under the rate curve shaped by the pulse width. This observation is valid since the value of a represents the angular acceleration of the spacecraft. This acceleration is

a known quantity and can be expressed using the linear uncoupled model of (2.5) as

$$a_i = \tau_i / I_{ii} \tag{4.1}$$

where the indices refer to the specific axis that is being considered.

Calculating the area under the acceleration curve (or under the pulse width burn) is fairly straightforward since it is nothing but the area of a rectangle with width p and height a. This area, ap, then represents the change in rate caused by a thrust of p time units long with a torque magnitude of $I_{ii}a_i$. Accounting for a nonzero initial condition of ω_o, the total change in rate after one control cycle is $\omega_{tot} = \omega_o + ap$. The change in position is the total area under the rate curve in Figure 4-1. This is calculated by splitting the entire region into four simple-shaped regions: A,B,C,D. Regions A, C, and D are all rectangles with areas $\omega_o\, t_{on}$, $\omega_o\, p$, and $(\omega_o + ap)(T - t_{on} - p)$ respectively. Region B is a triangle with area $\frac{1}{2}ap^2$. Assuming an initial condition of θ_o, the total change in angular position after one control cycle of length T is then given by $\theta_o + \omega_o T - \frac{1}{2}\, ap^2 + ap(T - t_{on})$. This expression is found by adding the initial angular position to the angular position change brought about by the coast-pulse-coast behavior (total area under the rate curve). Thus, the nonlinear discrete time model for the linear uncoupled angular dynamics with nonlinear actuation is

$$\theta_{k+1} = \theta_k + \omega_k T - \frac{1}{2}ap^2 + ap(T - t_{on}) \tag{4.2}$$

$$\omega_{k+1} = \omega_k + ap \tag{4.3}$$

where θ is the spacecraft angular position, ω is the body rate about a single axis, a is the fixed angular acceleration of the spacecraft, t_{on} is the time in the control cycle when a jet is commanded on, and p is the length of time that the jet is left on. These equations apply to each of the three body axes. It should be noted that the new system model derived has two control parameters (t_{on} and p) per axis and as a result allows an extra degree of flexibility in the control scheme.

4.2 Tracking-Fuel Optimal Control Formulation

The tracking-fuel optimal control problem can thus be stated as follows: Determine the control vector $\mathbf{u}$ that drives the system states $\{\theta, \omega\}$ described by (4.2) and (4.3) from a given initial condition $\{\theta_0, \omega_0\}$ to a specified final condition $\{\theta_f, \omega_f\}$ within a single control cycle of duration T while minimizing the performance index

$$J = (\theta_d - \theta_f)^2 + k(\omega_d - \omega_f)^2 \tag{4.4}$$

subject to the system dynamics of (4.2) and (4.3). In (4.4), θ_d and ω_d are the desired final states.

The quadratic cost function of (4.4) is selected for its simplicity and its accurate representation of the performance characteristics that are desired for fuel efficient and high precision spacecraft maneuvers. Each term in (4.4) serves a specific purpose. The minimization of the first term aims to drive the attitude error to zero while minimizing the second term aims to null out the body rates. Equation (4.4) hence plays a similar role to the role that integral control plays in a standard linear control law. The weighting parameter, k, defines the relative degree of importance the designer attributes to the two terms in the cost function. A smaller k will place more emphasis on minimizing the attitude error and in general give more precise pointing. Smaller values of k, however, can increase fuel consumption by introducing steady state limit cycling behavior caused by the presence of residual rates. Consequently, a large value of k will likely result in better fuel efficiency while degrading the pointing accuracy. No direct weight for the control effort u implemented in this cost function because in a system with a natural limit cycle the primary fuel inefficiencies arise from the presence of nonzero velocities. These nonzero velocities adversely affect the accuracy in the attitude position unless a control law is designed with these physics in mind. Thus, this optimal control formulation takes advantage of the actual physics causing the excessive fuel expenditure during attitude control by giving increased importance to nulling out the state errors.

The tracking-fuel optimal control problem as defined above, however, has some

additional constraints. These constraints pertain to the restrictions that the real time software imposes on the control variables. The constraints are listed below

$$\left.\begin{array}{rcl} t_{on} & \geq & \delta \\ t_{on}+p & \leq & T \end{array}\right\} \tag{4.5}$$

where T is the control cycle length and δ is the minimum reliable pulse possible in the hardware. Equation (4.5) is relevant because the real-time control architecture requires one "on" command and one "off" command during every control cycle if the logic calls for a control input. This stems directly from the fact that there is no pulse overlap allowed between control cycles. Furthermore, the control command must also be realizable in the physical sense (we require nonnegative time values). If the solution to the tracking-fuel optimal control problem satisfies the constraints of (4.5), it can be shown that this specific solution drives the attitude and rate below a specified tolerance during a single control cycle. This solution will be referred to as the "unconstrained" optimal solution for the remainder of this thesis. If the tracking-fuel control solution, however, does not satisfy (4.5) then additional conditions are placed on the optimization problem. This constrained problem and its solution is discussed further in section 4.2.2. The solution to the unconstrained optimal control problem is presented next in section 4.2.1.

4.2.1 Solving the unconstrained control problem

The tracking-fuel problem as stated in section 4.2 is a minimization problem with a set of constraints for the states θ and ω defined by the system dynamics of (4.2) and (4.3). This formulation can be transformed into an unconstrained minimization problem by substituting the system dynamics into the engineering objective function of (4.4). This substitution requires us to define the states as follows

$$\left.\begin{aligned} \theta_f &= \theta_{k+1} \\ \omega_f &= \omega_{k+1} \\ \theta_o &= \theta_k \\ \omega_o &= \omega_k \end{aligned}\right\} \tag{4.6}$$

Recall that we would like the terminal states, θ_f and ω_f, to be driven to the desired state commands θ_d and ω_d, respectively. At every control cycle, the commanded position is selected according to a desired attitude change, while the rate command is chosen to be zero. As mentioned already, the nulling out of body rates is the key requirement in minimizing the effect of the limit-cycle. Using (4.2), (4.3), (4.4), and (4.6) we can rewrite the objective function as

$$J = [\theta_d - \theta_o - \omega_o T + \frac{1}{2}p^2 - ap(T - t_{on})]^2 + k[\omega_d - \omega_o - ap]^2 \tag{4.7}$$

We can now use differential calculus to minimize (4.7) with respect to the control parameters. The necessary conditions for (4.7) to have a minimum are

$$\frac{\partial J}{\partial p} = 0 \tag{4.8}$$

and

$$\frac{\partial J}{\partial t_{on}} = 0 \tag{4.9}$$

Solving (4.8) and (4.9 gives the following expressions for the unconstrained optimal control parameters:

$$T_{on} = T - (\frac{P}{2} + \frac{\Delta\theta}{aP}) \tag{4.10}$$

and

$$P = \frac{\Delta\omega}{a} \tag{4.11}$$

where T_{on} and P are the optimal values of control variables t_{on} and p respectively,

and $\Delta\omega$ and $\Delta\theta$ are defined as

$$\left.\begin{aligned} \Delta\omega &= \omega_d - \omega_o \\ \Delta\theta &= \theta_d - \theta_o - \omega_o T \end{aligned}\right\} \tag{4.12}$$

The variable $\Delta\theta$ is the residual attitude error that accumulates if no corrective action is taken. Thus, the system starting from the initial states, θ_o and ω_o, will have a residual error in attitude of $\Delta\theta$ after one control cycle of length T. The variable, $\Delta\omega$, is just the error in the body rates. The control parameters T_{on} and P are truly optimal when they satisfy the real-time control constraints specified in (4.5). In this formulation, the sign of the acceleration, a, is switched depending on the required torque direction. The acceleration term in (4.10) and (4.11) is given a positive sign when the torque applied needs to increase the angular rate in a predefined direction, and a negative sign when the torque increases the angular rate in the opposing direction. Adopting this sign convention allows correct handling of the thrust direction in the prescence of positive values for the control parameters, T_{on} and P.

Since this optimal control approach assumes that the state error is driven to zero within a single pulse, the formulation can best be described as a single-step optimization problem. The single-step in this case is the fundamental control cycle T. Therefore, at every control cycle the optimal controller attempts to null out the rates with an effort depending on the magnitude of k. Floyd [4] has looked at single-step optimal control of flexible spacecraft and this serves as a good reference for a different perspective of the single-step optimization concept. The next section presents the solution to the tracking-fuel optimal control problem in situations when the state errors cannot be driven to zero in a single control cycle. For instance, when the rate command of $w_d = 0$ is unrealistic for the system to achieve in a single control cycle.

4.2.2 Solving the constrained control problem

It is very likely that the initial and final desired states are far enough from one another that the optimal control vector $\mathbf{u} = \{T_{on} \quad P\}^T$ solved for in (4.10) and (4.11) does not meet the constraints of (4.5). Given the the maximum thrust constraints and the physical construction of the spacecraft, the final state when using the optimal control is unreachable in one control cycle. We can still find an optimal solution $\mathbf{u}$ that keeps the control vector within the allowable limits specified in (4.5) and provides minimal tracking-fuel cost J. In order to do so, we need to convert the unallowable control actions to an allowable set of control actions satisfying (4.5) in a fuel efficient way.

The first step in defining allowable control actions is identifying the cases when the optimal control actions solved for in (4.10) and (4.11) are not allowable in the real-time software architecture. Given that there are two real-time software constraints, we naturally define each of these separately as a specific case. Thus, Case 1 will refer to the situations when the solution to (4.10) and (4.11) does not satisfy the first constraint in (4.5). Case 2 is the situation when the optimal control solutions in section 4.2.1 do not satisfy the second constraint of (4.5). In addition to these two cases, a third scenario is considered when the body rate error is zero and the attitude error is nonzero. This third case needs to be considered because here it is physically impossible for the attitude error to be driven to zero in one control cycle. In this case, at least two pulse are required for driving the state errors to zero.

For each of the three cases defined above an optimal control vector can be found if we assume optimal solutions of the form:

$$\left.\begin{array}{lllllll} T_{on}^* & = & 0 & \text{and} & P & = & P^* \quad \text{Case 1 solution} \\ T_{on}^* & = & T - P^* & \text{and} & P & = & P^* \quad \text{Case 2 solution} \\ T_{on}^* & = & 0 & \text{and} & P & = & P^* \quad \text{Case 3 solution} \end{array}\right\} \tag{4.13}$$

In this expression T_{on}^* and P^* refer to the optimal thruster on-time and pulse width, respectively, when the solutions to (4.10) and (4.11) do not satisfy the constraints of (4.5). Although the "best" optimal solution to the problem can not be

realized in one control cycle with the current real-time software system, a "second best" solution can be found easily by assuming the restrictions defined in (4.13). Substituting the restricted control parameters into (4.7) we arrive at the following three separate performance indexes for each constrained case respectively

$$\left.\begin{array}{lcll} J^* & = & [\Delta\theta + \frac{1}{2}aP^{*2} - aP^*T]^2 + k[\Delta\omega - aP^*]^2 & \text{Case 1} \\ J^* & = & [\Delta\theta - \frac{1}{2}aP^{*2}]^2 + k[\Delta\omega - aP^*]^2 & \text{Case 2} \\ J^* & = & [\Delta\theta + \frac{1}{2}aP^{*2} - aP^*T]^2 + k[aP^*]^2 & \text{Case 3} \end{array}\right\} \tag{4.14}$$

The constrained optimal pulse width, P^* , that minimizes (4.14) and simultaneously satisfies (4.5) can be determined by repeating the minimization problem. Using (4.8) and (4.9) with (4.14), differentiation gives the following three cubic equations in P^* for each of the three cases.

$$\left.\begin{array}{lcll} P^{*3} - 3TP^{*2} + 2(T^2 + \frac{\Delta\theta}{a} + k)P^{*2} - 2(\frac{\Delta\theta T + k\Delta\omega}{a}) & = & 0 & \text{Case 1} \\ P^{*3} + 2(k - \frac{\Delta\theta}{a})P^* - \frac{2k\Delta\omega}{a} & = & 0 & \text{Case 2} \\ P^{*3} - 3TP^{*2} + 2(T^2 + \frac{\Delta\theta}{a} + k)P^* - 2(\frac{\Delta\theta T}{a}) & = & 0 & \text{Case 3} \end{array}\right\} \tag{4.15}$$

Thus, solving for P^* in each of these equations gives a constrained optimal pulse width that when combined with the associated optimal on-time, T^*_{on} , gives the minimal value of J^*. Like in the unconstrained optimal formulation, the same sign convention for the acceleration is used in (4.15) to handle switching of the control effort direction. An optimal solution is thus always possible without the use of any numerical methods that solve the classical constrained optimization problems. Computer efficiency and design clarity is thus achieved.

In most typical pulse-width-modulated (PWM) control of spacecraft, t_{on} is set to zero to avoid complexity in the real-time control system. Thus, case 1 and case 3 of the constrained tracking-fuel formulation is equivalent to a PWM control system that is in some sense optimized. In its most general case, the formulation presented

in this section adds flexibility to the typical PWM control problem of Chapter 2 by adding an extra control input that can be specified and optimized.

4.3 The phase plane viewpoint

The tracking-fuel optimal control formulation developed in the last section can be viewed with a phase plane design perspective as is the RLC of Chapter 3. This viewpoint provides better insight into the optimal formulation and allows for more design clarity. In this section we derive the optimal state trajectories and map the different constraints defined in section 4.2.2 to regions in a phase plane.

To derive the tracking-fuel optimal state trajectories we recall the nonlinear discrete model of section 4.1 and the unconstrained controller of section 4.2.1. We can rewrite (4.2) and (4.3) as a single equation in $\Delta\theta$ and $\Delta\omega$ by substituting

$$aP = \Delta\omega \tag{4.16}$$

into (4.2). We then get

$$\theta_{k+1} - \theta_k = \omega_k T - \frac{\Delta\omega^2}{2a} + \Delta\omega(T - T_{on}) \tag{4.17}$$

If it is assumed that the state errors can be driven to zero in one control cycle then the state variables can be redefined according to (6.2).

$$\left.\begin{aligned} \theta_d &= \theta_{k+1} \\ \theta_o &= \theta_k \\ \omega_d &= \omega_{k+1} \\ \omega_o &= \omega_k \end{aligned}\right\} \tag{4.18}$$

These state errors can be thought of as belonging to the reachable state space, $\mathcal{R}_s$. Thus, $\mathcal{R}_s$ contains all the states ($\Delta\theta$, $\Delta\omega$) that can be driven to zero in a single thruster burn applied during one control cycle. Making the change of variable as

defined in (6.2) the resultant expression for the state equation is

$$\Delta\theta = \Delta\omega(T - T_{on}) - \frac{\Delta\omega^2}{2a} \tag{4.19}$$

This equation describes a set of parabolas in the phase space $\Delta\theta - \Delta\omega$ that describe the attitude dynamics of the spacecraft under optimal tracking-fuel control. These parabolas can be treated as sets of switching trajectories for different values of the control variables. The system trajectories are shown in Figure 4-2 for arbitrary thruster on-times, t_{on}. Also note that the curves drawn in Figure 4-2 have the correct physics. The correct physics requires the acceleration a and $\Delta\omega$ to be of the same sign (See Equation (4.13)). Consequently, a negative value for a, which implies that the states must be in the third or fourth quadrant, corresponds to the range $\Delta\omega < 0$. Likewise, a positive value of a corresponds to the range $\Delta\omega > 0$. A positive a is only needed when the states are in the top half of the state-space (quadrants I, II). The required pulse width, p, at any one point in the phase plane is extracted from Figure 4-2 by looking at the value of $\Delta\omega$ and substituting in (4.11). Note that this figure assumes no pulse-width constraints.

To gain a better understanding of these phase plane curves and the formulation of the constrained optimal control problem, the real time software limitations must be analyzed and viewed in the phase plane. First a bounding region must be calculated so that the region $\mathcal{R}_s$ is identified. The lower bound is straightforward to find since we know that all parabolas in (4.19) contain the origin of the state space. As a result, the value $T_{on} = 0$ defines the lower bounding parabola for the reachable region $\mathcal{R}_s$. This parabola is given by

$$\Delta\theta = \Delta\omega T - \Delta\omega^2/(2a) \tag{4.20}$$

Any state in the region to the right of the lower bounding parabola cannot be driven to the origin in a single pulse. This makes sense because the system parabolas that are further along the $\Delta\theta$ axis correspond to negative values of T_{on}. The upper bound on the region $\mathcal{R}_s$ is determined by maximizing $\Delta\theta$ with respect to $\Delta\omega$. This finds the maximum position error, $\Delta\theta_{max}$, as a function of the jet pulse ($\Delta\omega = aP$).

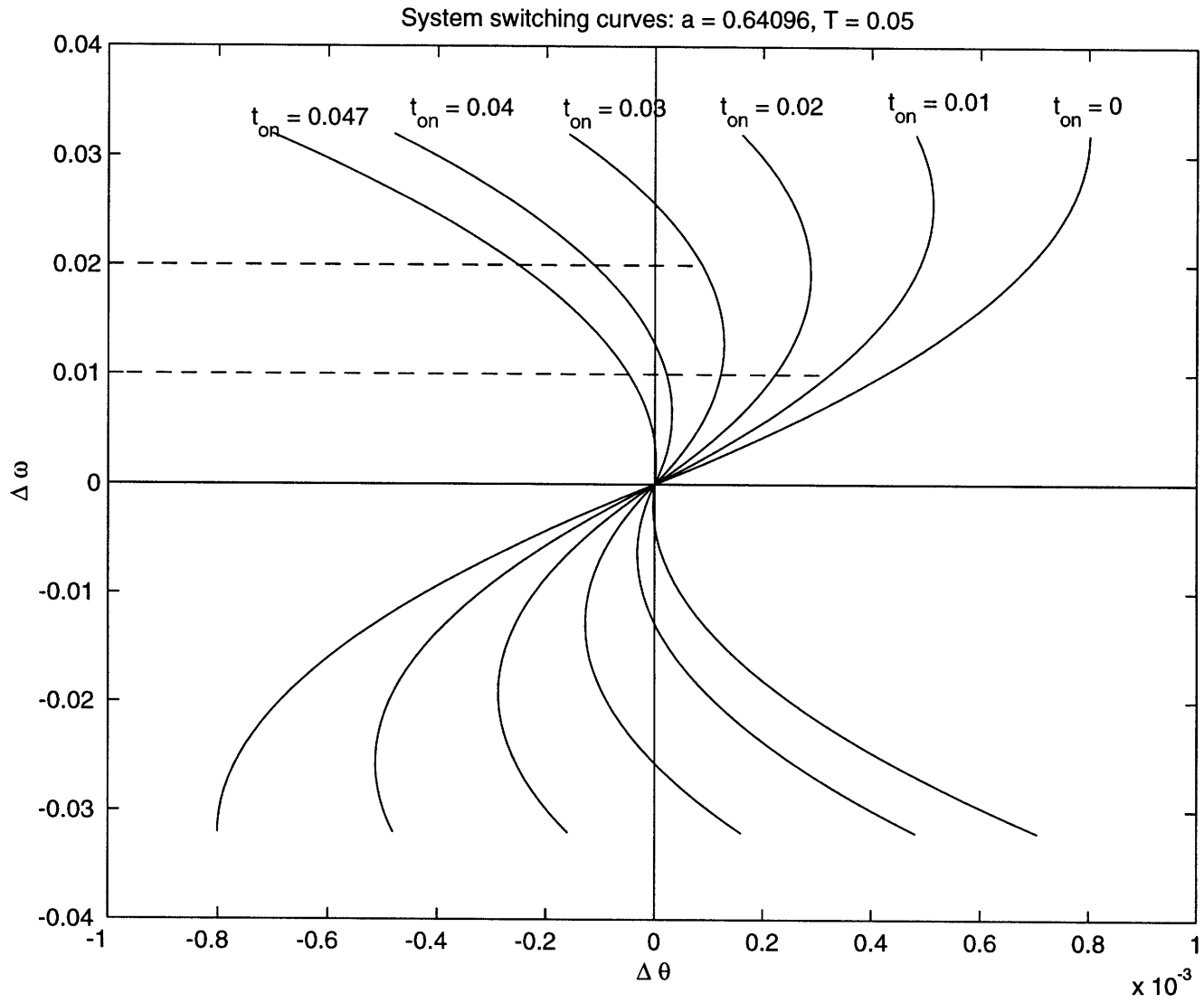

Figure 4-2: Phase plane schematic of nonlinear closed-loop tracking-fuel optimal control system. The curves describe the optimal state trajectories with assumption that a pulse width could overlap into subsequent control cycles (Case 2 restriction is no longer present). The t_{on} values above the system curves indicate the time within the control cycle when a pulse is started. These on-times are arbitrary and thus are not optimal values. They are selected to show the closed-loop behavior of the system if the above t_{on}'s are requested. A maximum value of $t_{on} = 0.047$ is used since the minimum pulse allowed by the actual control system is $p = 0.003$. The positive rate curves are a reflection of the lower curves about the line $y = -x$. The numbers used in the figure correspond to the dynamics of the vehicle yaw axis with angular acceleration of $a = 0.64096$ rad/s^2. The horizontal dashed lines in the figure are indicative of the pulse width commanded at that specific point in the phase plane. Recall that the commanded optimal pulse, p, is proportional to $\Delta\omega$ with a constant of proportionality a.

The upper bound is given by the solution to

$$\frac{\partial \Delta\theta}{\partial \Delta\omega} = 0 \tag{4.21}$$

Equation 4.21 is satisifed only when

$$\Delta\omega = a(T - Ton) \tag{4.22}$$

.

Using (4.19) and (4.22) the following relation can be derived

$$\Delta\theta_{max} = \frac{\Delta\omega^2}{2a} \tag{4.23}$$

Again because of the physics of the problem, the relevant sections of the parabolas described by (4.23) are the following

$$\left.\begin{array}{rcll} \Delta\theta_{max} & = & \Delta\omega^2/(2a) & \text{For } \Delta\omega \geq 0 \\ \Delta\theta_{max} & = & -\Delta\omega^2/(2a) & \text{For } \Delta\omega < 0 \end{array}\right\} \tag{4.24}$$

For the expressions in (4.24) the sign convention for the angular acceleration a is positive. Since $\Delta\omega$ is on the vertical axis, these parabolas more accurately describe the maximum allowable $\Delta\theta$ for a given state $\Delta\omega$ before escaping the upper bound on the region $\mathcal{R}_s$. Having determined the lower and upper bounds on the reachable region we now can completely define the region $\mathcal{R}_s$. This region is shown in Figure 4-3. Superimposing Figures 4-2 and 4-3 gives the phase plane of Figure 4-4.

A closer look at Figure 4-3 makes the constraints of (4.5) more apparent. As already pointed out, the region in the state space below the lower bound corresponds to a negative value of T_{on} and hence it is a mapping of Case 1 onto the phase plane. Case 2 which represents states that do not satisfy the second constraint of (4.5) can be mapped to the region directly above the upper bound parabola. The third case maps to the entire horizontal axis ($\Delta\omega = 0$). In addition to these three regions, care must also be taken to satisfy $T_{on} < T - \delta$, where δ is the minimum reliable pulse

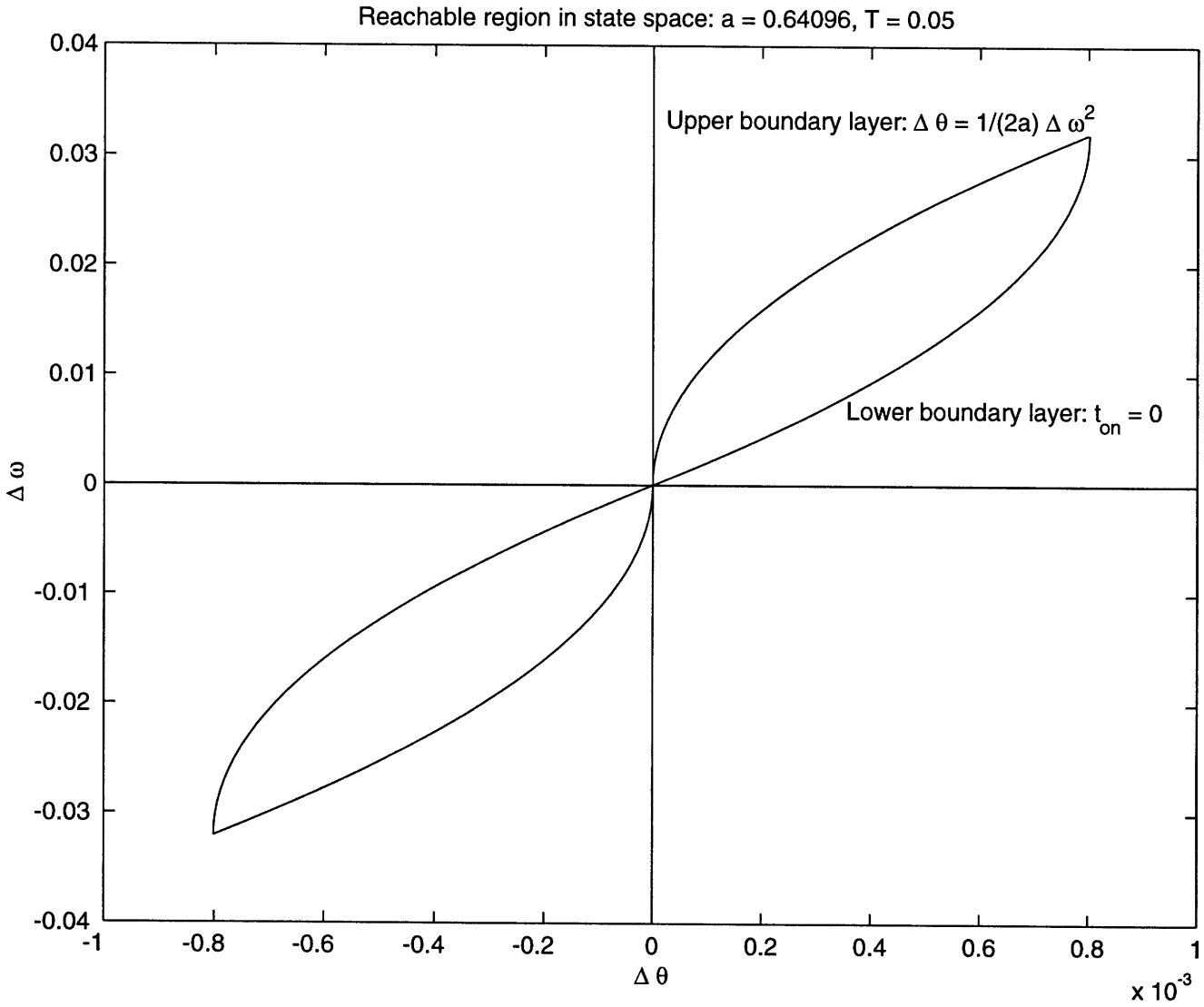

Figure 4-3: The reachable region $\mathcal{R}_s$ has a propeller shape. The boundary layers are also reflected about the line $y = -x$. Any initial state ($\Delta\theta$,$\Delta\omega$) in $\mathcal{R}_s$ can be driven to the origin within a single control cycle. The numbers used in the figure correspond to the yaw axis of the experimental vehicle.

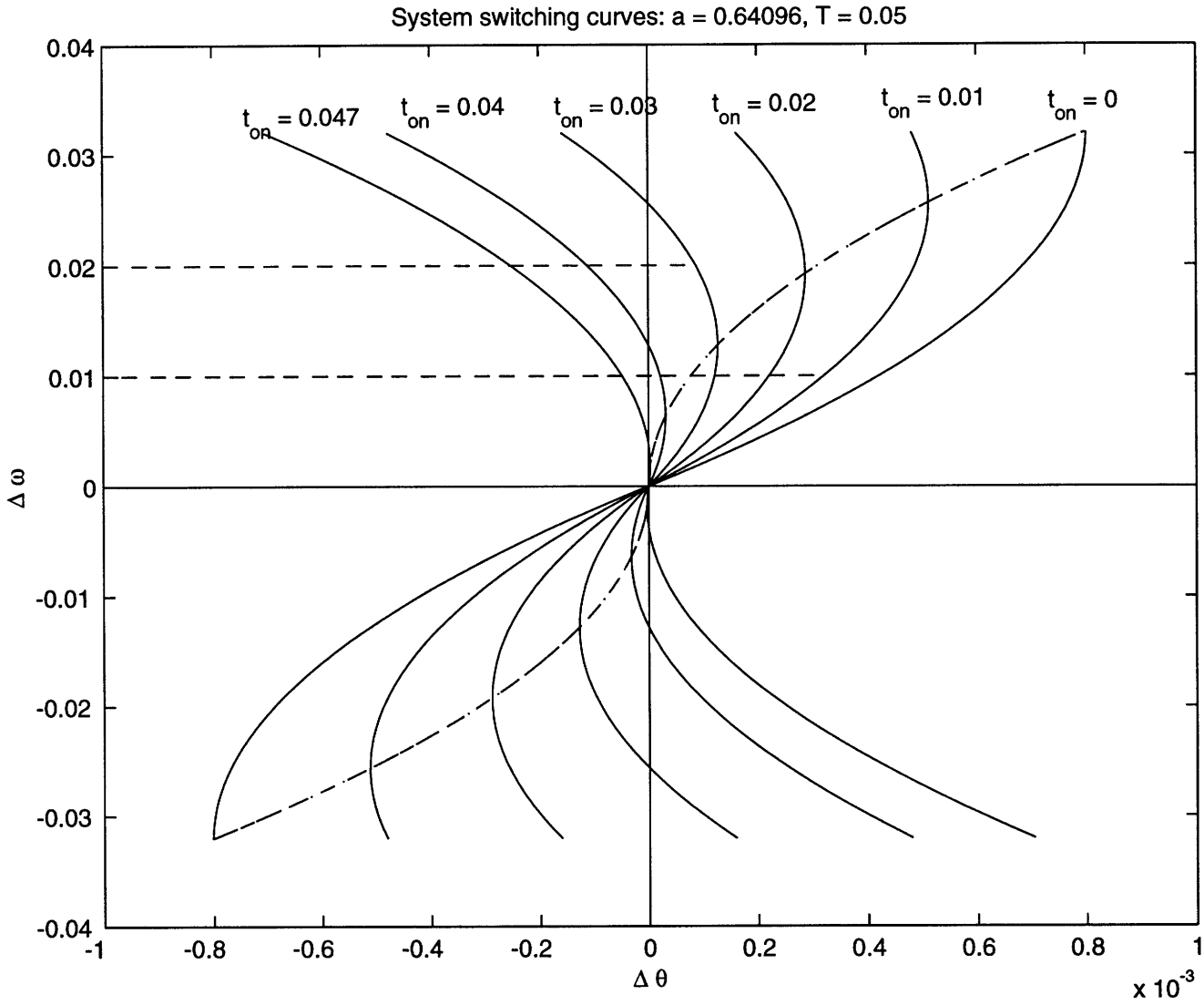

Figure 4-4: Phase plane schematic of nonlinear closed-loop tracking-fuel optimal control system showing the reachable region and the system state trajectories. The t_{on} values above the system curves indicate the time within the control cycle when a pulse is started. These on-times are arbitrary and thus are not optimal values. They are selected to show the closed-loop behavior of the system if the above t_on's are requested. A maximum value of $t_{on} = 0.047$ is used since the minimum pulse allowed by the actual control system is $p = 0.003$. Like in Figure 4-2, the horizontal dashed lines are indicative of the pulse width commanded at that specific point in the phase plane. Recall that the commanded optimal pulse, p, is proportional to $\Delta\omega$ with a constant of proportionality a. Any combination of $\Delta\theta$ and $\Delta\omega$ that lies on a any t_{on} trajectory inside the reachable region, can be driven to the origin of the state space in a single control cycle.

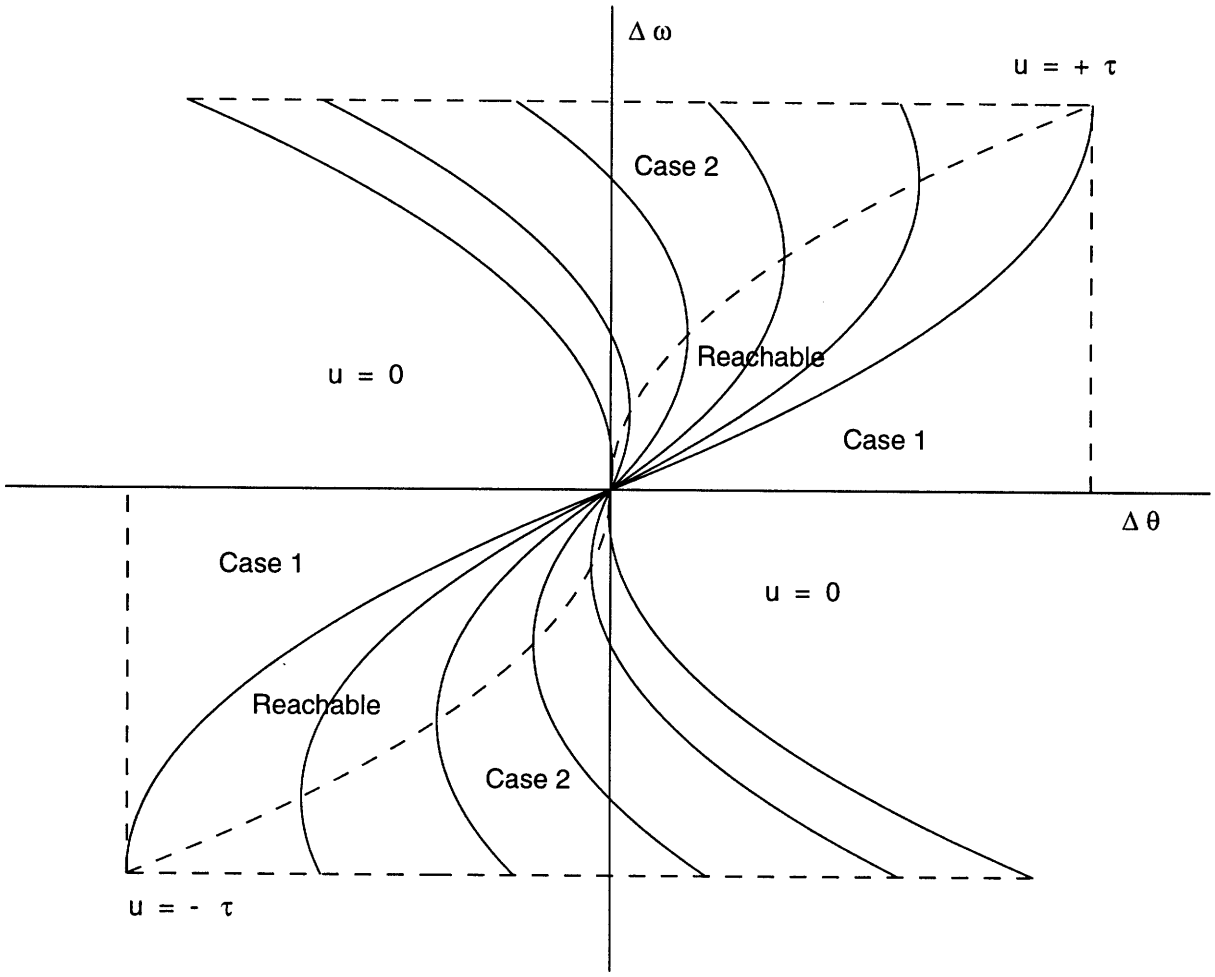

Figure 4-5: Phase plane schematic of nonlinear closed-loop tracking-fuel optimal control system showing the reachable region and the constrained regions superpositioned with the unconstrained system trajectories of Figure 4-2.

width available from the jets. A more complete description of the constrained control mapping is shown in Figure 4-5. Note that regions in quadrant II and quadrant IV are defined as regions in the state space where zero control effort is commanded. This definiton is made in efforts to make the controller more fuel conscious. In these two regions control effort is not required to drive the vehicle towards the origin since it will naturally drift in the correct direction. Since fuel minimization is valued more than time minimization in this thesis, this heurestic assumption on quadrants II and IV is justified.

Hence, to find the optimal control variables corresponding to states located outside $\mathcal{R}_s$ (Case 1, Case 2, or Case 3) the cubic equations of (4.15) must be used. Inside this

reachable region the relations of (4.10) and (4.11) correctly give the optimal control. This optimal control formulation is different from the approach taken in Chapter 3. In the case of the TPBV solution and the RLC formulation, the optimal control effort is defined by on-off switching logic of duration equal to a full control cycle or a prespecified factor of the control cycle. In this chapter, however, an optimal control effort is defined not only with on-off switching logic but also with exact control times and durations that are calculated to be the "best" solution in a tracking-fuel sense. In the experimental implementation the tracking-fuel optimal controller is designed so as to weigh the position tracking error more heavily ($k < 1$) and hence provide enhanced pointing capability from that given by the RLC schemes.

Chapter 5

Experimental Implementation

This chapter describes Lawrence Livermore National Laboratory's hardware-in-the-loop prototype MicroSatellite vehicle and explains how the different control algorithms developed in Chapters 2, 3, and 4 are implemented in the real time software architecture. The prototype vehicle is a high fidelity testbed for preflight assessment and debugging of the guidance and control systems as well as for the refinement of the custom real time software. The embedded real time operating system running in the laboratory is Wind River Systems' VxWorks 5.3.1 (Tornado 1.0.1). A custom built Applications Programming Interface (API) is used to invoke VxWorks functions allowing flexibility to change the base operating system if desired without changing the applications code. The VxWorks framework works in conjunction with a VME bus which connects the Motorola MV1603 PowerPC 603e microprocessor to the system peripherals. The main peripherals, located on the VME crate, associated with the experimental setup include the valve driver for the solenoid valves, the digital I/O board, and a LLNL custom built power distribution board and VME frame buffer board. The I/O board is a Datel DVME-660 board for the interfaces of the valves and the inertial measurement unit. The VME crate, VME bus, and the processor all reside on-board the prototype vehicle (See Figure 5-1).

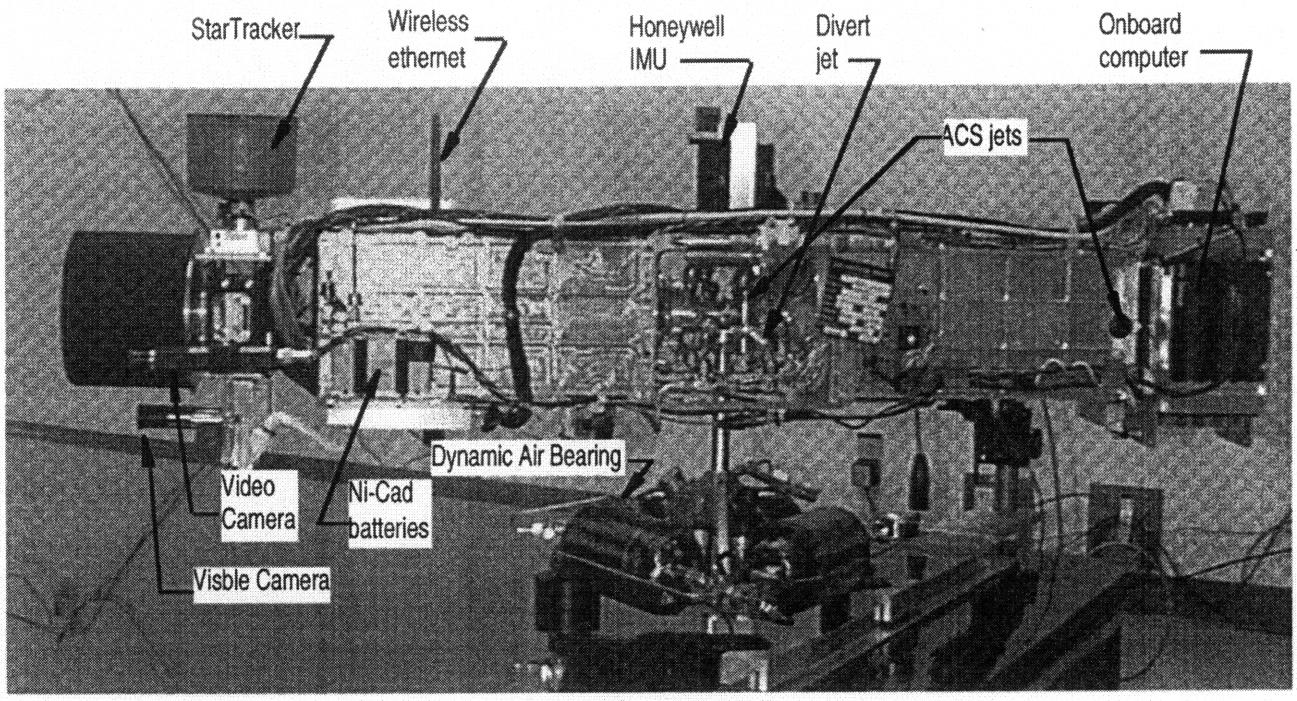

Figure 5-1: Photograph of the LLNL MicroSatellite Dynamic Air-Bearing prototype vehicle.

5.1 Hardware

The MicroSatellite prototype vehicle, built for verifying tracking and control algorithms, carries an on-board Honeywell space certified LIMU inertial measurement unit, a wide field ultraviolet CCD camera for imaging and tracking, a BreezeCom wireless Ethernet for downloading the mission code onto the CPU, and four $\frac{3}{4}$ lb thrust cold gas thrusters for pitch and yaw control, and two $\frac{1}{4}$ lb thrust cold gas thrusters for controlling roll (see Figure 5-1 for exact location of system components). The camera, while not used in this research, will eventually be used to take images that provide the necessary position feedback in future tracking maneuvers. The thrusters expel nitrogen gas, which has a specific impulse about 120 sec. The specific impulse, I_{sp}, describes the overall performance of the propellant and is expressed as Newtons of available thrust per kilogram of propellant consumed (or expelled) per second. Much higher I_{sp} values can be obtained by replacing the inert nitrogen with a fuel/oxidizer bipropellant combination. For more information on the theoretical performance of

Inertia Properties	Value, $[kgm^2]$	Moment Arm, (m)	Maximum angular acceleration $[rad/s^2]$
I_{xx}	0.3078	0.2	0.72
I_{yy}	2.6207	0.5	0.64038
I_{zz}	2.6052	0.5	0.64038
I_{xy}	-0.0353	$---$	$---$
I_{xz}	-0.1036	$---$	$---$
I_{yz}	-0.0330	$---$	$---$

Table 5.1: Moments I_{ii} and products I_{ij} of inertia for the prototype vehicle. Long dashes indicate irrelevant data for the axis in question.

rocket propellants refer to Smith [16]. The mass expulsion process is assumed to have a 3 ms rise and fall time due to the mechanical response time of the valves and the propulsion dynamics of the gas. This assumption is very conservative given the fact that the solenoid valves are rated as having a maximum rise and fall time of 1.5 ms and the propulsion dynamics are an order of magnitude faster. Thus, in order to avoid exciting the actuator/gas dynamics a jet firing command of less than 3 ms in duration is forbidden. This pulse-width deadzone also prevents the control systems from excessively reacting to sensor noise. Both the clock resolution and the software time delays are on the order of 1 ms.

The vehicle is allowed to rotate about a spherical gas-bearing so as to simulate motion in a frictionless environment (See Figure 5-2). The nitrogen in the bearing is regulated at a constant pressure of 1000 psi during experimental runs. The mass properties of the vehicle are shown below in Table 5.1.

The IMU which consists of an accelerometer and a rate-integrating gyro is strapped down to the vehicle so that the sensor axes is aligned with the body axes of the vehicle (see Figure 5-3 for schematic of body and sensor axes). Accelerometer data, which is typically used to update the changing center of mass of a spacecraft, is not necessary in this application because of the short longevity of the experimental runs and our primary interest in just attitude control. In the laboratory, the gyro data normally drifts at about $(1^o/hr)$. There is an earth rate bias of $15^o/hr$ inherently present that is biased out in the IMU software. The gyro drift, if assumed to vary linearly,

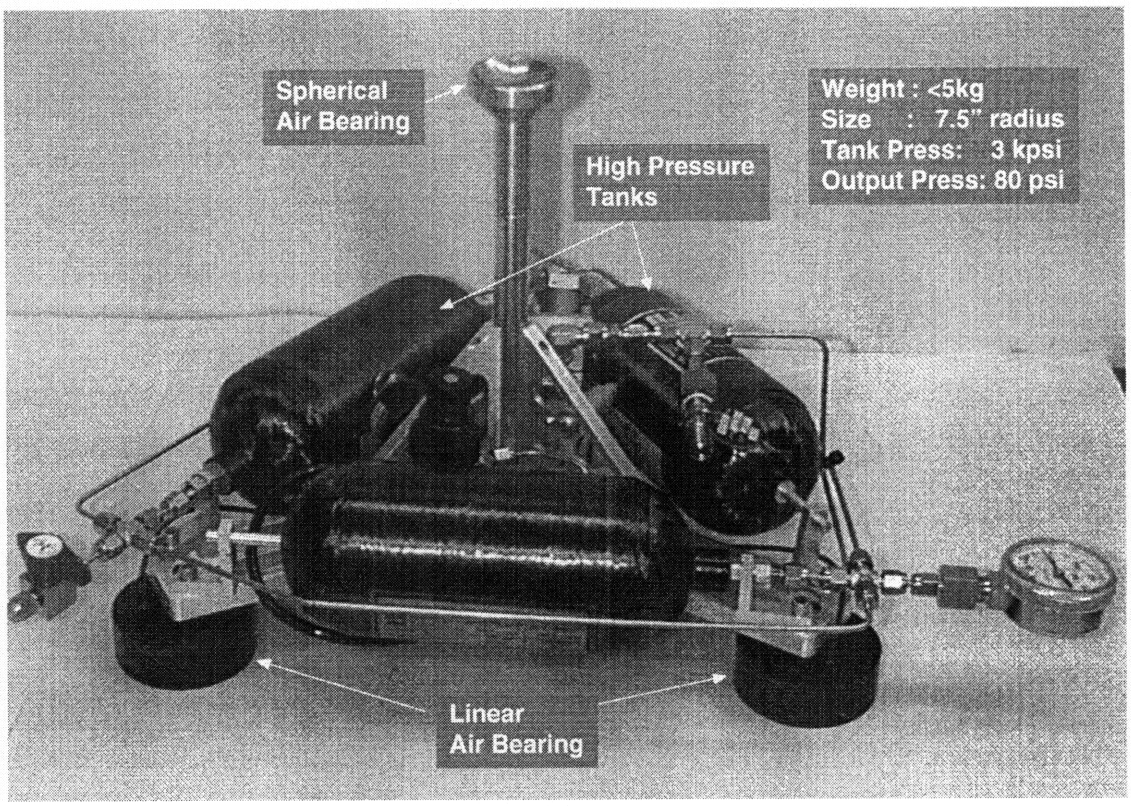

Figure 5-2: Photograph of the gas air bearing assembly of the LLNL *MicroSat* prototype vehicle. The high pressure gas tanks are also illustrated in the picture as well as the linear bearing used in translational motion.

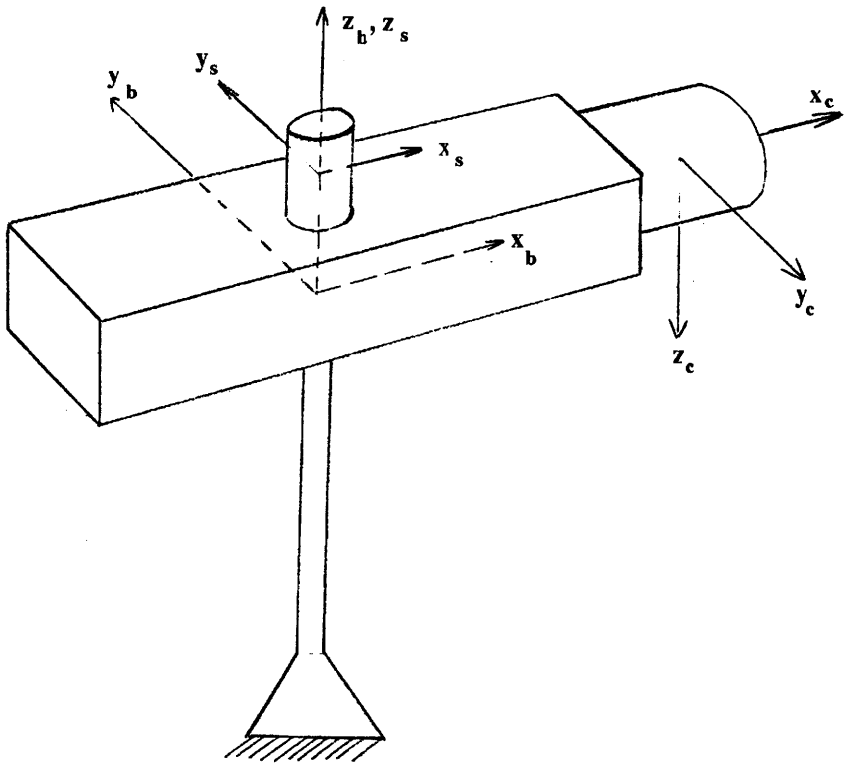

Figure 5-3: Figure of the dynamic air-bearing setup showing the vehicle body axes (x_b, y_b, z_b), the IMU sensor axes (x_s, y_s, z_s), and the camera axes (x_c, y_c, z_c). The x, y, and z axis are the roll, pitch, yaw axis respectively. The longitudinal axis for the camera and the body coincide in the setup.

adds 0.25μrad/s of error to the gyro measurements every control cycle. This error is ignored in the experiments because the runs are usually 30 seconds to 1 minute in duration and the rate tolerance is set to 1 ± 30 mrad/s. The noise in the gyro is observed to be on the order of 5μrad/s, also insignificant given the tolerance level of our control. The gyro measurements are taken every 2.5 ms (400 Hz), stored in a temporary buffer, and then added up every 20 samples to synchronize to a control loop update rate of 20 Hz.

5.2 Control loop description

The schematic for the digital control process is shown in Figure 5-4. The overall control loop, cycling every 50 ms, starts by collecting the synchronized gyro sample for the current body state from the storage buffer and converts it into a body quaternion.

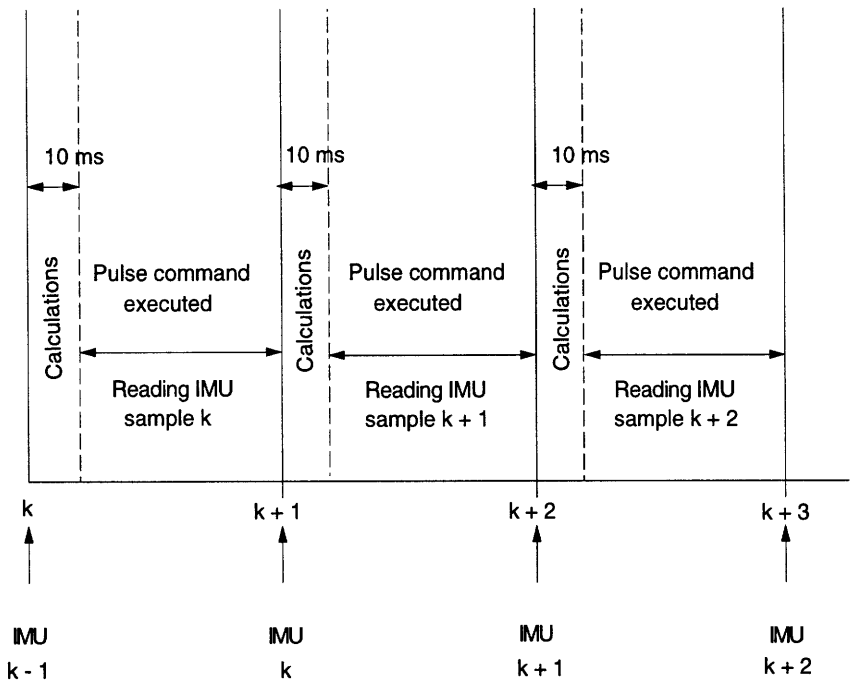

Figure 5-4: This schematic describes the order of operations during a control cycle.

After a built-in 10 ms time period allowed for the control calculations and real-time system checks, an open-valve command is sent to the bus so as to provide the necessary control effort. The control effort requested is based on the prior gyro sample and not the most current gyro sample. Therefore the feedback calculations done in the alloted 10 ms period are using the information form the prior gyro sample. In discrete-time terms this corresponds to requesting an input after the k^{th} calculation based on the sum of the $(k-1)^{\text{th}}$ and $(k-2)^{\text{th}}$ gyro samples. Thus, a whole-cycle delay is present in the real-time control system. An off-valve command is sent to the bus at the end of every control cycle regardless whether the control calculations issued a longer "on" command. Thus, a main constraint present in the real-time control loop is the inability to overlap an on-valve command over several control cycles. This also results in a maximum pulse-width capability of 40 ms per control cycle.

5.3 Control algorithm implementation

5.3.1 General overview

During closed-loop feedback maneuvers, the rate-integrating gyro in the IMU provides rate and position information about all three body axis. The control system gets synchronized angular position increments about the pitch, roll, and yaw axis after every control cycle, $T = 50$ ms. Thus rate information about every axis is obtained directly by dividing the three synchronized gyro outputs respectively by T. For small control cycles, like the one used here, this is a very good approximation as long as the sensor noise is not very significant. This rate information is used directly in the controllers for rate feedback.

5.3.2 Quaternion feedback

In spacecraft control applications the concept of a quaternion is widely used to represent rigid body coordinate axes transformations. It is usually favored over Euler angles and direction cosine methods for its computational efficiency. Quaternions offer more efficient memory usage and faster execution time in real-time control applications. They are also convenient for optimal control schemes because they provide the least angle of rotation when commanding a spacecraft from one configuration to another. A quaternion, as defined by Hamilton [6], is a mathematical operator that can act on a vector so as to rotate it about a given axis and then change its length. The general mathematical notation of a quaternion is

$$\mathbf{Q} = q_1\mathbf{i} + q_2\mathbf{j} + q_3\mathbf{k} + q_4 \tag{5.1}$$

A quaternion is thus a vector appended by a scalar. The first three terms are vector components directly related to a virtual axis of rotation while the fourth term is a scalar part representing the magnitude of rotation about the virtual axis. To see this more clearly we can write the following definitions:

$$\left.\begin{aligned} q_i &= n_i sin(\theta/2) \quad \text{i} = 1,2,3 \\ q_4 &= cos(\theta/2) \end{aligned}\right\} \tag{5.2}$$

Quaternions, as formulated by Hamilton, are a set of four element hypercomplex numbers whose law of multiplication obeys

$$\left.\begin{aligned} \vec{\epsilon_3} &= n_2\vec{\epsilon_1} + n_1\vec{\epsilon_2} + \vec{\epsilon_1} \times \vec{\epsilon_2} \\ n_3 &= n_1 n_2 - \vec{\epsilon_1}^T\vec{\epsilon_2} \end{aligned}\right\} \tag{5.3}$$

where ϵ_i's are the vector parts of the quaternions Q_1, Q_2, and Q_3 respectively, and n_i are the scalar parts corresponding to Q_i. Note that in (5.3) we are multiplying two quaternions, Q_1 and Q_2, and get back a quaternion Q_3. A more physical interpretation of the quaternion formulation comes from Euler's theorem which states that any rigid body rotation can be exactly described by a single body rotation of some magnitude about a single fixed axis called the Euler axis. In some textbooks quaternions are referred to as Euler parameters because the interpretation lends itself more toward Euler's theorem than to the Hamiltonian notation. Thus, matrix notation is entirely adequate for dealing with the quaternion formalism. The rotation matrix equivalent of a quaternion, Q, can then be expressed as

$$\mathbf{R} = (n^2 - \vec{\epsilon}^T\vec{\epsilon})\mathbf{I} + 2\vec{\epsilon}^T\vec{\epsilon} - 2n\vec{\epsilon}^x \tag{5.4}$$

where $\mathbf{I}$ is the 3×3 identity matrix and $\vec{\epsilon}^x$ is the notation for the skew symmetric matrix defining the vector product by the vector $\vec{\epsilon}$ and is written as

$$\vec{\epsilon}^x = \begin{bmatrix} 0 & -\epsilon_3 & \epsilon_2 \\ \epsilon_3 & 0 & -\epsilon_1 \\ -\epsilon_2 & \epsilon_1 & 0 \end{bmatrix} \tag{5.5}$$

Equation (5.4) is displayed explicitly as,

$$\mathbf{R} = \begin{bmatrix} 1-2({\epsilon_2}^2+{\epsilon_3}^2) & 2(\epsilon_1\epsilon_2+\epsilon_3 n) & 2(\epsilon_1\epsilon_3-\epsilon_2 n) \\ 2(\epsilon_2\epsilon_1-\epsilon_3 n) & 1-2({\epsilon_3}^2+{\epsilon_1}^2) & 2(\epsilon_2\epsilon_3+\epsilon_1 n) \\ 2(\epsilon_3\epsilon_1+\epsilon_2 n) & 2(\epsilon_3\epsilon_2-\epsilon_1 n) & 1-2({\epsilon_1}^2+{\epsilon_2}^2) \end{bmatrix} \tag{5.6}$$

We will employ this more intuitive quaternion formalism throughout the thesis. In (5.2) the n_i's are components of the unit vector $\mathbf{n} = [n_1 \quad n_2 \quad n_3]$ indicating the orientation of the Euler axis with respect to the reference coordinate system and θ is the angle of counterclockwise rotation about the "virtual" Euler axis. The reference axes, often referred to as the home position of the kinematics, is where the Euler "virtual" angle θ is defined to be zero. In quaternion representation this orientation is $\mathbf{q}_{ref} = [0 \quad 0 \quad 0 \quad 1]$. Equation 5.2, however, is valid only if the following constraint holds

$$q_1^2 + q_2^2 + q_3^2 + q_4^2 = 1 \tag{5.7}$$

which directly stems from $||\mathbf{n}|| = 1$. Equation 5.7 implies that the quaternion, $\mathbf{Q}$, is a unitary quaternion because its length (and hence the norm) is 1. Unitary quaternions have nice properties that make computations quicker and make it easier when working with spacecraft control system applications. For a more detailed presentation of quaternions and quaternion algebra I recommend textbooks by Hughes [7] and Chobotov [2] and an informative article by Niva [11].

In spacecraft attitude control, the unitary quaternion formalism works well with the basic control problem of driving a set of body axes toward a commanded axes orientation. Specifically, in optimal control, quaternions' relation with Euler's theorem provides a least-angle solution to the rotation kinematics. In feedback control applications the quaternion representation contains the angular position information that is output by the gyro. The incremental angular output of the gyro can be transformed into an equivalent quaternion representation describing the three-axis measured body rotation (see the next section for a detailed discussion of the specific transformation algorithm). Furthermore, it can easily be shown that the attitude errors in roll,

pitch, and yaw independently can be determined by the first three components of the quaternion relating the measured body orientation to the commanded orientation. This quaternion is expressed mathematically as

$$\mathbf{Q}_e = \mathbf{Q}_b \, \mathbf{Q}_c^* \tag{5.8}$$

where $\mathbf{Q}_b$ and $\mathbf{Q}_c$ are the measured body quaternion and command quaternion respectively relative to a reference set of axes. The asterisk after $\mathbf{Q}_c$ represents the conjugate quaternion which is given by

$$\mathbf{Q} = (-\mathbf{q}, q_4) \tag{5.9}$$

For a unitary quaternion (one satisfying (5.7)) the conjugate of a quaternion is equal to the inverse quaternion. The inverse quaternion is intuitively the equivalent of reversing the set of axes being considered as the reference axes. Thus, the inverse of the quaternion that relates the set of axes A to axes B is just the quaternion that relates axes B to axes A. This is probably the most important property of unitary quaternions since it makes the equations for the attitude errors much simpler and more computationally efficient. The actual attitude errors that are used in position feedback loops are given by the following relations

$$\left.\begin{array}{rcll} \epsilon[i] & = & -2Q_e[i] & \text{i = 1,2,3 Small angle errors} \\ \epsilon[i] & = & -\Delta\theta Q_e[i]/sin(\Delta\theta/2) & \text{i = 1,2,3 Large angle errors} \end{array}\right\} \tag{5.10}$$

where the components $\epsilon[i]$, i=1,2,3 represent the errors in roll, pitch, and yaw respectively and $\Delta\theta$ is the angle of rotation along the Euler axis and given by

$$\Delta\theta = 2cos^{-1}(Q_e[4]) \tag{5.11}$$

.

In this thesis the control laws designed are tested using small angular step dis-

turbances ($\pm$ 4^o) so that the small angle formulation of (5.10) is adopted. Of great importance in the feedback loop is the maintaining of the orthonormality of the quaternion. System errors can cause the norm of the quaternion to deviate form unity and thereby change the consistency and reliability of the unitary quaternion formulation of (5.8). To prevent this phenomena, the body quaternion can be divided through by its length and the constraint condition of (5.7) is thereby restored. If the alternative direction cosine matrix formulation is used the normalization process requires many more computations.

5.3.3 Quaternion extraction

The extraction of the measured body quaternion from gyro output can be done several different ways depending on the specific hardware and software setup. Regardless of the extraction method, the main benefit to the use of the quaternion formulation is that it offers increased computational speed because of the nature of quaternion algebra. Quaternion algebra just involves basic vector addition and multiplication operations and avoids trigonometric functions and memory consuming matrix schemes. In addition, quaternion calculations, unlike the other formalisms, are not prone to singularities at specific body orientations.

The conventional method of extraction consists of taking the elements of the general rotation matrix and calculating the body quaternions using the correspondence between the direction cosine matrix and the quaternion formalism. An update law based on either Spurrier [17] or Shepperd [15] is then usually employed to keep the measured quaternion current after every control cycle. A much more straightforward method is employed in this thesis that takes advantage of the strap-down rate-integrating gyro of the prototype vehicle. The method, developed by Wie and Barba [22], is somewhat less accurate than the prior methods discussed but is better suited for the incremental angle readout of the gyro. The extraction process consists of numerically integrating the quaternion equations using a 4th-order Taylor series expansion to give the quaternion update. The method requires knowledge of only the most current gyro output and can be expressed as

$$Q_i(T+t) = Q_i(t) + R_i(t) - D^2 Q_i(t) - D^2 R_i(t)/3 + D^4 Q_i(t)/6 \tag{5.12}$$

where

$$\left.\begin{aligned} D^2 &= \Delta\theta_1^2 + \Delta\theta_2^2 + \Delta\theta_3^2 \\ R_1 &= 1/2[\Delta\theta_1 Q_4 - \Delta\theta_2 Q_3 + \Delta\theta_3 Q_2] \\ R_2 &= 1/2[\Delta\theta_1 Q_3 + \Delta\theta_2 Q_4 - \Delta\theta_3 Q_1] \\ R_3 &= 1/2[-\Delta\theta_1 Q_2 + \Delta\theta_2 Q_1 + \Delta\theta_3 Q_4] \\ R_4 &= 1/2[-\Delta\theta_1 Q_1 - \Delta\theta_2 Q_3 - \Delta\theta_3 Q_4] \end{aligned}\right\} \tag{5.13}$$

and $\Delta\theta_i$ are the incremental angle outputs form the gyros over the control period of T seconds. The body rates used in this type of feedback loop are then $\Delta\theta_i/T$, the same as mentioned in the prior section above. It should be noted that because this algorithm is not exact and the microprocessor has finite word length, the unity of the quaternion norm is rapidly degraded after every control cycle. The quaternion normalization process described earlier, however, eliminates the errors due to the degradation.

5.3.4 Cubic solution to tracking-fuel problem

As was seen in Chapter 4 for the tracking-fuel optimal control problem, the solution to a cubic equation gives the optimal control variable P^*. To solve the cubic solution at every control cycle where it is needed a computationally efficient solution scheme has to be used. In digital control systems the amount of alloted calculation time is limited. Thus, in order to avoid a numerical methods such as Newton's Tangent Line approximation, the *Numerical Recipes in C* [12] reference was consulted for an analytical cubic equation solution. For a typical cubic equation

$$P^{*3} + aP^{*2} + bP^* + c = 0 \tag{5.14}$$

where a, b, c are real coefficients depending on which case in Chapter 4 the states

correspond to. The analytic solution method for P^* in (5.14) is broken up into two main parts. The first part gives an expression for when (5.14) has three real roots P_1^*, P_2^*, and P_3^*, while the second part gives the one real root in the case when the other two roots are complex conjugates. To separate out these two cases the following is first computed

$$\left.\begin{array}{rcl} Q & = & \frac{a^2-3b}{9} \\ R & = & \frac{2a^3-9ab+27c}{54} \end{array}\right\} \tag{5.15}$$

If $R^2 < Q^3$, then the cubic solution has three roots given by

$$\left.\begin{array}{rcl} P_1^* & = & -2\sqrt{Q}cos(\frac{\theta}{3}) - \frac{a}{3} \\ P_2^* & = & -2\sqrt{Q}cos(\frac{\theta+2\pi}{3}) - \frac{a}{3} \\ P_3^* & = & -2\sqrt{Q}cos(\frac{\theta-2\pi}{3}) - \frac{a}{3} \end{array}\right\} \tag{5.16}$$

where $\arccos\theta = (R/\sqrt{Q^3})$. Otherwise, the single real root is given below

$$P^* = (A+B) - \frac{a}{3} \tag{5.17}$$

where

$$A = -sgn(R)[|R| + \sqrt{R^2 - Q^3}]^{1/3} \tag{5.18}$$

and

$$B = \begin{cases} Q/A & A \neq 0 \\ 0 & A = 0. \end{cases} \tag{5.19}$$

Notice that for the single real root case explicit equation for the complex conjugate root pair is left out. In control systems an imaginary or complex control effort makes no real physical sense. This solution algorithm minimizes the roundoff error associated with the powers and exponents in the expressions and works well with a real-time control application.

Chapter 6

Results

6.1 Chapter summary

In this chapter, experimental and simulation results for four attitude controller designs are presented – the PWM/PD controller, the standard RLC, the short-pulse RLC, and a combined phase plane optimal controller. The first three controllers have been already introduced in Chapters 2 and 3. The latter of these controllers is a multiple phase plane control scheme which combines the short-pulse RLC phase plane of Chapter 3 with the phase plane of the tracking-fuel optimal controller discussed in Chapter 4. This hybrid control scheme uses the short-pulse RLC for time-fuel optimal transient shaping and the tracking-fuel optimal controller to give improved steady-state accuracy and stabilization. Experimental data and numerous simulation examples are compared and discussed in order to gain insight into the plant closed-loop dynamics. These are also carefully studied so as to assess the validity of the plant model adopted in the thesis. This chapter is separated into three main sections. The first section presents the experimental data, the second section presents the simulation results, and the last section compares the results presented in the first two sections. Experimental data is acquired using Lawrence Livermore National Laboratory's (LLNL) next generation Microsatellite vehicle, *MicroSat*. This ground-based testbed has been under development for the past two years and provides a great opportunity to test attitude control systems in an inexpensive and reliable way. The

simulations for all of the above mentioned controllers are designed and performed using the Matlab/Simulink software package. The pulse-width modulated PD controller (PWM/PD) is presented first in the three sections of the chapter as it is used as the benchmark controller in this thesis. This will be followed by the standard RLC, short-pulse RLC, and the multiple phase plane optimal controller, in that order.

6.2 Experimental Results

This section presents the data for all the relevant experiments performed at the LLNL MicroSatellite facility. The experimental methodology is briefly described in the first part of this section. We then show trial runs of the PWM/PD control law and study the resulting step responses and pulse plots to establish a benchmark data set. A comparison of experimental data with the runs for the other three control algorithms is also made.

6.2.1 Experimental Methodology

Preceding any experiment, the validity of the vehicle home position is established. The home position is defined as the initial configuration of the vehicle before the experiment is started and has the associated home quaternion, $\mathbf{q} = [0\ 0\ 0\ 1]$. In our experiments it is taken to be aligned with a plane parallel to the floor and normal to one of the walls. To maintain this position consistently, we statically balance the vehicle by positioning a collection of counterweights along the three axes of the vehicle while it is supported by the spherical gas-bearing. The counterweights, located on the side not shown in the photograph of Chapter 1, are thick, cylindrical pieces of brass that are tapped so as to screw in and out on a threaded shaft. There are three shafts, each aligned with a body axis of rotation. In addition to balancing the vehicle, the nonzero gyro measurements caused by small residual motion are averaged before the experiment is performed. This ensures that the initial gyro data used by the control algorithm is true and adjusted for any nonzero bias.

The experiments performed consist of commanding the vehicle to do consecutive

step commands of equal magnitude. Figure 6-1 shows the reference input to the vehicle. The reference input can be divided into four sequential step commands as can be seen from Figure 6-1. The vehicle is first given a positive step command away from its home position. This is followed by a command to return back to home and then by a command to take a negative step away from this last position. The fourth and final command instructs the vehicle to return to its home position. In between each of the step commands an attitude hold command of anywhere from 0.15 to 0.5 seconds is given once a specified attitude and body rate tolerance is met. The tolerance defined is ± 1 mrad and ± 1 mrad/s. This allows for both a visual check on the attitude stabilization characteristics as well as for an opportunity for the vehicle to attain steady-state before being instructed away from the current position. This reference input is chosen so as to acquire multiple experimental step responses for each axis in the least amount of time. In all of the experiments, the step commands are set to $\pm 4^o$ (69.7 mrad) in all directions. This value is chosen for two reasons. First, the maximum allowed angular travel in the roll and pitch axis is $\pm 5^o$ and we wish to be safe against damage caused by forceful overshoot. Furthermore, the yaw axis also is stepped at $\pm 4^o$ levels in order to remain consistent with the numbers used in the experiments. The second reason for the selection of this step magnitude is to maintain small angle motion so that the quaternion update equations remain linear (see Chapter 5).

6.2.2 Pulse-Width Modulated Proportional Derivative Control

One of the first experiments performed using a PWM/PD consisted of qualitatively validating the uncoupled rigid body model for the attitude dynamics of the MicroSat test vehicle. The reference input described in the prior section and shown in Figure 6-1 is consecutively applied to each body axis of the vehicle in the ensuing discussion. By commanding each axis separately during the same experiment we are able to analyze the effect of inter-axis torque coupling on the control system design. In addition to

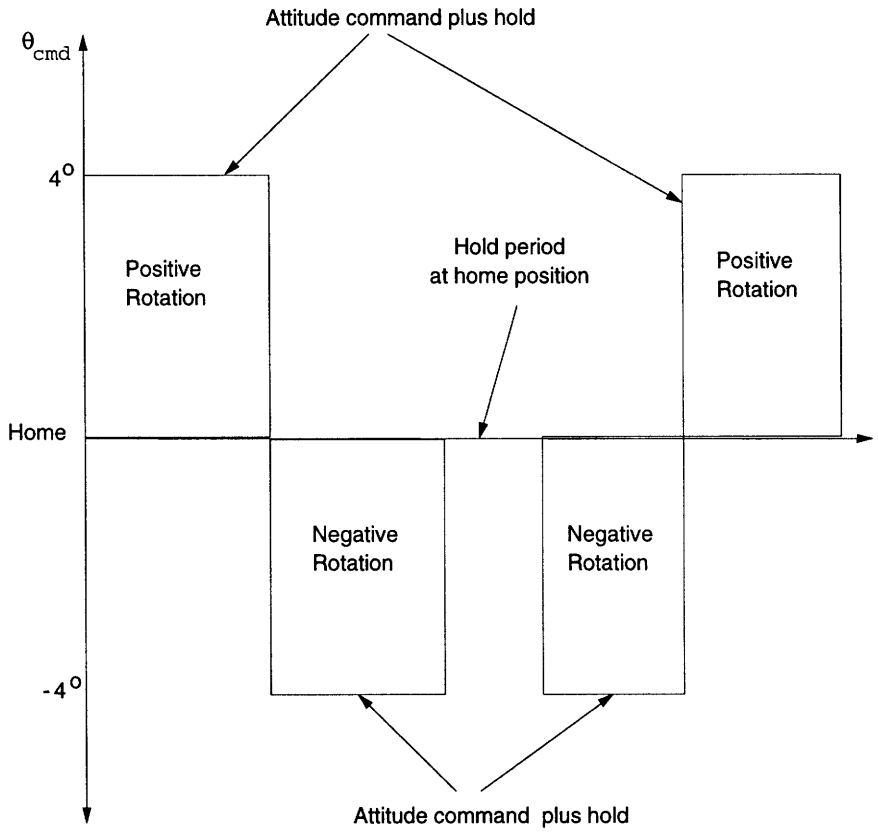

Figure 6-1: A schematic of the reference input used in the *MicroSat* control system testing.

this, we are also able to assess the validity of the linear uncoupled model assumed in most of this thesis. Figures 6-2, 6-3, and 6-4 show the sequential small step commands of the roll, pitch, and yaw axis respectively. From these step responses it is evident that some inter-axis coupling exists in the vehicle. This coupling effect is stronger, however, in the roll axis (see Figure 6-2) than in the remaining two axes. Note the high amplitude oscillations during the small step maneuvers in the pitch and yaw axis. In the case of the pitch and yaw axis, a very small ripple effect is seen as a result of inter-axis torque disturbances. This behavior is to be expected since the products of inertia, although small compared to the moments of inertia (see Table 5.1), are nonzero and will contribute to some degree to the overall system response. On the other hand, the higher moments of inertia for the pitch and yaw axis allow these axes to be much more robust to coupling disturbances. The linear uncoupled model is thus a good approximation for the attitude dynamics about the pitch and yaw axis of the *MicroSat* test vehicle. Furthermore, the pitch and yaw axis have very similar inertia properties and thus in the ensuing experiments we only present the data for the yaw axis[1]. Any discrepancy between the pitch and yaw axis would be mainly due to inconsistent tolerances and disparate thrust magnitudes between the two sets of axes jets.

Results for an experimental run of the PD/PWM control for the yaw axis is shown in Figures 6-5 and 6-6. The PD gains used in this experiment are $K_p = 20$ and $K_d = 8$. In this run, the same type of control is used for the roll and pitch axes but with a zero command reference. It is evident that the step response given in Figure 6-5 has a nicely damped response as well as an acceptable bandwidth. The bandwidth can be estimated by using the following rule of thumb calculation

$$\omega_n \approx \frac{1.8}{t_r} \tag{6.1}$$

where t_r is the 10% to 90% rise time. For Figure 6-5 we find $t_r \approx 1.8$ sec and therfore

[1]In fact they both have the same measured moment arm of 0.5 m and identical jet thrusters rated at $\frac{1}{4}$ lb

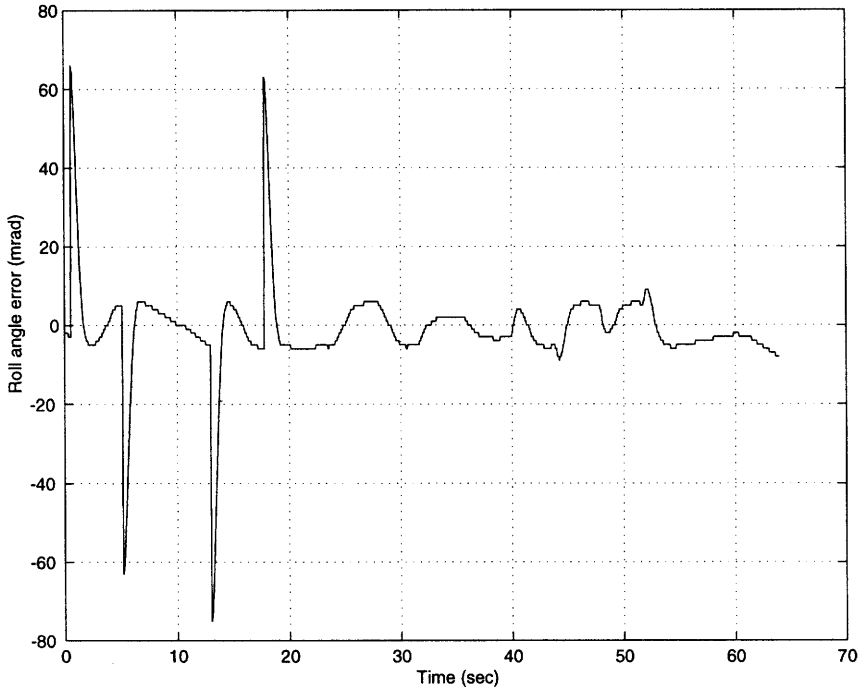

Figure 6-2: Experimental step response of *MicroSat* using pulse-width modulated proportional derivative control on all three axes sequentially. The roll axis is the first to be commanded with the defined reference input. This figure shows the roll axis angular error response during the course of the entire experiment. The gains for the roll axis are $K_p = 20$ and $K_d = 5$. The step input is of magnitude 69.7 mrad.

we obtain a value $\omega_n \approx 1\ r/s$. The fuel efficiency, however, of this control system is very poor. Figure 6-6 shows that very frequent switching of the valves is necessary to achieve such a smoothly shaped response. The loud popping noises heard when implementing this control system is indicative of the excessive switching of the valves. Limit cycling should appear if the experiment called for a single direction step response followed by an attitude hold command. A second experiment is shown in Figures 6-7 and 6-8 in which the gains are $K_p = 26.3$ and $K_d = 15.1$. In this experiment we observe a somewhat quicker and more damped response. Using Equation 6.1 we arrive at rise time of $t_r \approx 1.5$ sec and thus at a bandwidth value of $\omega_n \approx 1.2\ r/s$. These gains, however, increase the amount of control effort that is output from the PD term and as a result increase the frequency of jet firings during attitude maneuvering. Comparing Figures 6-6 and 6-8 it is clearly seen that the higher PD gains increase fuel consumption.

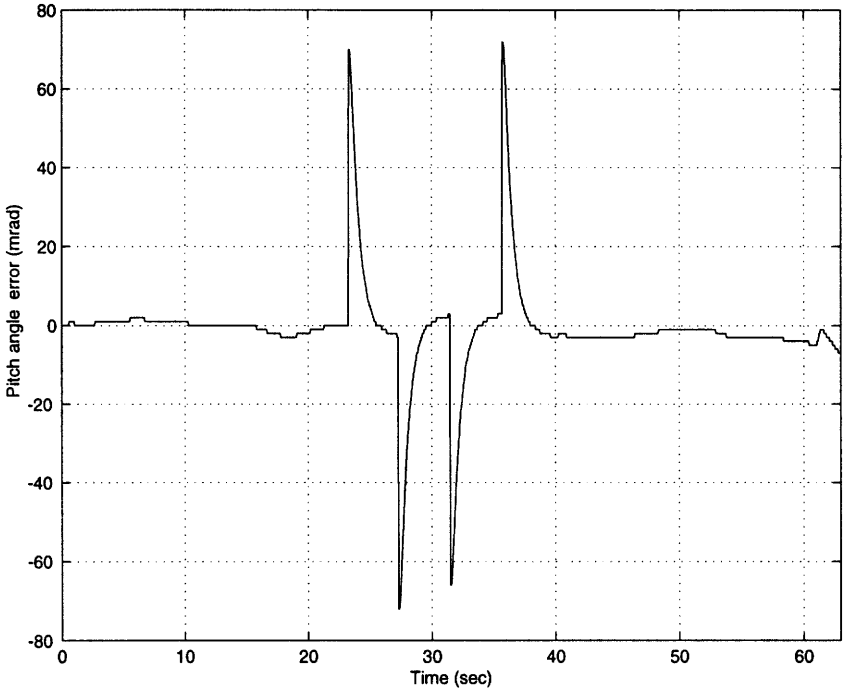

Figure 6-3: Experimental step response of *MicroSat* using pulse-width modulated proportional derivative control on all three axes sequentially. The pitch axis is the second to be commanded with the defined reference input. This figure shows the pitch axis angular error response during the course of the entire experiment. The gains are $K_p = 20$ and $K_d = 8$.

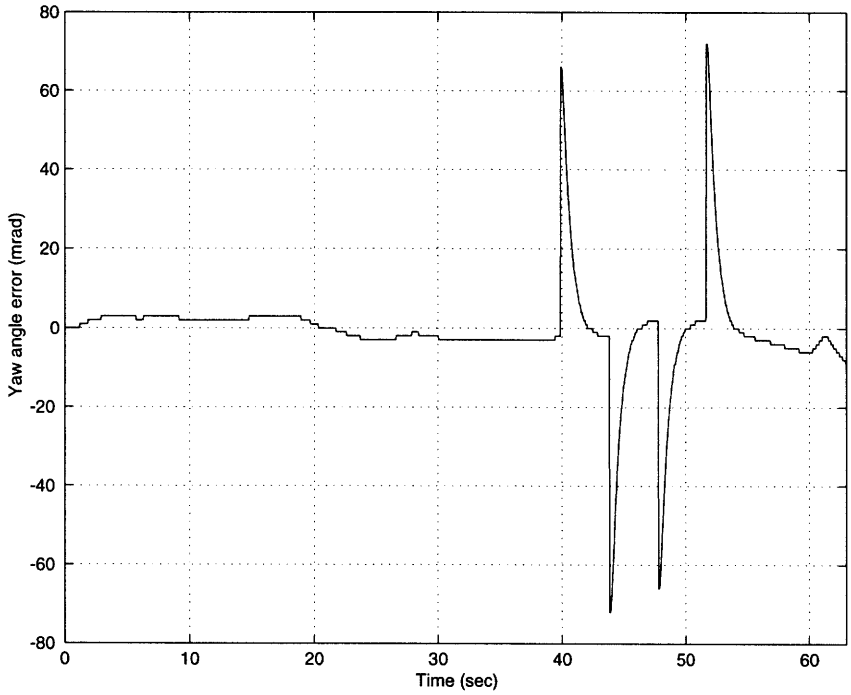

Figure 6-4: Experimental step response of *MicroSat* using pulse-width modulated proportional derivative control on all three axes sequentially. The yaw axis is the last to be commanded with the defined reference input. This figure shows the yaw axis angular error response during course of the entire experiment. The gains are $K_p = 20$ and $K_d = 8$. The step input is of magnitude 69.7 mrad.

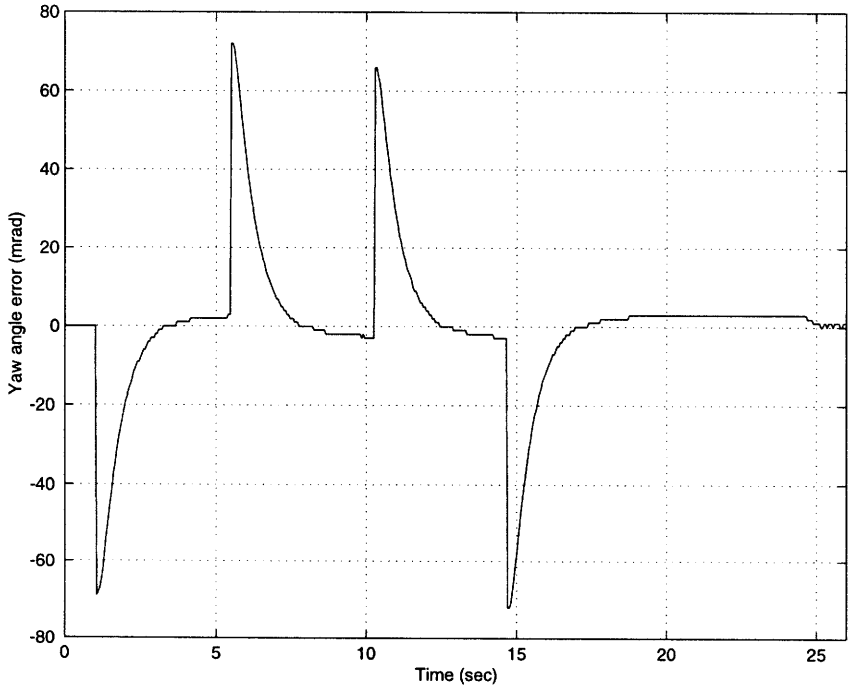

Figure 6-5: Experimental step response of *MicroSat* using pulse-width modulated proportional derivative control on the yaw axis. The gains are $K_p = 20$ and $K_d = 8$. The step input is of magnitude 69.7 mrad.

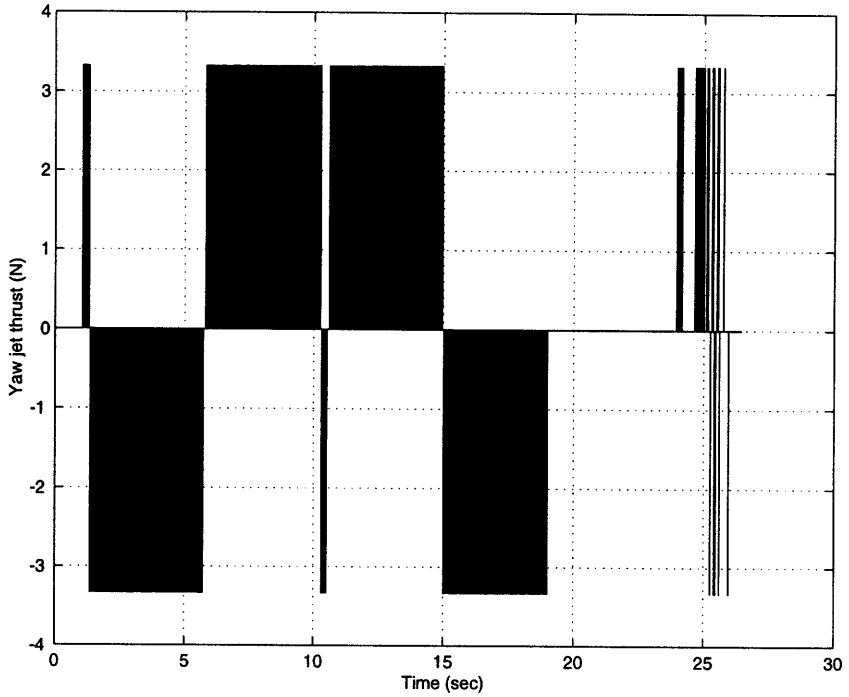

Figure 6-6: Experimental pulse command plot of *MicroSat* using pulse-width modulated proportional derivative control on the yaw axis. The gains are $K_p = 20$ and $K_d = 8$. The step input is of magnitude 69.7 mrad.

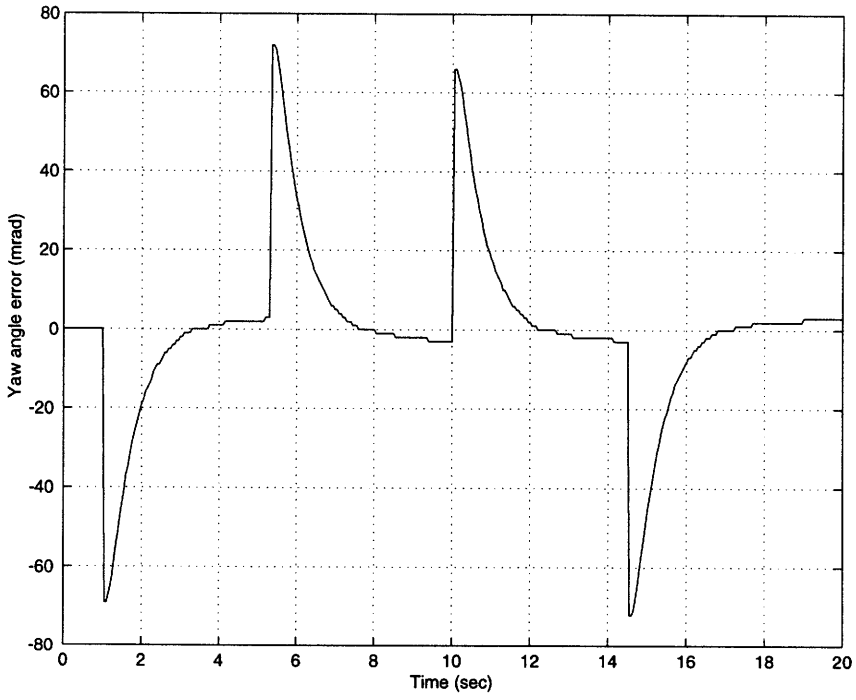

Figure 6-7: Experimental step response of *MicroSat* using pulse-width modulated proportional derivative control on the yaw axis. The gains are $K_p = 26.3$ and $K_d = 15.1$. The step input is of magnitude 69.7 mrad.

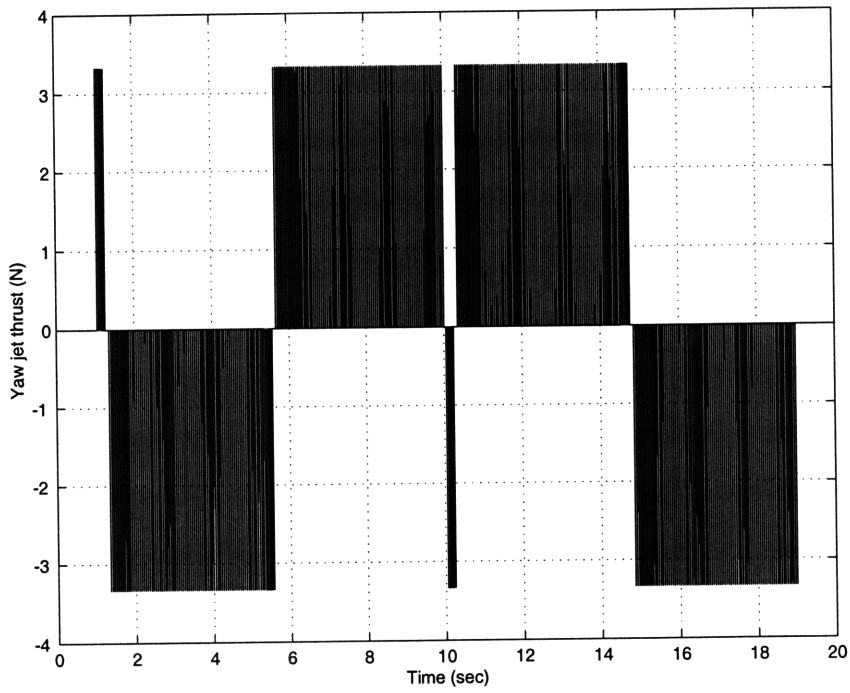

Figure 6-8: Experimental pulse command plot of *MicroSat* using pulse-width modulated proportional derivative control. The gains are $K_p = 26.3$ and $K_d = 15.1$. The step input is of magnitude 69.7 mrad.

6.2.3 Standard RLC Algorithm

Two sets of experiments using the standard RLC control design are presented in this section. The first experimental run uses design parameters $\theta_{db} = 0.01$ rad, $\theta_r = 0.0203$ rad, and $A_1 = 0.1231$. This design selection approximates a time-fuel optimal controller of time weighting $\lambda = 0.4$. The step responses and pulse plans are shown in Figures 6-9 and 6-10 and are seen to display an exponentially decreasing limit cycle and excessive fuel expenditure. These limit cycle oscillations tend to be wild and out of control. The limit cycle thus does not have time to settle before a sample is acquired within the tolerance limit and a new reference step command is given. A second set of RLC parameters- $\theta_{db} = 0.005$ rad, $\theta_r = 0.005071$ rad and $A_1 = 0.073159$- are used in another RLC design iteration in order to compare with the first design. The step response and pulse plot for this second design iteration are illustrated in Figures 6-11 and 6-12 respectively. A clear steady state limit cycle is seen in the step response of Figure 6-11. This is more clearly observed at the end of the last step response where a uniform limit cycle oscillation is present. The period of the limit

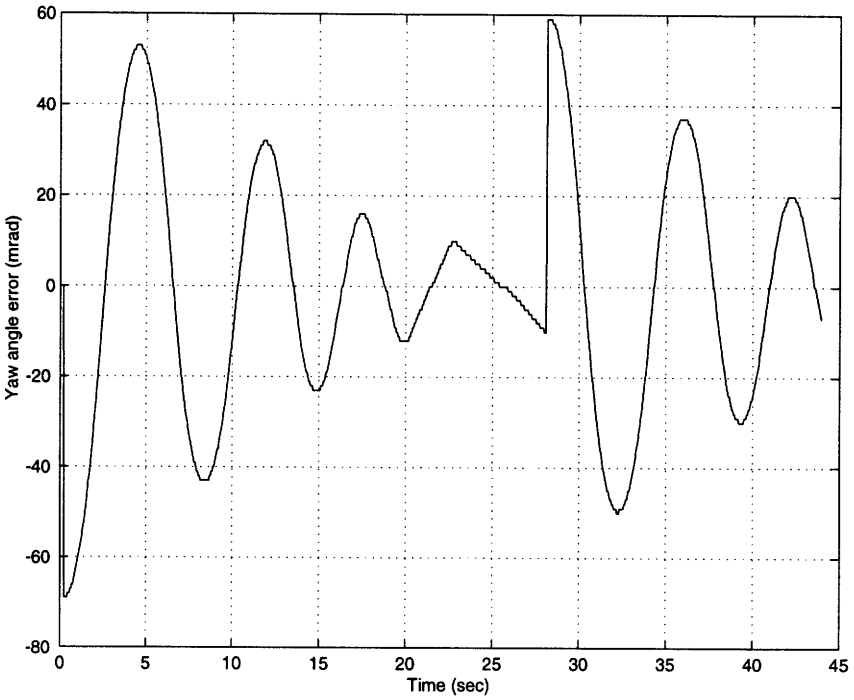

Figure 6-9: Step response of *MicroSat* yaw axis angular error with standard RLC control law using design parameters $\theta_{db} = 0.01$ rad, $\theta_r = 0.0203$ rad, and $A_1 = 0.1231$. Note that these parameters approximate a time-fuel optimal controller with a time weighting of $\lambda = 0.4$. The step input is of magnitude 69.7 mrad.

cycle is approximately 9 sec. By comparing the pulse plots of the two designs (see Figure 6-10 and 6-12), we can conclude that the second design iteration is more fuel efficient than the first. This steady state improvement is also accompanied by an improved transient response as well. Although this second design is an improvement over the first design, we do not recommend the use of this controller for improving the fuel efficiency of the *MicroSat* vehicle; better performance is achieved with the short-pulse RLC algorithm presented in the next section.

6.2.4 Short-Pulse RLC Algorithm

The short-pulse RLC control algorithm is also implemented on the *MicroSat* test vehicle and three design iterations are done before findinga set of RLC parameters and short-pulse boundary values that give acceptable transient and steady state "fuel-saving" performance. After several trial and error experimental runs it is observed that a good choice for the short-pulse boundary values is

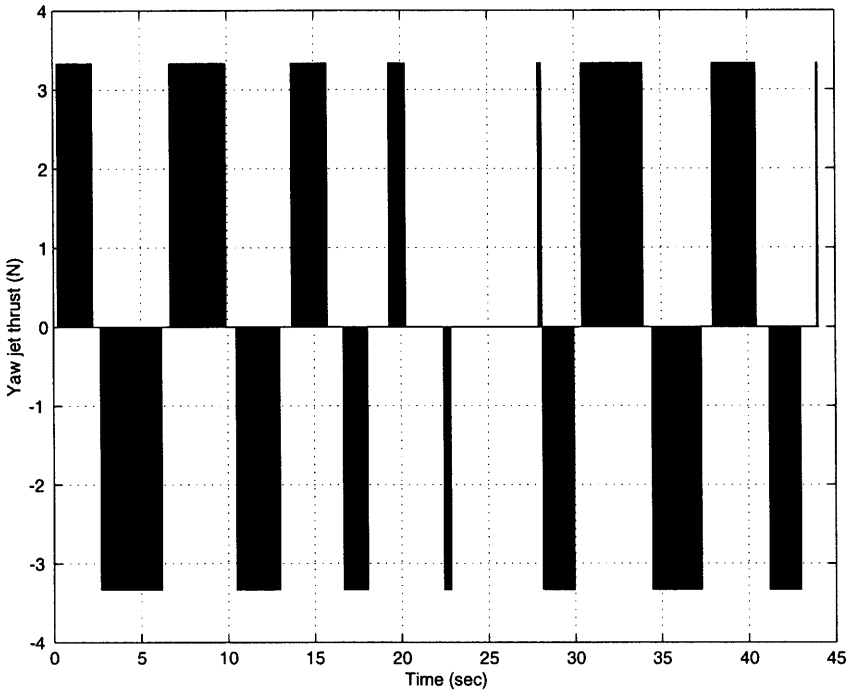

Figure 6-10: Pulse plot of the yaw thruster firings with standard RLC control law. Design parameters selected are $\theta_{db} = 0.01$ rad, $\theta_r = 0.0203$ rad, and $A_1 = 0.1231$. The step input is of magnitude 69.7 mrad.

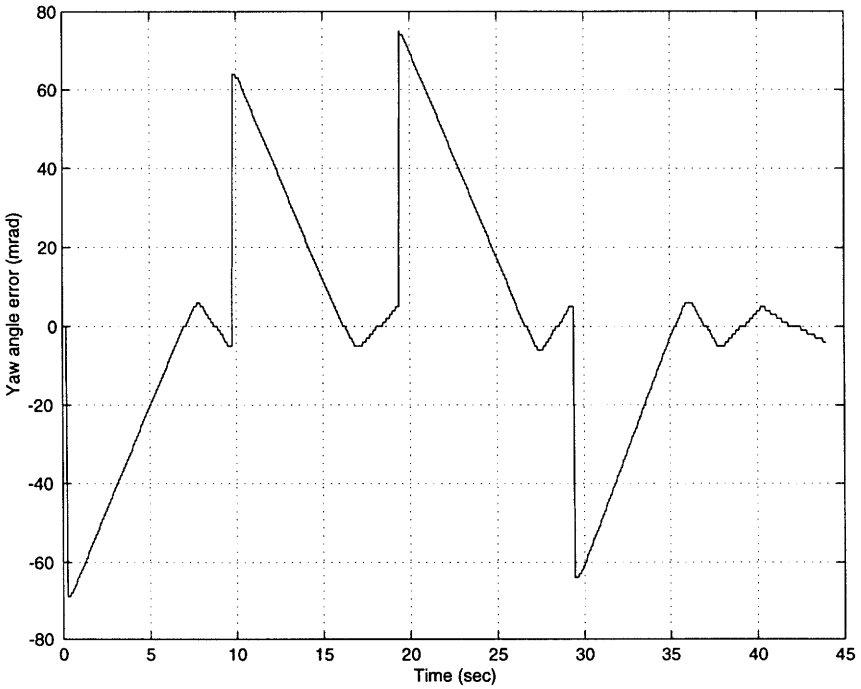

Figure 6-11: Step response of *MicroSat* yaw axis angular error with standard RLC control law with design parameters $\theta_{db} = 0.005$ rad, $\theta_r = 0.005071$ rad and $A_1 = 0.073159$. The RLC parameters chosen seek to approximate a time-fuel optimal controller with time weighting of $\lambda = 0.004$. The step input is of magnitude 69.7 mrad.

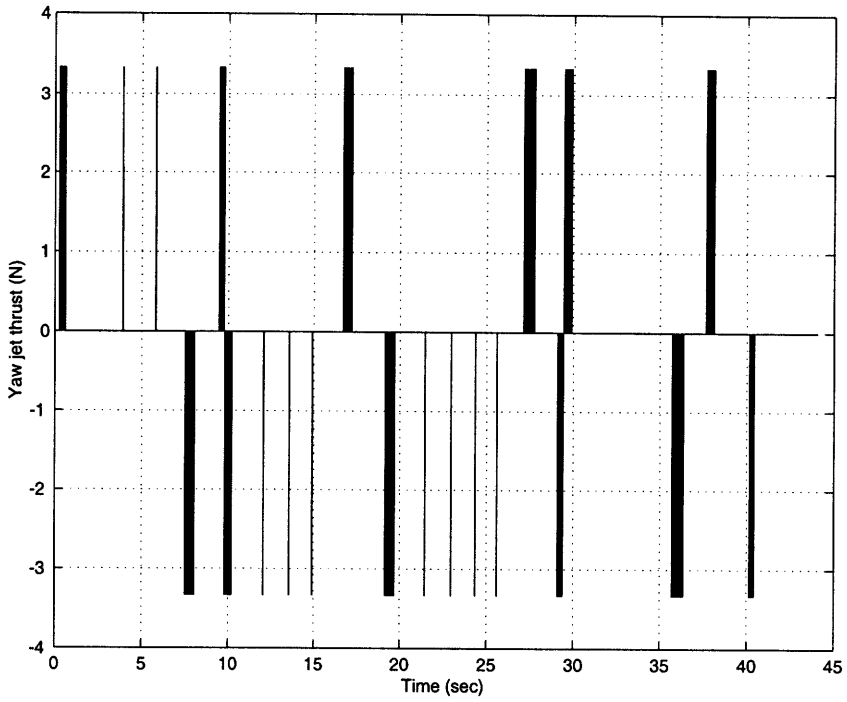

Figure 6-12: Pulse plot of the yaw thruster firings with standard RLC control law. Design parameters selected are $\theta_{db} = 0.005$ rad, $\theta_r = 0.005071$ rad and $A_1 = 0.073159$. The step input is of magnitude 69.7 mrad.

$$\begin{aligned} \theta_{short} &= \pm 0.007 \\ \dot{\theta}_{short} &= \pm 0.01 \\ \theta_{med} &= \pm 0.04 \\ \dot{\theta}_{med} &= \pm 0.15 \end{aligned} \tag{6.2}$$

These RLC boundary values are shown more formally in Figure 6-13 along with the actual short-pulse commands implemented in this thesis. The first design implemented thus has these short-pulse ranges and RLC parameters: $\theta_{db} = 0.01$ rad, $\theta_r = 0.0203$ rad, and $A_1 = 0.1231$. The step response and pulse plot is shown in Figures 6-14 and 6-15. From the step response, a clear limit cycle is seen to occur at every step response in the experimental run. Using RLC parameters $\theta_{db} = 0.003$ rad, $\theta_r = 0.005$ rad and $A_1 = 0.06326$ and the same good set of ranges, we get the response shown in Figures 6-16 and 6-17. We observe that a significant limit cycle is present at the start but the short-pulse regions gradually slow the rate down sufficiently so as

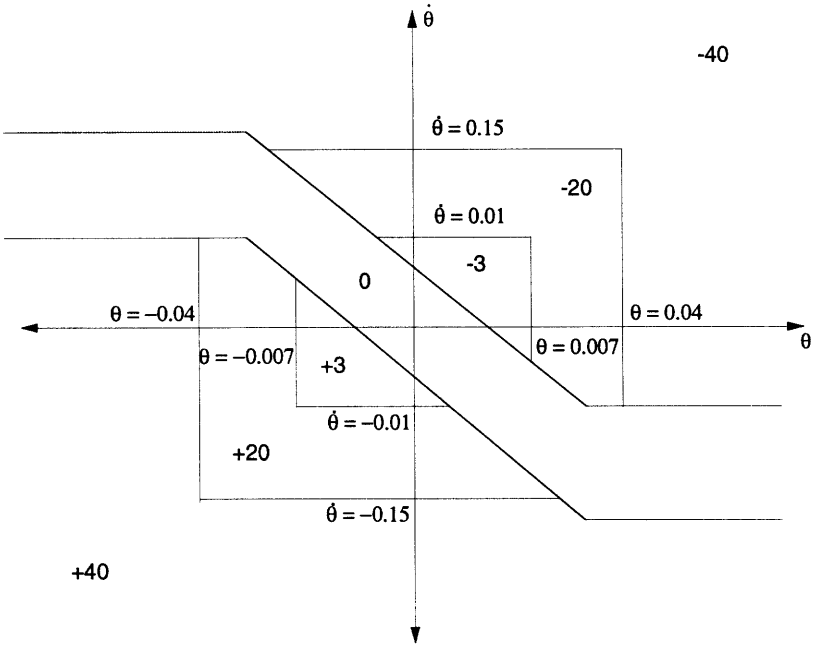

Figure 6-13: The RLC short-pulse boundary regions that correspond to $\theta_{short} = \pm 0.007$, $\theta_{med} = \pm 0.04$, $\dot{\theta}_{short} = \pm 0.01$, and $\dot{\theta}_{med} = \pm 0.15$ are shown in this figure. Note that also shown are the three different pulse widths implemented in both the *MicroSat* vehicle and in the simulations of the next section. The pulse widths shown are in units of milliseconds.

to increase the period of the limit cycle. This control design is certainly favored over the first design presented with respect to accuracy and fuel efficiency. This improvement is best illustrated by comparing the pulse commands of Figures 6-15 and 6-17. A better control system design, however, has the RLC parameters $\theta_{db} = 0.005$ rad, $\theta_r = 0.005071$ rad and $A_1 = 0.073159$ and the same short-pulse ranges of the last two designs. The step response and pulse commands for this improved design are shown in Figures 6-18 and 6-19. This parameter selection eliminates the limit cycle behavior and attains superb accuracy as demonstrated in Figure 6-18. The fuel efficiency is also increased as observed by comparing Figures 6-17 and 6-19. The drawback of this last design iteration is its slower time response compared to the second short-pulse RLC design. This makes sense since the time weighting, λ, used in this last design iteration is significantly higher. Since fuel efficiency is more important in our application, this final design is preferred.

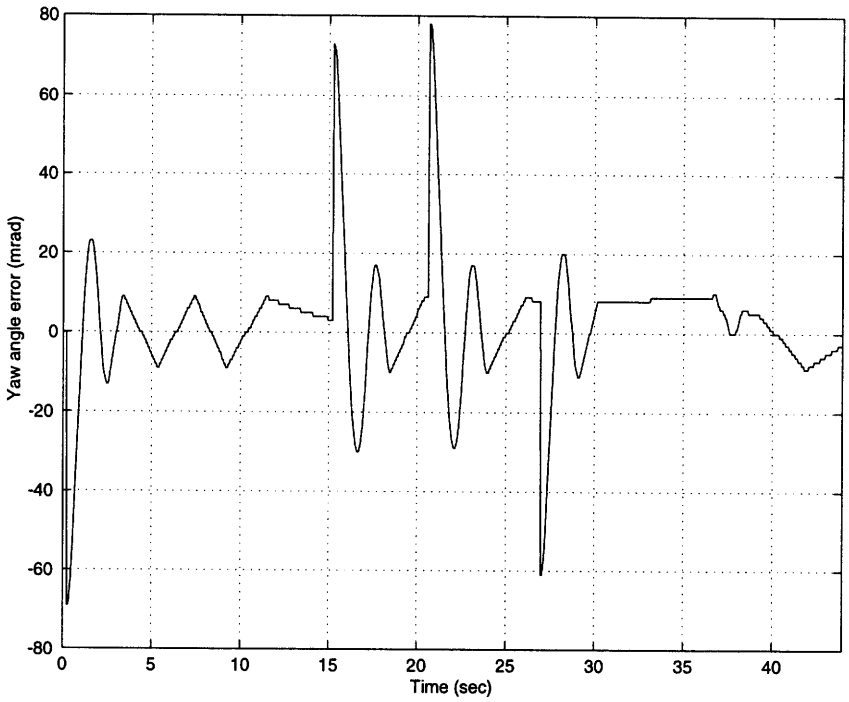

Figure 6-14: Yaw axis angular error response of the short-pulse RLC control algorithm with RLC parameters $\theta_{db} = 0.01$ rad, $\theta_r = 0.0203$ rad, and $A_1 = 0.1231$. The short-pulse regions are defined through the following ranges: $\theta_{short} = \pm 0.007$, $\theta_{med} = \pm 0.04$, $\dot{\theta}_{short} = \pm 0.01$, and $\dot{\theta}_{med} = \pm 0.15$. The step input is of magnitude 69.7 mrad.

6.2.5 Multiple Phase Plane Optimal Controller

In this section two different multiple phase plane optimal controllers are designed and the results are shown. Recall from the beginning of this chapter that a multiple phase plane controller design is a hybrid of the short-pulse RLC scheme with the tracking-fuel controller. In these experiments, the tracking-fuel optimal control algorithm is implemented when the states fall in the region of the state space corresponding to $\Delta\theta = 0.0005$ rad and $\Delta\omega = 0.02564$ rad/s. These ranges are set by calculating the maximum possible residual attitude error, $\Delta\theta$, and rate error, $\Delta\omega$, during one control cycle given the maximum allowable pulse of 40 ms. This design gives a more realistic framework in which to drive state errors very near the state space origin during a single control cycle. The choice of a larger operation range for the tracking-fuel formulation is also possible within the multiple phase plane algorithm. In this thesis, however, the short-pulse RLC formulation is given more weight in the multiple phase plane optimal controller because it is seen to produce less switching than the

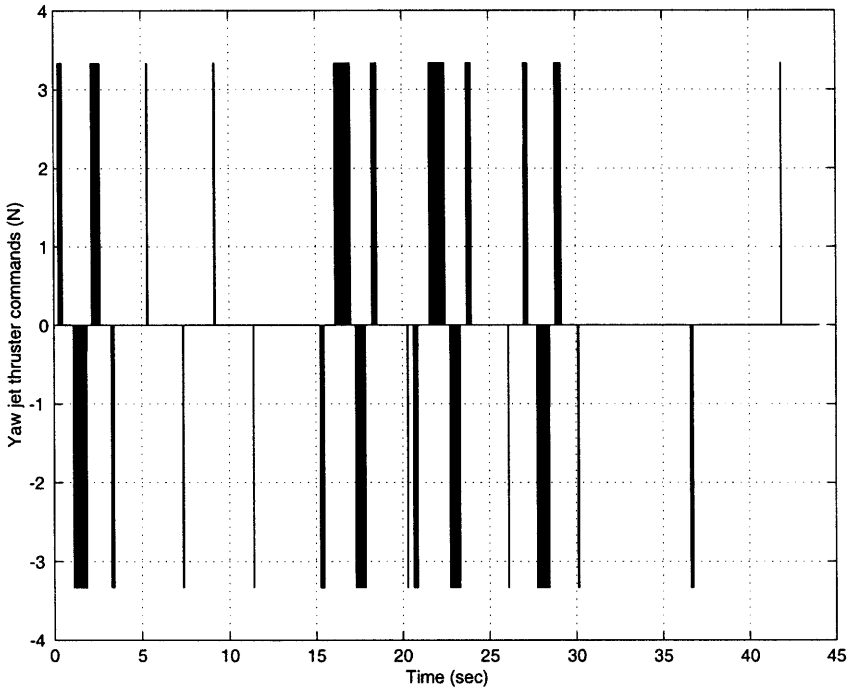

Figure 6-15: Yaw thruster pulse commands with the short-pulse RLC control algorithm and with RLC parameters $\theta_{db} = 0.01$ rad, $\theta_r = 0.0203$ rad. The short-pulse regions are defined through the following ranges: $\theta_{short} = \pm 0.007$, $\theta_{med} = \pm 0.04$, $\dot{\theta}_{short} = \pm 0.01$, and $\dot{\theta}_{med} = \pm 0.15$. The step input is of magnitude 69.7 mrad.

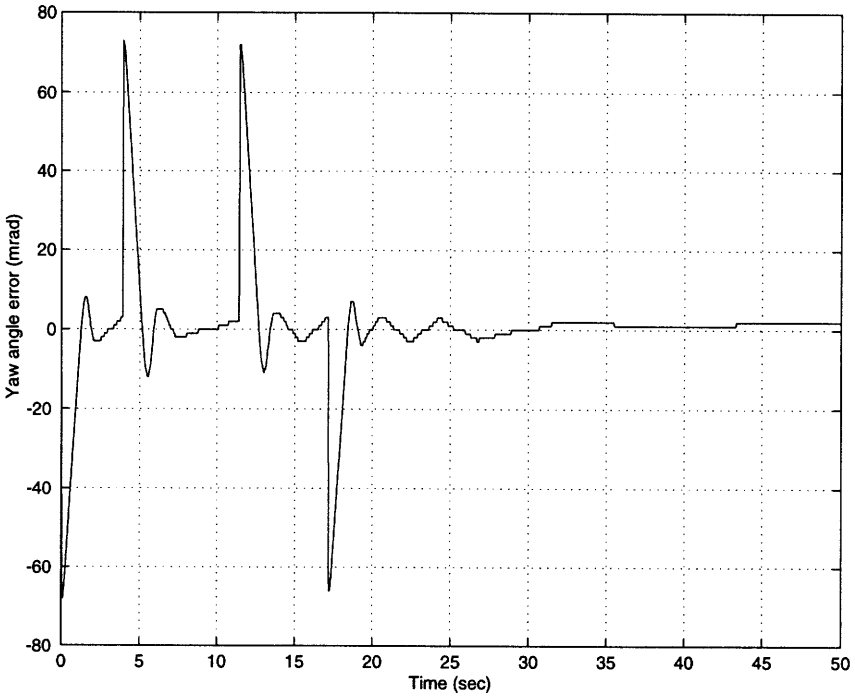

Figure 6-16: Yaw axis angular error response of the short-pulse RLC control algorithm with RLC parameters $\theta_{db} = 0.003$ rad, $\theta_r = 0.005$ rad and $A_1 = 0.06326$. The short-pulse regions are defined through the following ranges: $\theta_{short} = \pm 0.007$, $\theta_{med} = \pm 0.04$, $\dot{\theta}_{short} = \pm 0.01$, and $\dot{\theta}_{med} = \pm 0.15$. The input is a step of magnitude 69.7 mrad.

tracking-fuel optimal controller. The first design of the multiple phase plane optimal controller has the same RLC parameters and short-pulse ranges of the second short-pulse RLC design. The corresponding response plots are given in Figures 6-20 and 6-21. We observe a similar limit cycle behavior when the step response of Figure 6-20 is compared to the short-pulse RLC step response of Figure 6-16. This design is also less fuel efficient than the corresponding short-pulse RLC design. This is seen by comparing their respective pulse plots in Figures 6-17 and 6-21. A second multiple phase plane control design uses the RLC parameters and short-pulse ranges selected for the last design discussed in the previous section. The response plots for this design are illustrated in Figures 6-22 and 6-23. A limit cycle is still present in this last design as seen by the last step response occuring after the first 16 seconds. This last design is an improvement over the first multiple phase plane controller, but produces more fuel consumption than the short-pulse RLC algorithm with the same ranges and control parameters. A value of $k = 0.005$ is used for both designs above since it is found,

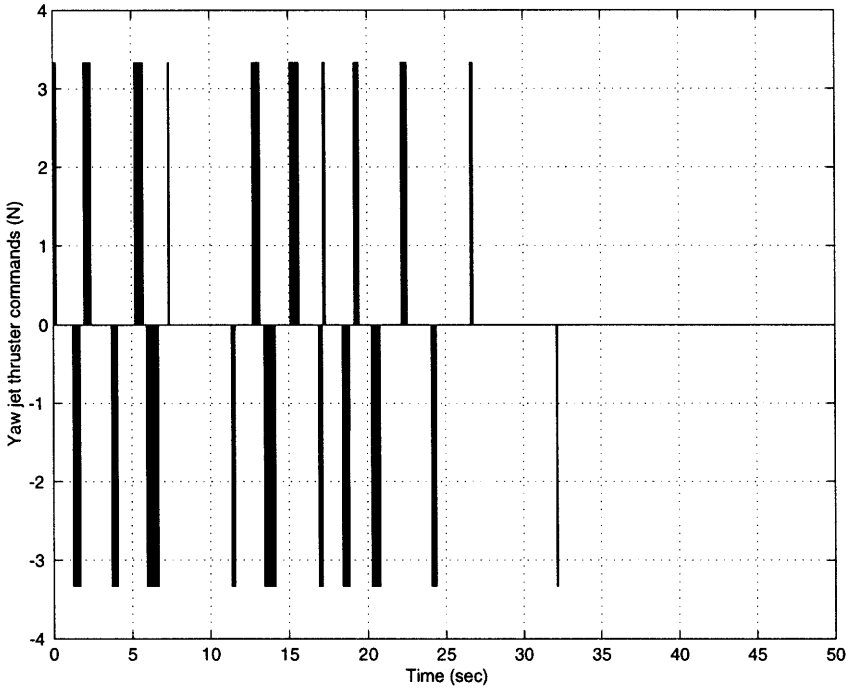

Figure 6-17: Yaw thruster pulse commands with the short-pulse RLC control algorithm and RLC parameters $\theta_{db} = 0.003$ rad, $\theta_r = 0.005$ rad and $A_1 = 0.06326$. The short-pulse regions are defined through the following ranges: $\theta_{short} = \pm 0.007$, $\theta_{med} = \pm 0.04$, $\dot{\theta}_{short} = \pm 0.01$, and $\dot{\theta}_{med} = \pm 0.15$. The step input is of magnitude 69.7 mrad.

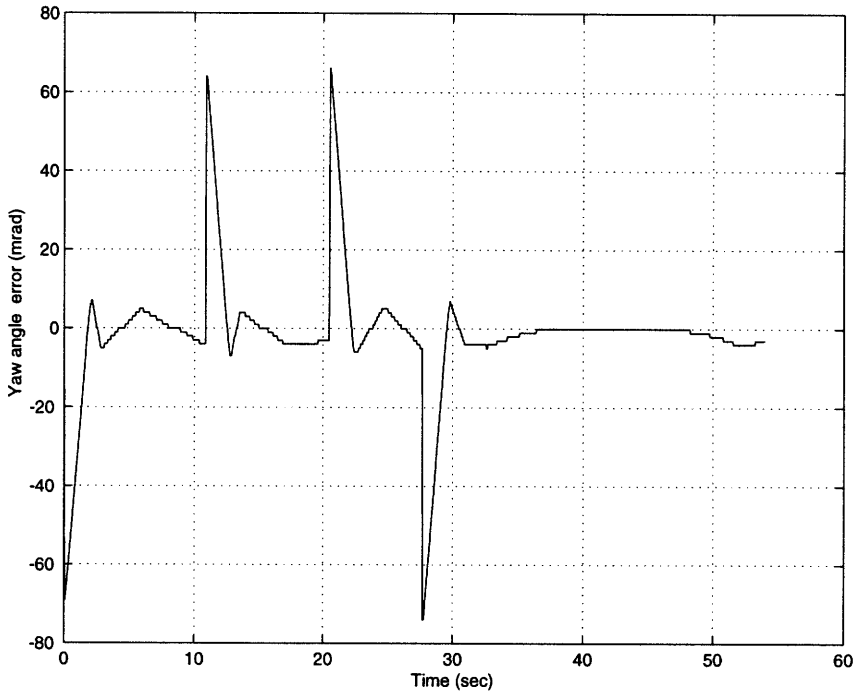

Figure 6-18: Yaw axis angular error response of the short-pulse RLC control algorithm with RLC parameters $\theta_{db} = 0.005$ rad, $\theta_r = 0.005071$ rad and $A_1 = 0.073159$. The short-pulse regions are defined through the following ranges: $\theta_{short} = \pm 0.007$, $\theta_{med} = \pm 0.04$, $\dot{\theta}_{short} = \pm 0.01$, and $\dot{\theta}_{med} = \pm 0.15$. The input is a step command of magnitude 69.7 mrad.

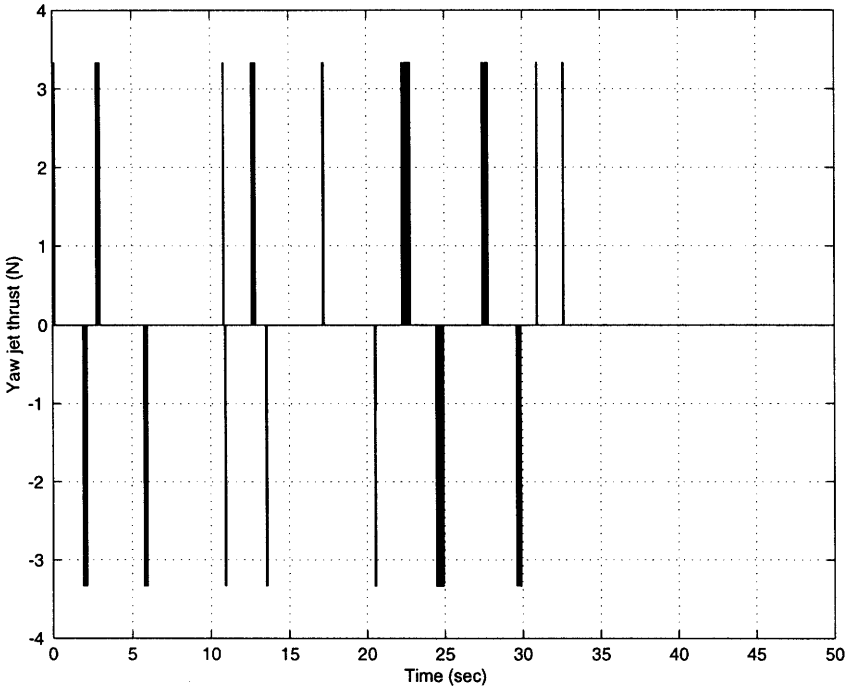

Figure 6-19: Yaw thruster pulse commands with the short-pulse RLC control algorithm and RLC parameters $\theta_{db} = 0.005$ rad, $\theta_r = 0.005071$ rad and $A_1 = 0.073159$. The short-pulse regions are defined through the following ranges: $\theta_{short} = \pm 0.007$, $\theta_{med} = \pm 0.04$, $\dot{\theta}_{short} = \pm 0.01$, and $\dot{\theta}_{med} = \pm 0.15$. The step input is of magnitude 69.7 mrad.

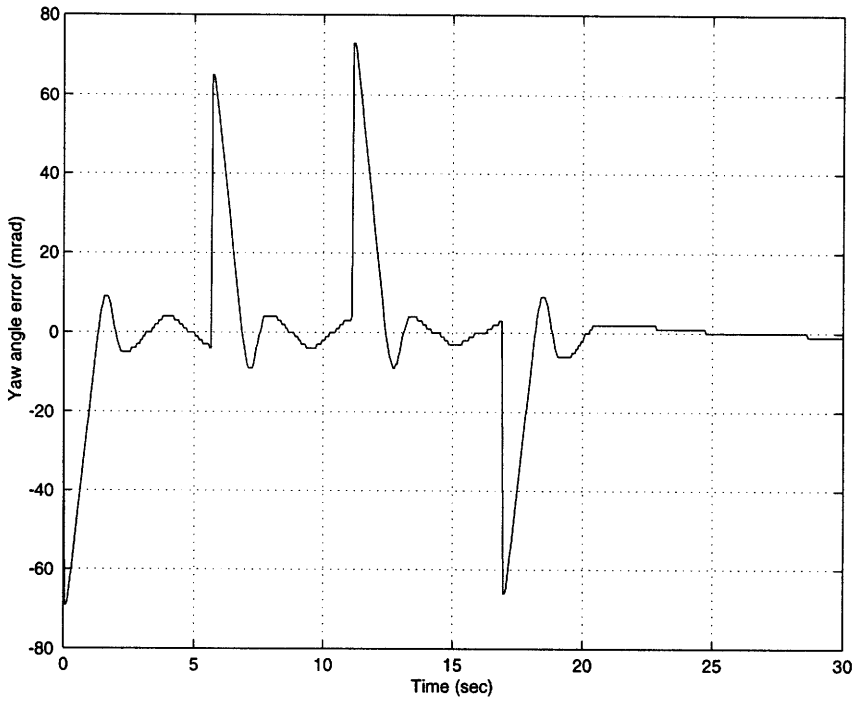

Figure 6-20: Experimental step response for the multiple phase plane optimal controller for a step input of 69.7 mrad. The short-pulse RLC parameters used are $\theta_{db} = 0.003$ rad, $\theta_r = 0.005$ rad and $A_1 = 0.06326$ with ranges $\theta_{short} = \pm 0.007$, $\theta_{med} = \pm 0.04$, $\dot{\theta}_{short} = \pm 0.01$, and $\dot{\theta}_{med} = \pm 0.15$. The tracking-fuel weighting factor used is $k = 0.005$.

through simulation, to work best in achieving a well balanced closed-loop performance that reduces both the limit cycle fuel consumption and the steady state error.

Based on preliminary experiments presented in this chapter on the four types attitude controllers, the short-pulse RLC controller is recommended for the *MicroSat* prototype since it is seen to be slightly more fuel efficient than the other three algorithms discussed. Its closest competitor is the multiple phase plane optimal controller. This algorithm produces slightly less fuel-efficient responses and no apparent improvement in steady-state accuracy and stabilization. The multiple phase plane optimal controller, however, should not be discounted so rapidly. This control algorithm seems a very promising alternative for fuel-optimal attitude control as will be seen in the next section.

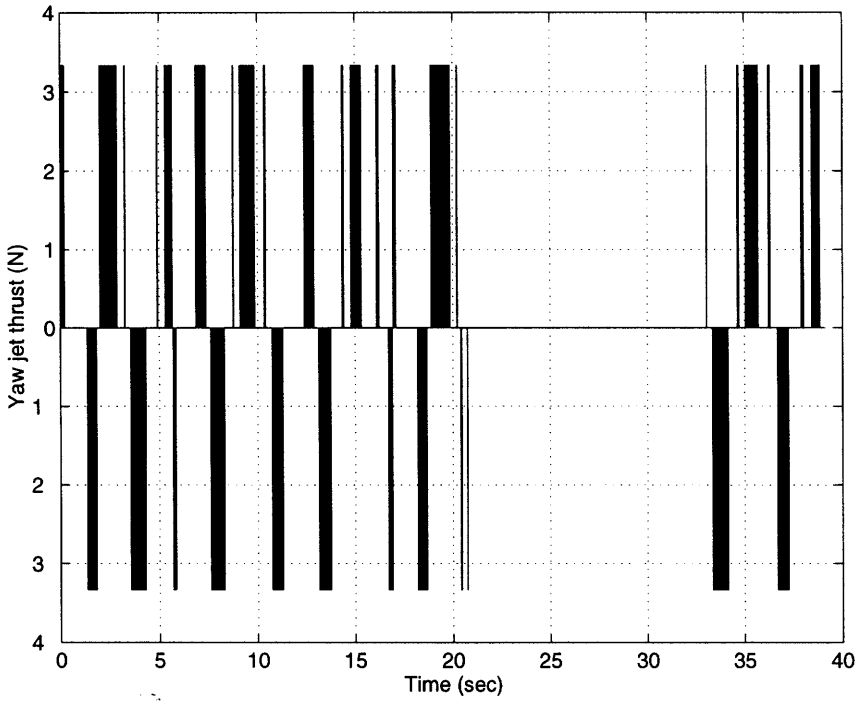

Figure 6-21: Experimental pulse commands for the multiple phase plane optimal controller for a step input of 69.7 mrad. The short-pulse RLC parameters used are $\theta_{db} = 0.003$ rad, $\theta_r = 0.005$ rad and $A_1 = 0.06326$ with ranges $\theta_{short} = \pm 0.007$, $\theta_{med} = \pm 0.04$, $\dot{\theta}_{short} = \pm 0.01$, and $\dot{\theta}_{med} = \pm 0.15$. The tracking-fuel weighting factor used is $k = 0.005$.

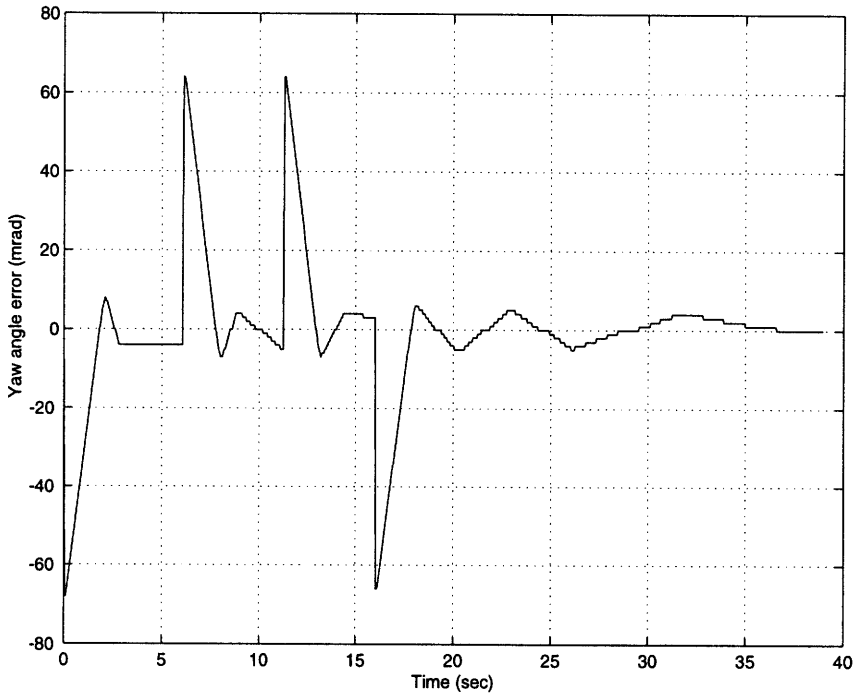

Figure 6-22: Experimental step response for the multiple phase plane optimal controller for a step input of 69.7 mrad. The short-pulse RLC parameters used are $\theta_{db} = 0.005$ rad, $\theta_r = 0.005071$ rad and $A_1 = 0.073159$ with ranges $\theta_{short} = \pm 0.007$, $\theta_{med} = \pm 0.04$, $\dot{\theta}_{short} = \pm 0.01$, and $\dot{\theta}_{med} = \pm 0.15$. The tracking-fuel weighting factor used is $k = 0.005$.

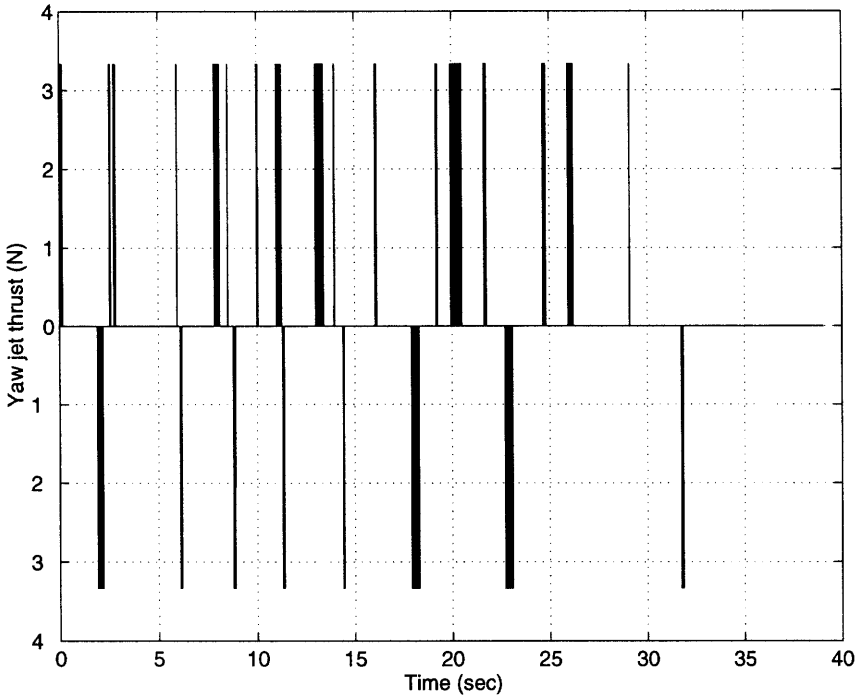

Figure 6-23: Experimental pulse commands for the multiple phase plane optimal controller for a step input of 69.7 mrad. The short-pulse RLC parameters used are $\theta_{db} = 0.005$ rad, $\theta_r = 0.005071$ rad and $A_1 = 0.073159$ with ranges $\theta_{short} = \pm 0.007$, $\theta_{med} = \pm 0.04$, $\dot{\theta}_{short} = \pm 0.01$, and $\dot{\theta}_{med} = \pm 0.15$. The tracking-fuel weighting factor used is $k = 0.005$.

6.3 Simulation Results

In this section we present simulations of the closed-loop step responses for the four controllers. In the simulations below, the vehicle is given an initial condition and commanded to zero body rate and position (attitude). The three axes of rotation are assumed to be decoupled so that a jet firing only produces torque about its corresponding axis. We first show the simulations for the PWM/PD control law, followed by the standard RLC, and the short-pulse RLC. Lastly we include the simulations for the multiple phase-plane controller design. In all the ensuing simulations we are consistent with the representation of the hardware and software constraints. The two most important considerations are the minimum reliable burn time that can be provided by the hardware and the inability of the software to overlap pulses over mulitple control periods. The first consideration stems from the finite rise and fall time of the solenoid valves when they open and close to produce thrust. The minimum pulse-width that is allowed to be commanded is 3 ms given the specified characteristic time constants for the valves (refer to Chapter 5 for more details). Thus, this serves as a deadband in the control system. The second is a direct result of LLNL's requirement of a simplified real-time control software architecture for practical implementation. As a result, the maximum pulse width is set to 40 ms for control purposes. Both these constraints are included as part of the simulated control system.

6.3.1 Pulse-Width Modulated Proportional Derivative Control

In order to gain insight into the limit cycling behavior observed in the laboratory when very small terminal tolerances are used, we decided to simulate the step response of the vehicle under PWM/PD control. This control law is the first design in the process of finding a simple control solution that yields efficient and accurate attitude maneuvers. The step responses for the three axes are shown in Figures 6-24, 6-25, and 6-26. Their corresponding pulse plots are in Figures 6-27, 6-28, and 6-29. These responses are obtained using control gains of $K_p = 20$ and $K_d = 5$ for the roll axis and $K_p = 20$ and

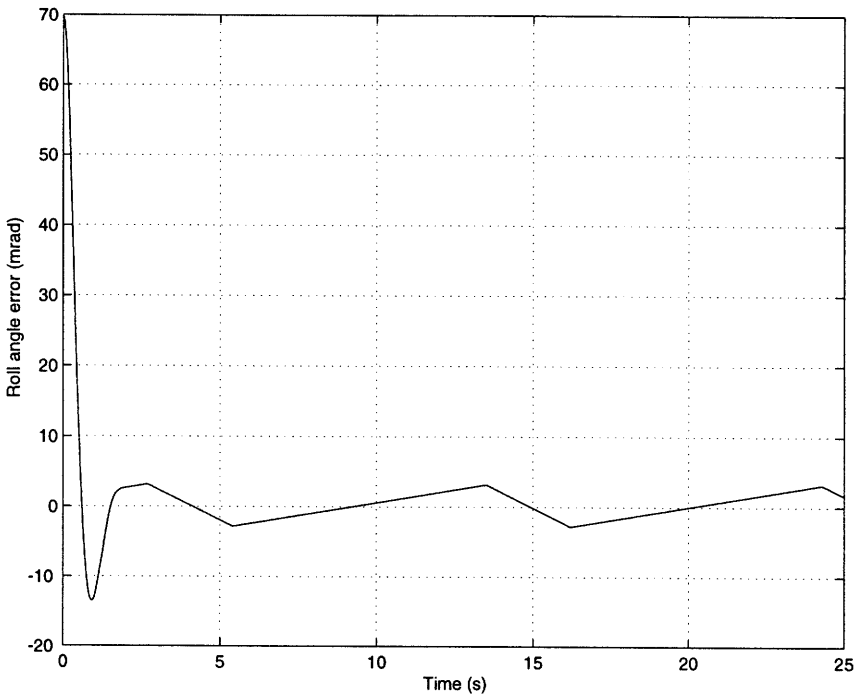

Figure 6-24: Simulated angular error response for the roll axis using a PWM/PD controller for a step input of 69.7 mrad. The gains are $K_p = 20$ and $K_d = 5$.

$K_d = 8$ for the remaining two axes. The roll axis having less inertia associated with it, need not have the added damping provided by an increased value of K_d. We recall that the closed loop bandwidth for this linear system without actuator nonlinearities can be given by the relations in Chapter 2. Using Equation 2.9 we can calculate an upper bound for the system bandwidth of $\omega_n \approx 2.77$ rad/s for the pitch and yaw axis and $\omega_n \approx 8.16$ rad/s for the roll axis.

The responses clearly show that a limit cycle is present in the responses of all three axes. The roll axis response appears to have the highest-frequency limit cycle. The response for the pitch and yaw axis are almost identical since the inertia values differ only by less than 1% and the jet sizes are the same. The pulse plans show that initially very frequent valve switching is required in all cases to achieve the steady state limit cycle. The length of the pulses get shorter after the steady state is reached. In efforts to reduce the fuel consumed in the steady state mode, we can increase the stiffness and damping of the closed loop system to $K_p = 26.3$ and $K_d = 15.1$. The step response and pulse plot for the yaw axis using these gains is shown in Figures 6-30 and 6-31.

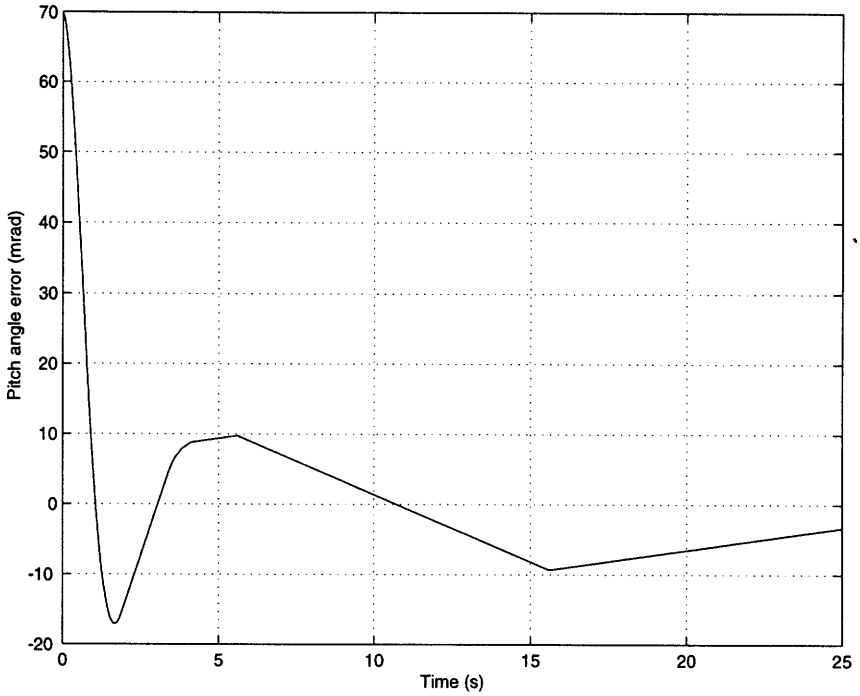

Figure 6-25: Simulated angular error response for the pitch axis using a PWM/PD controller for a step input of 69.7 mrad. The gains are $K_p = 20$ and $K_d = 8$.

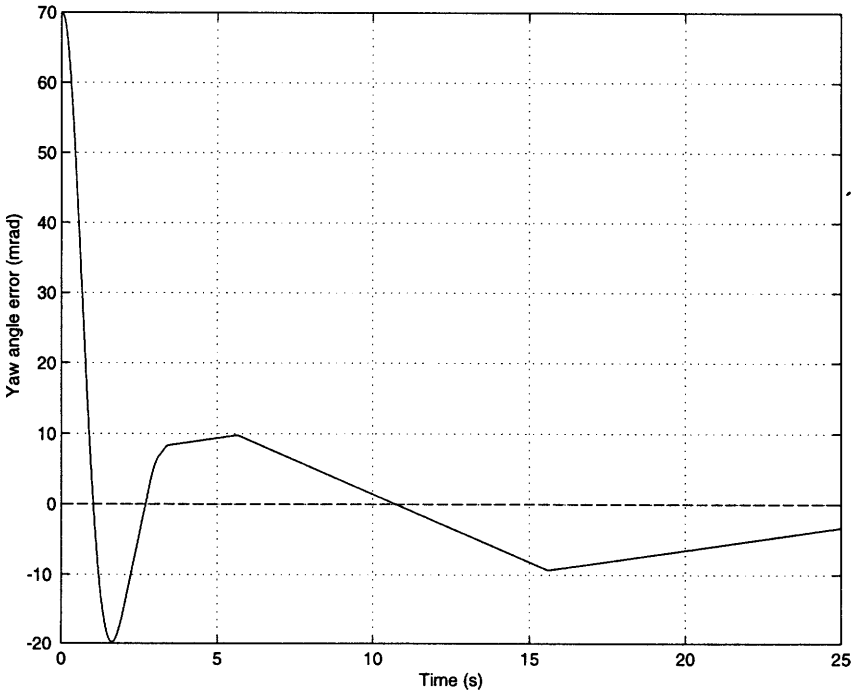

Figure 6-26: Simulated angular error response for the yaw axis using a PWM/PD controller for a step input of 69.7 mrad. The gains are $K_p = 20$ and $K_d = 8$.

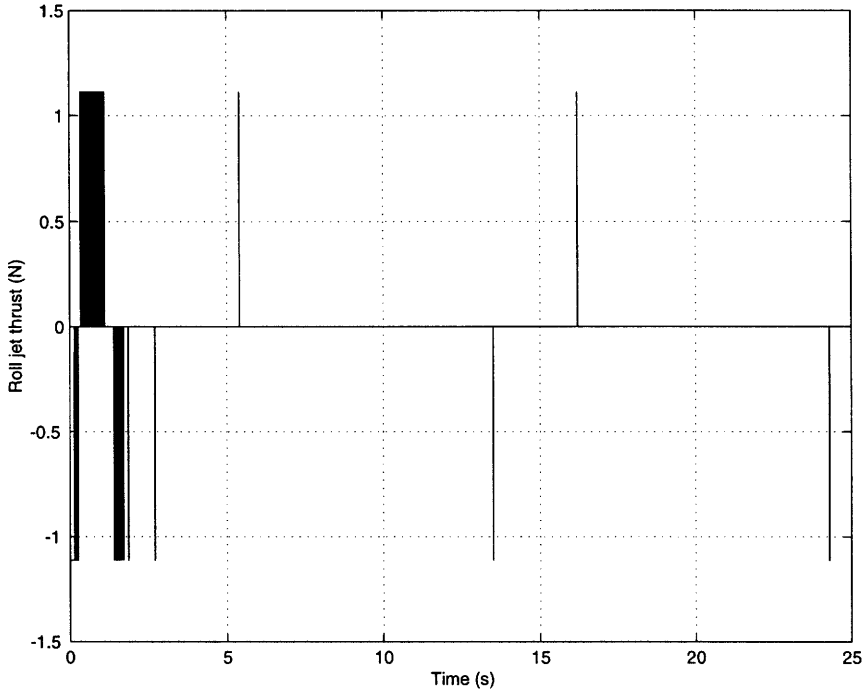

Figure 6-27: Simulated pulse commands for the roll axis using a PWM/PD controller. This response corresponds to a step input of 69.7 mrad. The gains are $K_p = 20$ and $K_d = 5$.

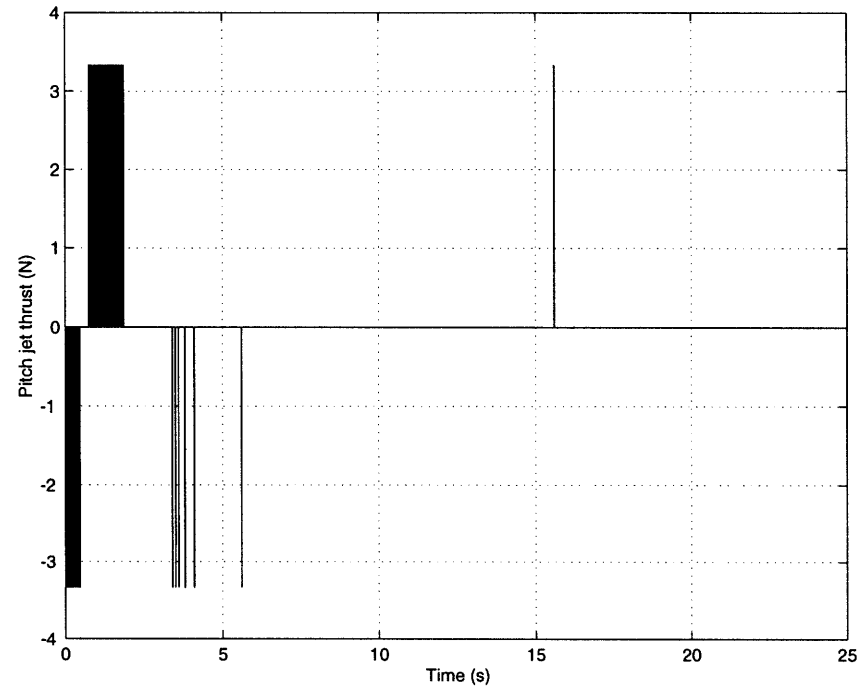

Figure 6-28: Simulated pulse commands for the pitch axis using a PWM/PD controller. This response corresponds to a step input of 69.7 mrad. The gains are $K_p = 20$ and $K_d = 8$.

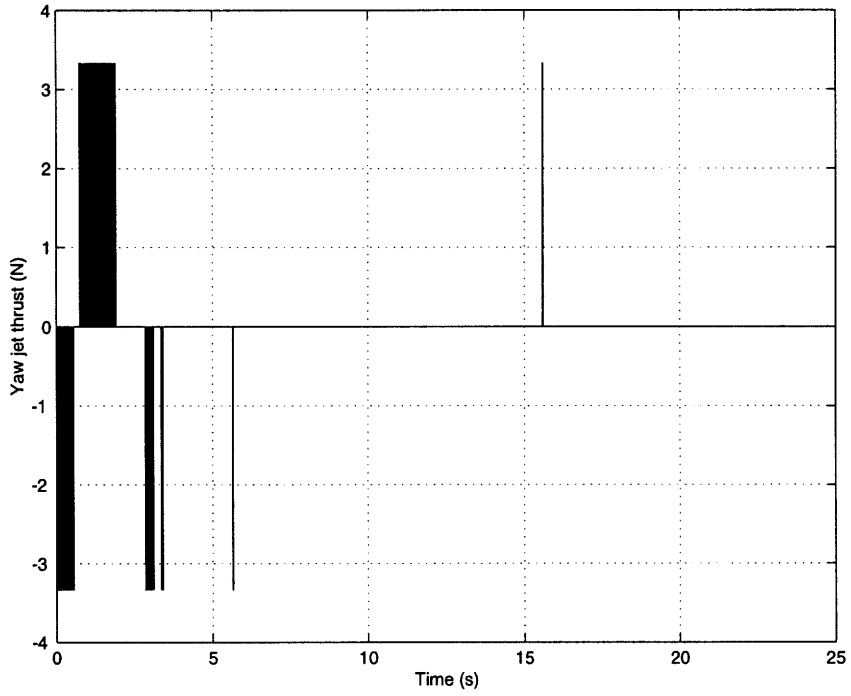

Figure 6-29: Simulated pulse commands for the yaw axis using a PWM/PD controller. This response corresponds to a step input of 69.7 mrad. The gains are $K_p = 20$ and $K_d = 8$.

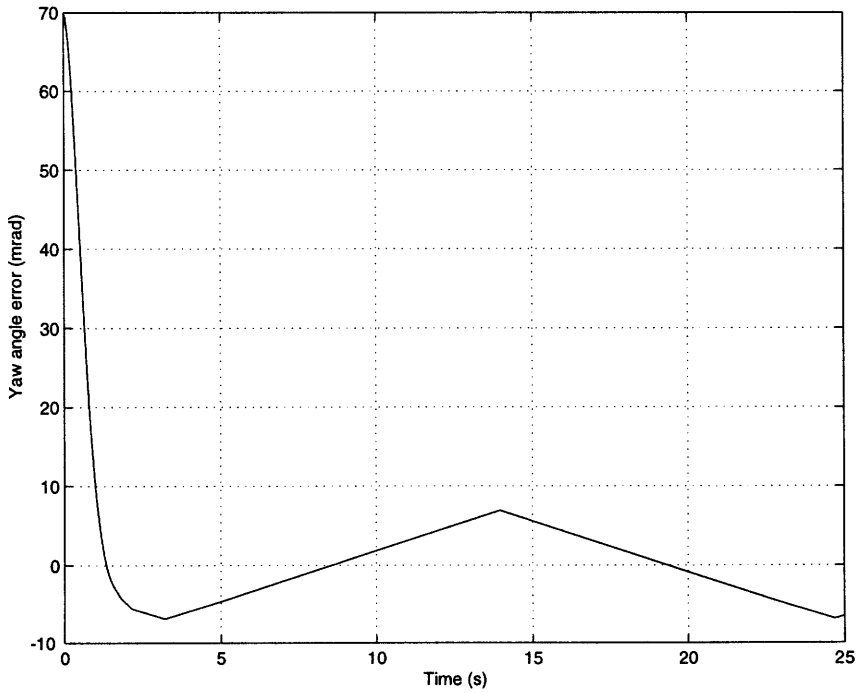

Figure 6-30: Simulated step response for the yaw axis using a PWM/PD controller for a step input of 69.7 mrad. The gains are $K_p = 26.3$ and $K_d = 15.1$.

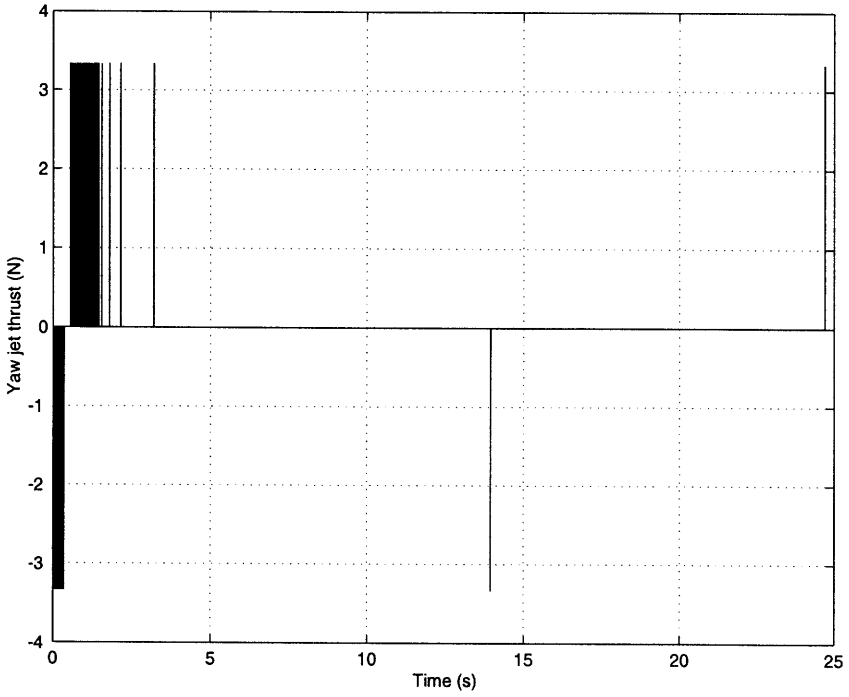

Figure 6-31: Simulated pulse commands for the yaw axis using a PWM/PD controller. This response corresponds to a step input of 69.7 mrad. The gains are $K_p = 26.3$ and $K_d = 15.1$.

We observe the less frequent pulsing and thus the fuel savings advantage of Figures 6-30 and 6-31 compared to Figures 6-26 and 6-29 respectively. Increasing the gains had the effect of slowing down the limit cycle and thus making pulsing more infrequent. The bang-bang nature of the control system is thus minimized.

6.3.2 Standard RLC Algorithm

Simulations of the standard RLC control algorithm for three sets of design parameters is presented in this section. Only the yaw axis is used in the simulations illustrated here. The first simulation, shown in Figures 6-32 and 6-33, has values for the RLC parameters of $\theta_{db} = 0.01$ rad, $\theta_r = 0.0203$ rad, and $A_1 = 0.1231$ that correspond to a time-fuel optimal control with time weighting of $\lambda = 0.4$. We see that a limit cycle behavior exists in steady state with a relatively long period of 28 sec. In addition, the desired 10 mrad deadband is clearly existent in the simulation as the bound on the attitude error. The pulse plan of Figure 6-33 clearly shows an improvement in fuel efficiency from any of the PWM/PD simulations. The step response, shown in Figure

6-32, also has similar rise times to the PWM/PD case. A second simulation with a reduced deadband of $\theta_{db} = 0.003$ rad and parameters $\theta_r = 0.005$ rad and $A_1 = 0.06326$ is shown in Figures 6-35 and 6-36. These parameters map approximately to a time-fuel optimal controller with $\lambda = 0.04254$, which leads to a more time stringent performance requirement than the last case. As observed from the step response in Figure 6-35, a shorter period limit cycle of 8 sec is present due to the decreased deadband. Thus, more fuel will be consumed as a result of more frequent switching. This is evident in the pulse plot shown in Figure 6-36. This makes sense because the error tolerance has been reduced by a factor of three while the impulse magnitude has remained unchanged. In addition, the rise time for this response is slightly slower than the first case response. A third simulation with an intermediate deadband value of $\theta_{db} = 0.005$ rad is illustrated in Figures 6-37 and 6-38. This controller has parameters $\theta_r = 0.005071$ rad and $A_1 = 0.073159$ which correspond to a time weighting of $\lambda = 0.004$. This control emphasizes fuel efficiency over faster response times more so than the other two cases. The step response of Figure 6-37 shows a twofold improvement in the limit cycle behavior (period of 16 sec) compared to the last case. The response is slower, however, than the other two simulation cases. Furthermore, like in the last two cases the error bound of the limit cycle is seen to equal the selected deadband. Consequently, the controller deadband is highly influential in the control of the damping characteristics in the closed-loop system. Thus, an analogy to a derivative gain term is quite valid, only that it works in the opposite direction. An increase in θ_{db} results in decreased closed-loop damping andvice-versa. In addition to its effect on system damping, θ_{db} also directly affects the steady state fuel consumption. In general, the wider the deadband is the less the fuel consumption. This happens up to a point, however. Although it is true that as the deadband is initially increased the better the fuel efficiency becomes, it has been observed by Weisenberg [20] that after increasing θ_{db} past a certain point fuel consumption begins to increase only again to decrease. This behavior, named the steady state "fuel-bump", was first encountered by the attitude control designers for the Magellan spacecraft. Figure 6-39 illustrates the basic behavior of the fuel bump.

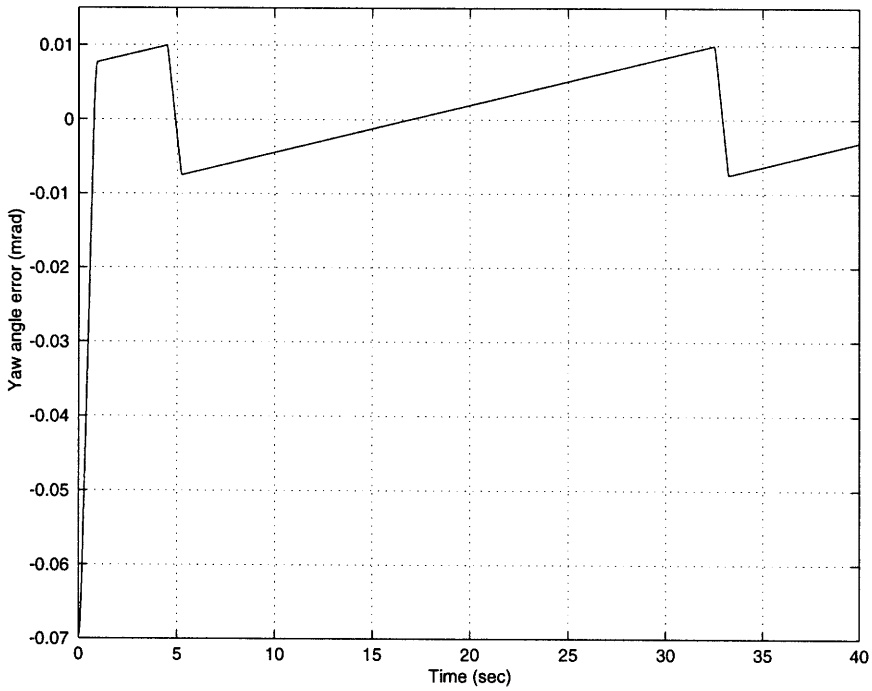

Figure 6-32: Simulated angular error response for the yaw axis using a standard RLC control law for a step input of 69.7 mrad. The RLC parameters used in this simulation are $\theta_{db} = 0.01$ rad, $\theta_r = 0.0203$ rad, and $A_1 = 0.1231$.

The sudden increase in fuel consumption as θ_{db} is increased is caused by coupling torques generated about the other perpendicular axes. The deadband, being wide enough at the location fuel bump, now gives the inter-axis torques sufficient time to influence the dynamics of the axis under control. For further detail into this fuel-efficiency/controller deadband coupling relationship refer to Weisenberg [20].

6.3.3 Short-Pulse RLC Algorithm

Simulations of the short-pulse or variable pulse RLC algorithm for the same three sets of parameters as used in the last section are presented in this section of the thesis. Like the standard RLC case, in this section we only consider yaw axis control in the ensuing simulations. The study of the phase plane control of a single axis with the linear uncoupled model assumed is perfectly valid as is seen througout the thesis. We should note the significant improvement of the step responses over the last two control algorithms. Moreover, in all the short- pulse RLC simulations the experimentally-selected short-pulse boundary ranges of section 6.1 are used. This is

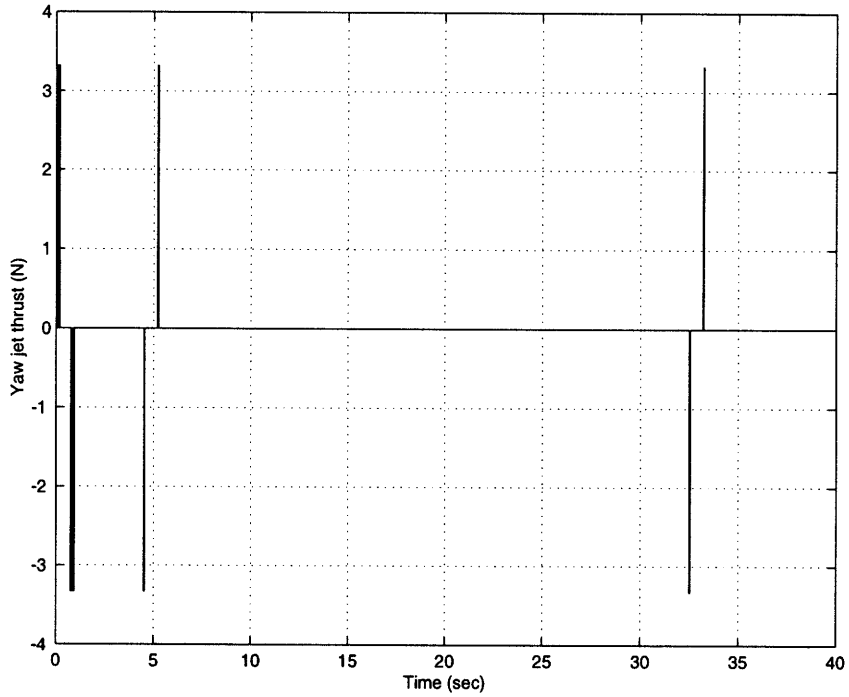

Figure 6-33: Simulated pulse commands for the standard RLC control algorithm for a step input of 69.7 mrad. The RLC parameters used are $\theta_{db} = 0.01$ rad, $\theta_r = 0.0203$ rad, and $A_1 = 0.1231$.

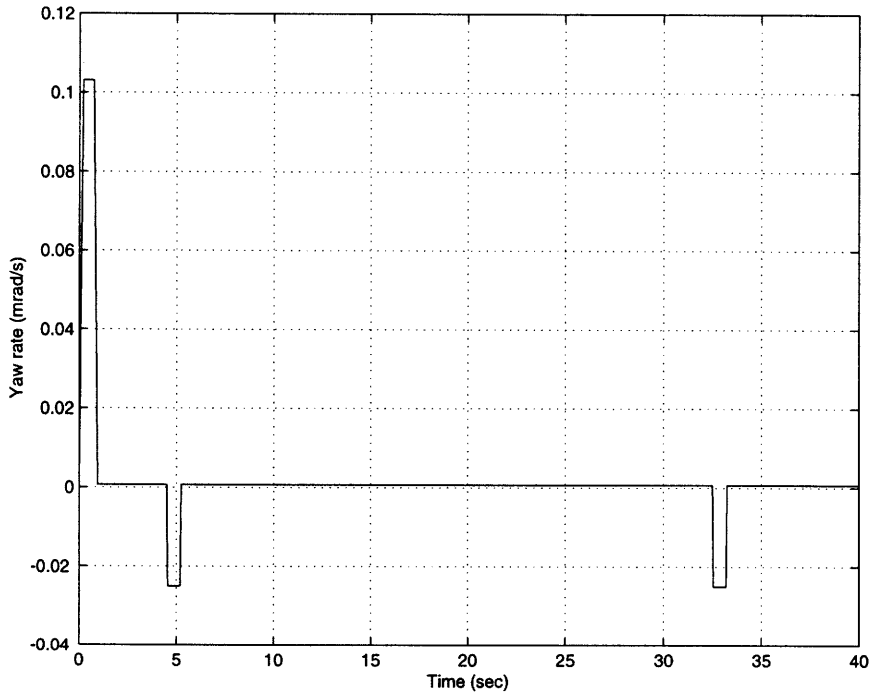

Figure 6-34: Simulated rate response for the standard RLC control algorithm for a step input of 69.7 mrad. The RLC parameters used are $\theta_{db} = 0.01$ rad, $\theta_r = 0.0203$ rad, and $A_1 = 0.1231$.

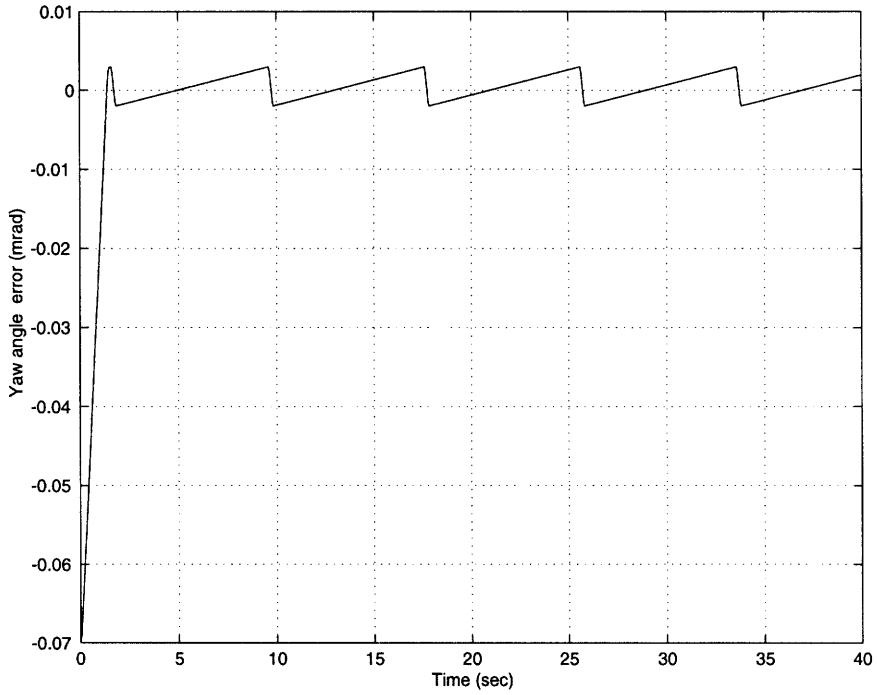

Figure 6-35: Simulated angular error response for the yaw axis using a standard RLC control law for a step input of 69.7 mrad. The RLC parameters used in this simulation are $\theta_{db} = 0.003$ rad,$\theta_r = 0.005$ rad and $A_1 = 0.06326$.

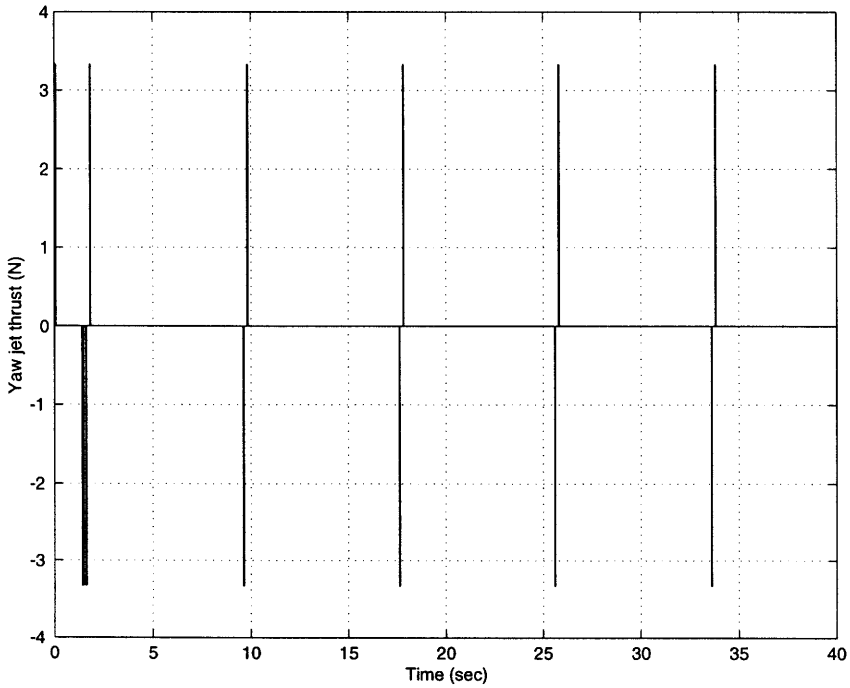

Figure 6-36: Simulated pulse commands for the standard RLC control algorithm for a step input of 69.7 mrad. The RLC parameters used are $\theta_{db} = 0.003$ rad, $\theta_r = 0.005$ rad, $A_1 = 0.06326$.

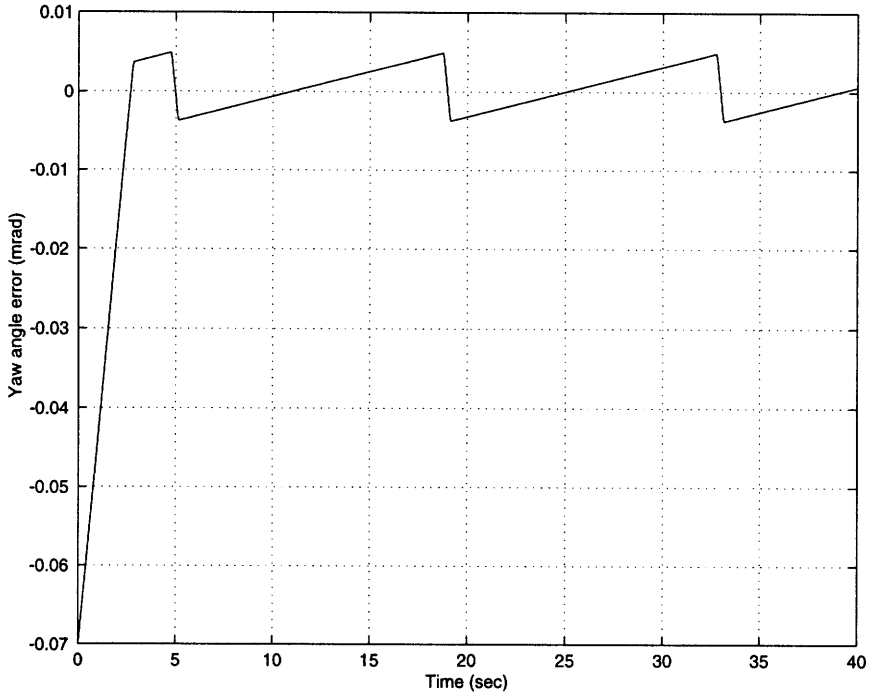

Figure 6-37: Simulated angular error response for the yaw axis using a standard RLC control law for a step input of 69.7 mrad. The RLC parameters used in this simulation are $\theta_{db} = 0.005$ rad, $\theta_r = 0.005071$ rad and $A_1 = 0.073159$.

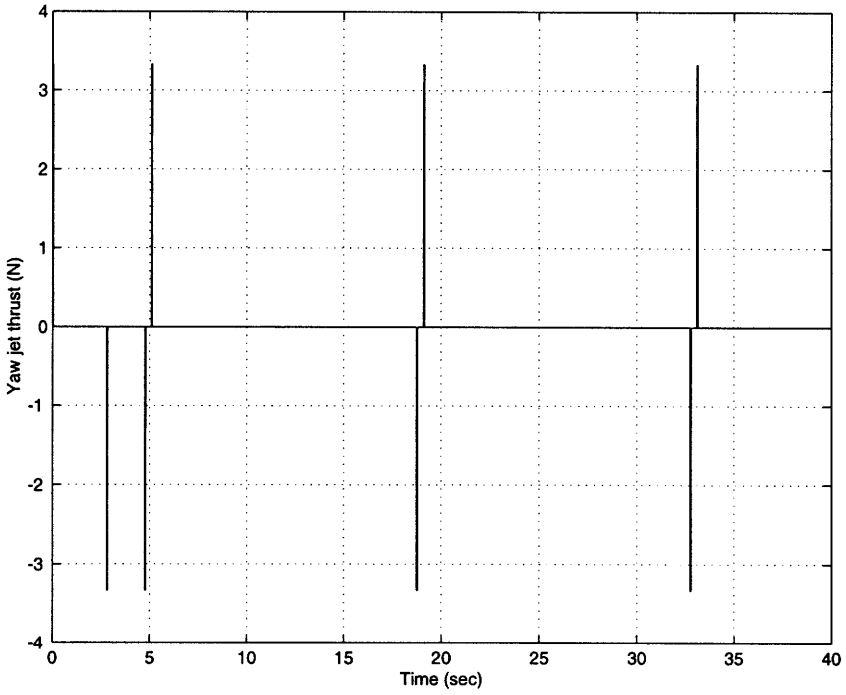

Figure 6-38: Simulated pulse commands for the standard RLC control algorithm for a step input of 69.7 mrad. The RLC parameters used are $\theta_{db} = 0.005$ rad, $\theta_r = 0.005071$ rad and $A_1 = 0.073159$.

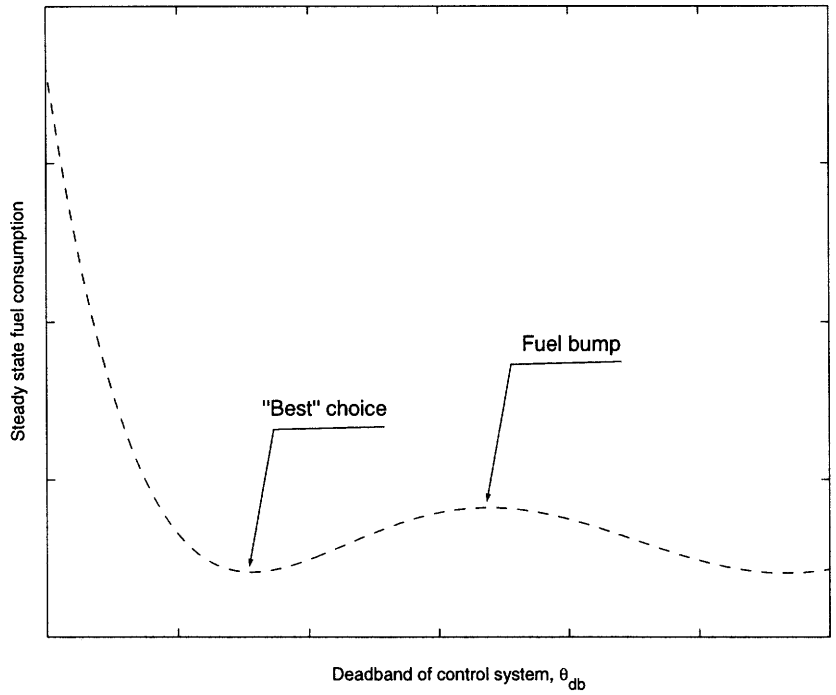

Figure 6-39: The fuel-bump phenomena existent in RLC type phase planes. The trough immediately before the bump in the figure is thought to correspond to the best choice for the deadband, θ_{db}. The figure labels these two sites.

assumed for the purpose of comparing the simulations to the experimental data of section 6.1.4. Figures 6-40 and 6-41 illustrate the step response and pulse plot for a short-pulse RLC control algorithm with parameters $\theta_{db} = 0.01$ rad, $\theta_r = 0.0203$ rad, and $A_1 = 0.1231$. As in the equivalent standard RLC case we observe a similar limit cycle behavior but with a longer period of 30 s as well as similar transient response. The difference between the standard and this short-pulse RLC design mainly lies in the increased overshoot and subsequent reduction of fuel expenditure of the latter control algorithm during steady state. See Figures 6-34 and 6-42 for the simulated rate dynamics of the standard RLC and short-pulse RLC with the above mentioned parameters. From these two plots it can be observed that the pulse widths are shorter for the short-pulse RLC algorithm thereby decreasing fuel consumption in the long run. One should note that the pulse widths are proportional to the change caused in the angular rate about an axis of the vehicle. The short-pulse RLC algorithm is also simulated with the design parameters $\theta_{db} = 0.003$ rad, $\theta_r = 0.005$ rad and

$A_1 = 0.06326$. As shown in Figures 6-44 and 6-45 this set of parameters eliminates the limit cycling present in all the other cases thus far. The rates are nulled out (see Figure 6-43) before the controller has a chance to eliminate the position error and since this final state is located within the deadband there is no associated pulse command. A residual error in position of 2.5 mrad thus exists in the closed-loop response that cannot be eliminated. This set of parameters seems to work extremely well both in transient and steady state when errors of up to 4% can be tolerated. This means that if the controller has perfect knowledge of the plant and noise is within a fraction of the deadband, the natural limit cycle can be eliminated. A final simulation is carried out for the case of RLC parameters $\theta_{db} = 0.005$ rad, $\theta_r = 0.005071$ rad and $A_1 = 0.073159$. As shown in Figures 6-47 and 6-48, the limit cycle is observed to exist with a period of 22.5 sec. In comparison to the standard RLC with the same parameters, this control algorithm increases the fuel efficiency and keeps the same fast transient performance shown in Figure 6-37. In general, the short-pulse RLC scheme as demonstrated in this section is an improved solution to the standard algorithm in terms of the fuel efficiency gained. Furthermore, it also outperforms the PWM/PD control law presented in the beginning of section 6.3 during the steady state stabilization period, although it slightly lags the linear controller in terms of a quick time response.

6.3.4 Multiple Phase Plane Optimal Controller

In the ensuing simulations of the multiple phase plane optimal controller, the size of the operation range for the tracking-fuel optimal controller is the same as implemented in the experimental runs. We first present the simulation of the multiple phase plane optimal control design with short-pulse RLC parameters $\theta_{db} = 0.005$ rad, $\theta_r = 0.005071$ rad and $A_1 = 0.073159$. The step response and pulse plot is shown in Figures 6-49 and 6-48. Again, a limit cycle behavior is present in the response with a period of 22.5 sec. In fact, the step response and pulse plan are identical to the simulation of the short- pulse RLC design with the same parameters. To obtain better insight into this result we show the phase plane plot in Figures 6-51 and 6-52

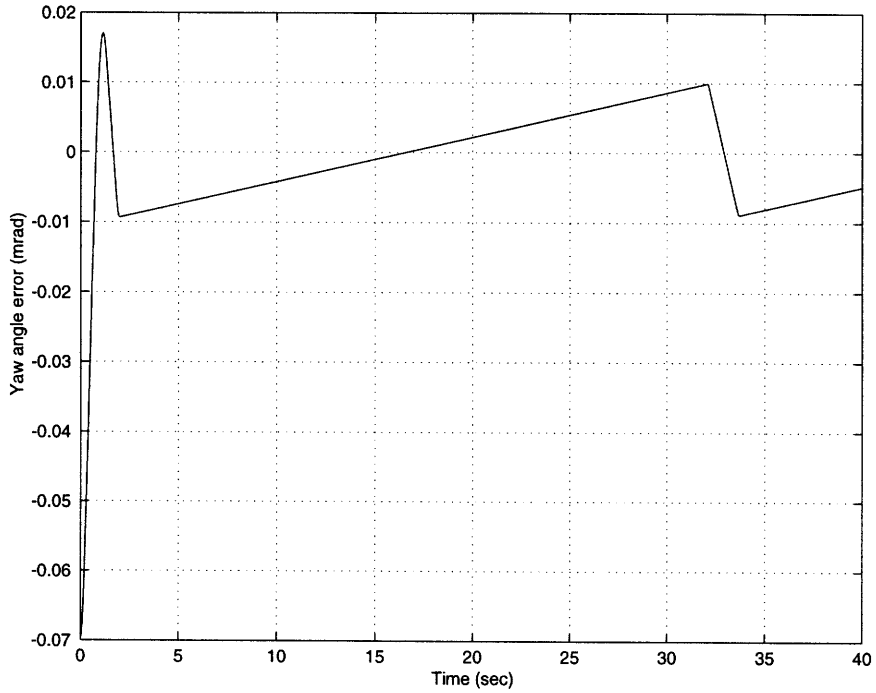

Figure 6-40: Simulated angular error response for the yaw axis using a short-pulse RLC control law for a step input of 69.7 mrad. The RLC parameters used in this simulation are $\theta_{db} = 0.01$ rad, $\theta_r = 0.0203$ rad, and $A_1 = 0.1231$. The short-pulse regions are defined through the following ranges: $\theta_{short} = \pm 0.007$, $\theta_{med} = \pm 0.04$, $\dot{\theta}_{short} = \pm 0.01$, and $\dot{\theta}_{med} = \pm 0.15$.

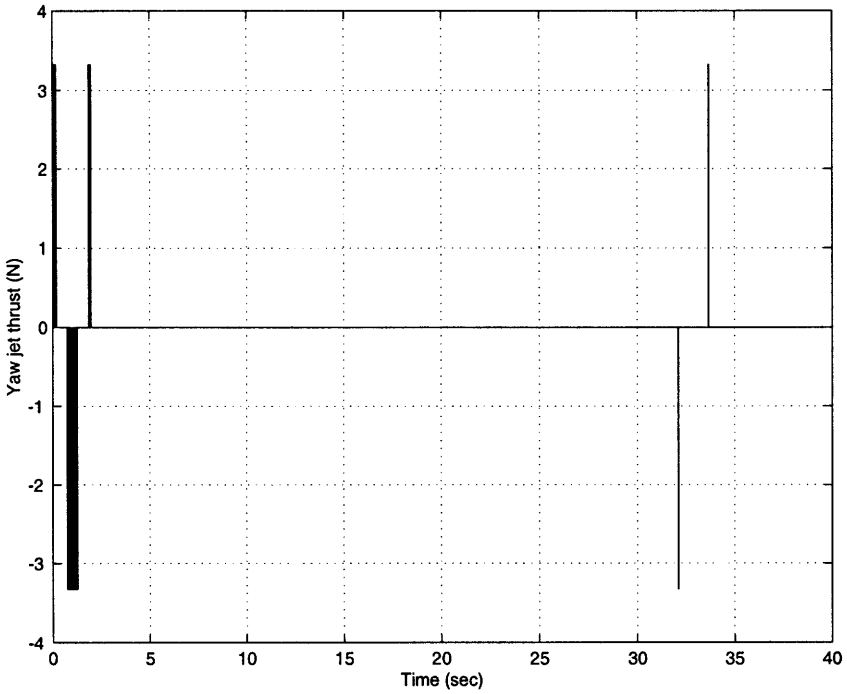

Figure 6-41: Simulated pulse commands for the short-pulse RLC control algorithm for a step input of 69.7 mrad. The RLC parameters used are $\theta_{db} = 0.01$ mrad, $\theta_r = 0.0203$ rad, and $A_1 = 0.1231$. The short-pulse regions are defined through the following ranges: $\theta_{short} = \pm 0.007$, $\theta_{med} = \pm 0.04$, $\dot{\theta}_{short} = \pm 0.01$, and $\dot{\theta}_{med} = \pm 0.15$.

for the step response using the multiple phase plane controller. In Figure 6-51 the limit cycle behavior is clearly shown in the dotted lines. Note that the limit cycle is one-sided so it has no tendency to stay in just one region of the state space. A closer look at the location where the limit cycle occurs is illustrated in Figure 6-52. In this graph we see that the limit cycle occurs inside the zero-control region of the RLC phase plane and within the bounds of the inner phase plane region. Moreover, we see a coasting behavior that indicates that the limit cycle is present in a region of the inner phase plane where the optimal control is calculated or set to be zero. This is the case due a combination of finite sampling period and a 3 ms minimum pulse width. Note that a significant amount of the sampling points occur in the case 1 category of the tracking-fuel optimal controller. The remaining sample hits occur in the no-pulsing regions (quadrants II and IV) and in the reachable region $\mathcal{R}_s$. The calculated pulse commands in the reachable region are less than 3 ms and thus will not execute a jet firing. These calculations indicate that coasting in this region is

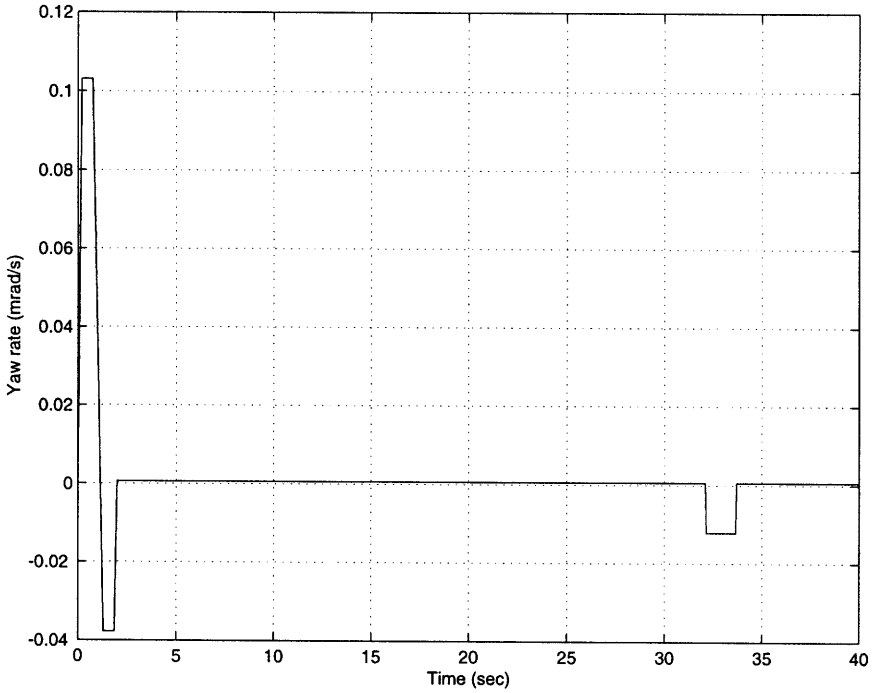

Figure 6-42: Simulated rate response for the yaw axis using a short-pulse RLC control law for a step input of 69.7 mrad. The RLC parameters used in this simulation are $\theta_{db} = 0.01$ rad, $\theta_r = 0.0203$ rad, and $A_1 = 0.1231$.The short-pulse regions are defined through the following ranges: $\theta_{short} = \pm 0.007$, $\theta_{med} = \pm 0.04$, $\dot{\theta}_{short} = \pm 0.01$, and $\dot{\theta}_{med} = \pm 0.15$.

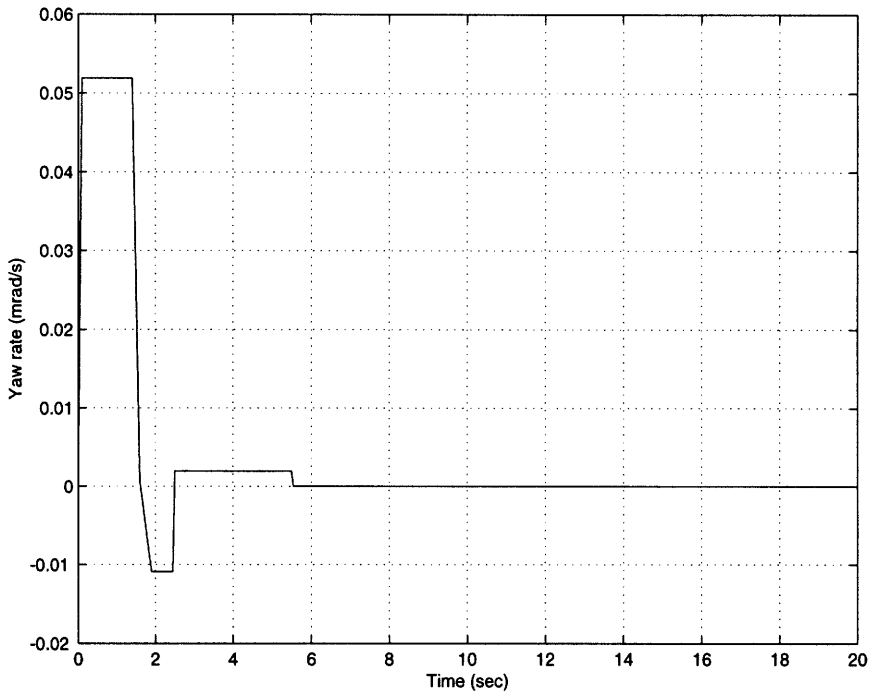

Figure 6-43: Simulated rate response for the yaw axis using a short-pulse RLC control law for a step input of 69.7 mrad. The RLC parameters used in this simulation are $\theta_{db} = 0.003$ rad,$\theta_r = 0.005$ rad and $A_1 = 0.06326$.The short-pulse regions are defined through the following ranges: $\theta_{short} = \pm 0.007$, $\theta_{med} = \pm 0.04$, $\dot{\theta}_{short} = \pm 0.01$, and $\dot{\theta}_{med} = \pm 0.15$.

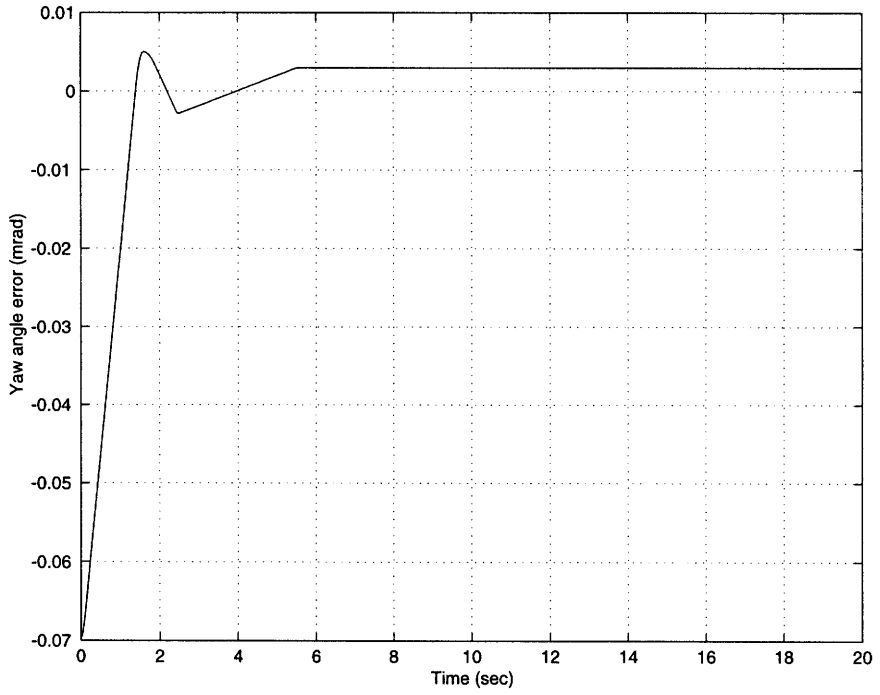

Figure 6-44: Simulated angular error response for the yaw axis using a short-pulse RLC control law for a step input of 69.7 mrad. The RLC parameters used in this simulation are $\theta_{db} = 0.003$ rad,$\theta_r = 0.005$ rad and $A_1 = 0.06326$. The short-pulse regions are defined through the following ranges: $\theta_{short} = \pm 0.007$, $\theta_{med} = \pm 0.04$, $\dot{\theta}_{short} = \pm 0.01$, and $\dot{\theta}_{med} = \pm 0.15$.

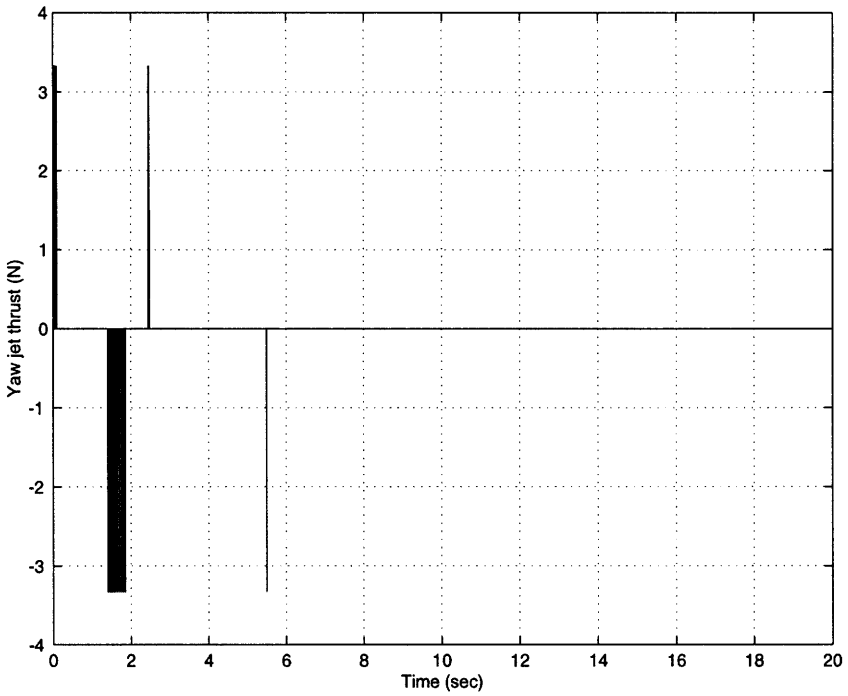

Figure 6-45: Simulated pulse commands for the short-pulse RLC control algorithm for a step input of 69.7 mrad. The RLC parameters used are $\theta_{db} = 0.003$ rad, $\theta_r = 0.005$ rad, $A_1 = 0.06326$. The short-pulse regions are defined through the following ranges: $\theta_{short} = \pm 0.007$, $\theta_{med} = \pm 0.04$, $\dot{\theta}_{short} = \pm 0.01$, and $\dot{\theta}_{med} = \pm 0.15$.

more favorable in a weighted tracking-fuel sense than firing a jet for a period of 3 ms or more. No apparent improvement over the short-pulse RLC algorithm is observed in this design.

The simulation for the design of a multiple phase plane optimal controller with RLC parameters $\theta_{db} = 0.003$ rad, $\theta_r = 0.005$ rad, and $A_1 = 0.06326$ is shown in Figures 6-53 and 6-54. Excellent steady state position accuracy is observed in the step response as well as the absence of a limit cycle. This response is seen to significantly improve the accuracy over the short-pulse response illustrated in Figure 6-44. The improvement is a substantial amount of approximately 16% in attitude steady state error reduction. The big improvement in this design comes from the control action produced by the inner phase plane control logic. This is more clearly illustrated by the phase plane trajectory in Figure 6-55. It is observed that a stable convergence to zero occurs in the state trajectory. In Figure 6-56 we show the inner phase plane control logic and the sample points falling in that region. Notice that the trajectory

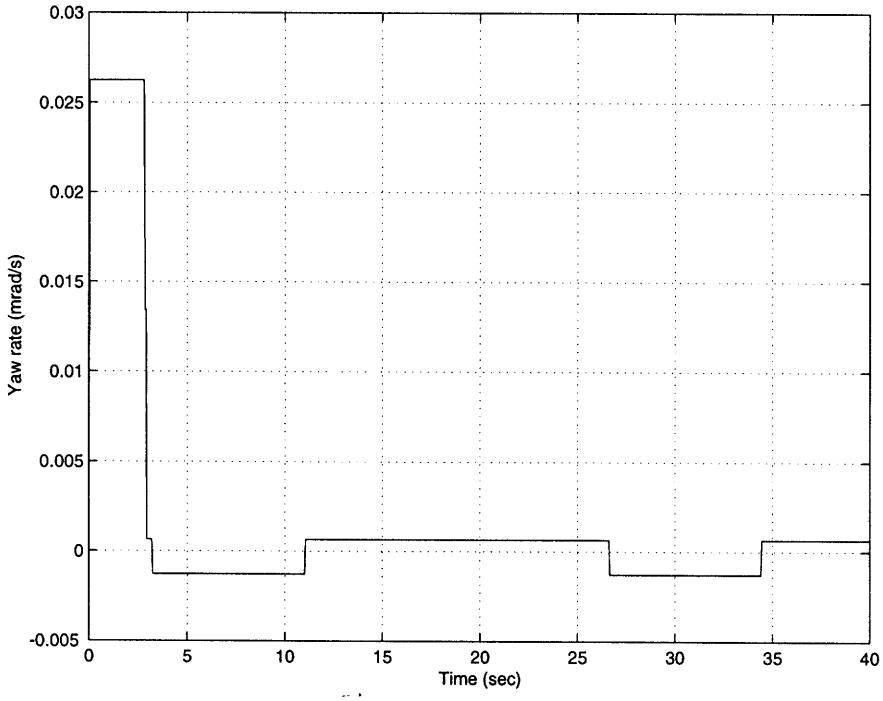

Figure 6-46: Simulated rate response for the yaw axis using a short-pulse RLC control law for a step input of 69.7 mrad. The RLC parameters used in this simulation are $\theta_{db} = 0.005$ rad, $\theta_r = 0.005071$ rad and $A_1 = 0.073159$. The short-pulse regions are defined through the following ranges: $\theta_{short} = \pm 0.007$, $\theta_{med} = \pm 0.04$, $\dot{\theta}_{short} = \pm 0.01$, and $\dot{\theta}_{med} = \pm 0.15$.

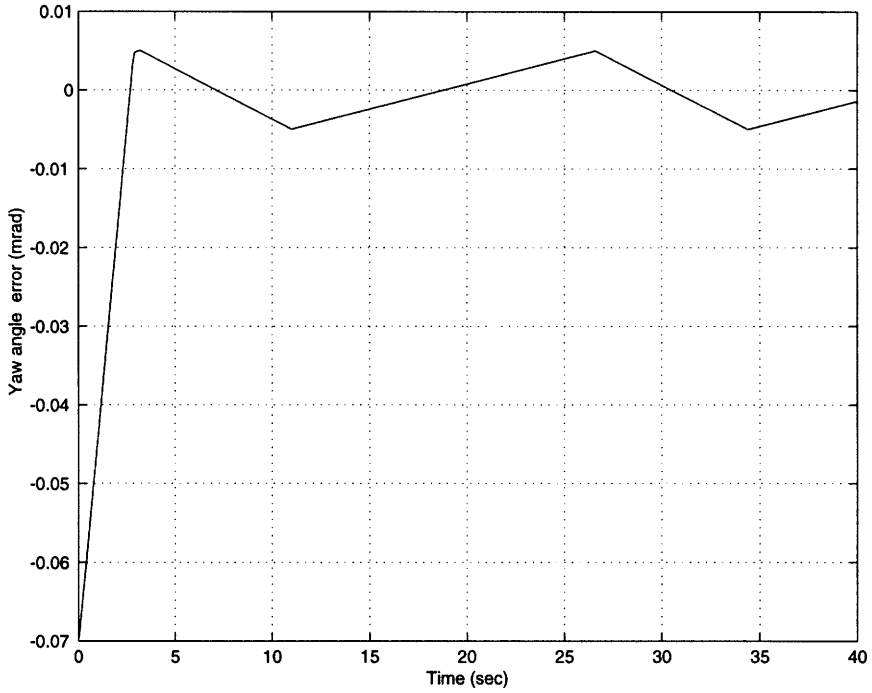

Figure 6-47: Simulated angular error response for the yaw axis using a short-pulse RLC control law for a step input of 69.7 mrad. The RLC parameters used in this simulation are $\theta_{db} = 0.005$ rad, $\theta_r = 0.005071$ rad and $A_1 = 0.073159$. The short-pulse regions are defined through the following ranges: $\theta_{short} = \pm 0.007$, $\theta_{med} = \pm 0.04$, $\dot{\theta}_{short} = \pm 0.01$, and $\dot{\theta}_{med} = \pm 0.15$.

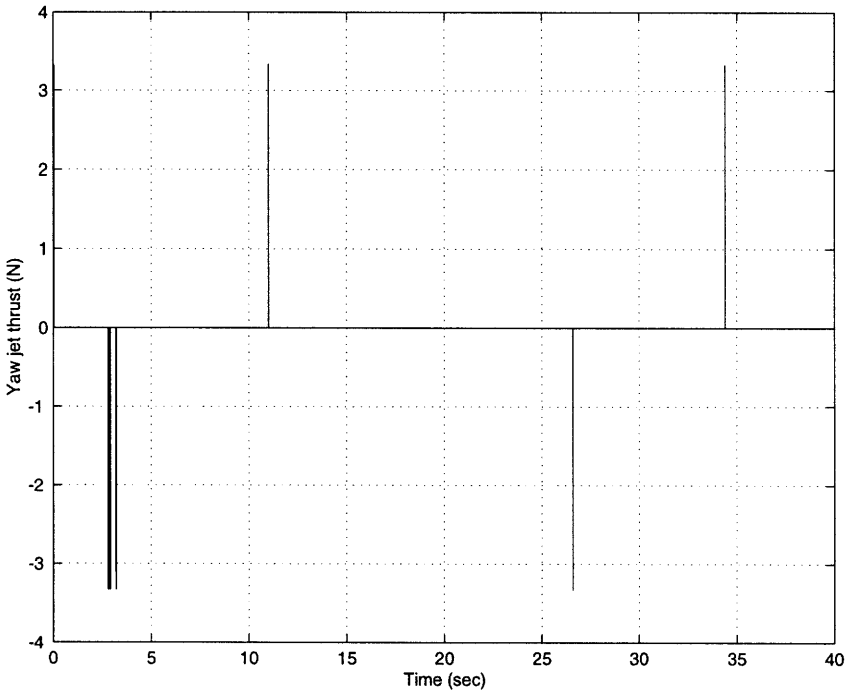

Figure 6-48: Simulated pulse commands for the short-pulse RLC control algorithm for a step input of 69.7 mrad. The RLC parameters used are $\theta_{db} = 0.005$ rad, $\theta_r = 0.005071$ rad and $A_1 = 0.073159$. The short- pulse regions are defined through the following ranges: $\theta_{short} = \pm 0.007$, $\theta_{med} = \pm 0.04$, $\dot{\theta}_{short} = \pm 0.01$, and $\dot{\theta}_{med} = \pm 0.15$.

coasts for awhile until a sample is taken inside the Case 2 region of the inner phase plane. This sample hit results in a nonzero control command given by the tracking-fuel optimal control. This combination of short-pulse RLC design with a tracking-fuel optimal controller yields the best overall performance. The increased fuel efficiency can be seen by comparing the pulse plot of Figure 6-54 with the pulse plots of the prior control designs in Section 6.3.

Note that the first set of parameters, $\theta_{db} = 0.01$ rad, $\theta_r = 0.0203$ rad, and $A_1 = 0.1231$, are not investigated for this controller since it failed to give acceptable steady state performance in all the cases of the RLC algorithm. In addition, it should be mentioned that a tracking-fuel weighting factor of $k = 0.005$ has been used for both simulated cases for comparing to the experimental design results.

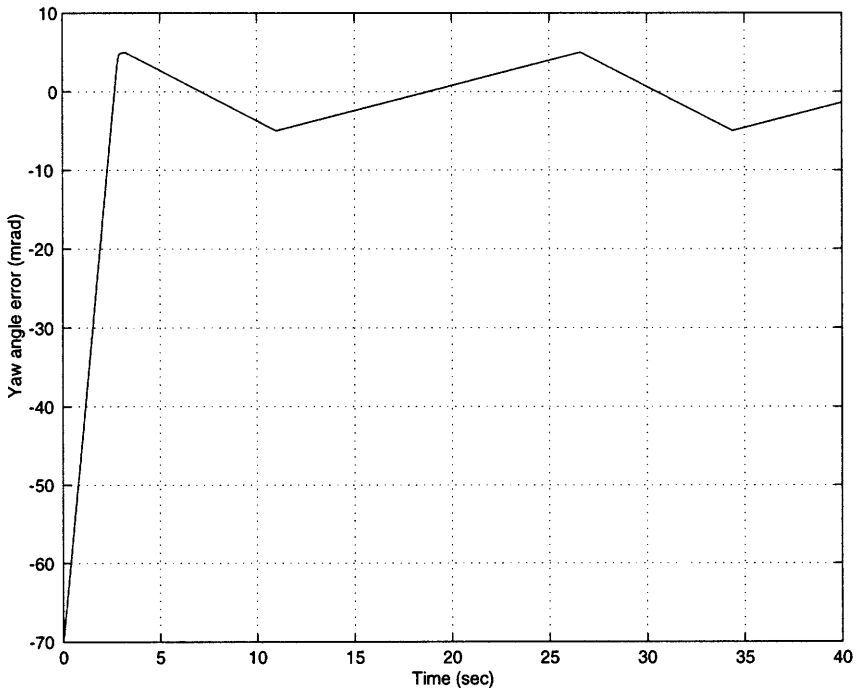

Figure 6-49: Simulated angular error response for the yaw axis using the multiple phase plane optimal control law for commanding a step input of 69.7 mrad. The RLC parameters used in this simulation are $\theta_{db} = 0.005$ rad, $\theta_r = 0.005071$ rad and $A_1 = 0.073159$. The short-pulse regions are defined through the following ranges: $\theta_{short} = \pm 0.007$, $\theta_{med} = \pm 0.04$, $\dot{\theta}_{short} = \pm 0.01$, and $\dot{\theta}_{med} = \pm 0.15$. The tracking-fuel weighting variable is $k = 0.005$.

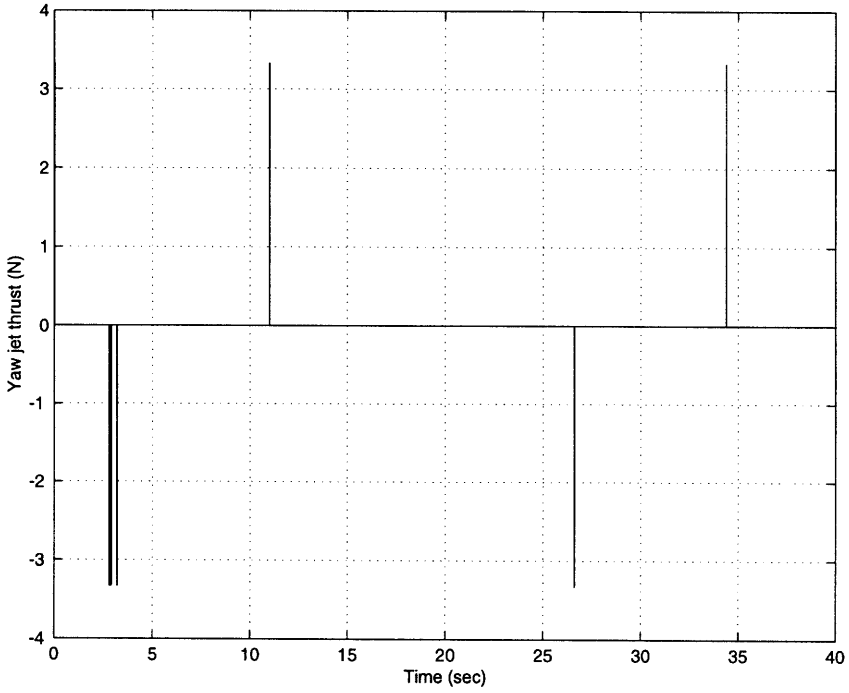

Figure 6-50: Simulated pulse commands for the multiple phase plane optimal control law for a step input of 69.7 mrad. The RLC parameters used are $\theta_{db} = 0.005$ rad, $\theta_r = 0.005071$ rad and $A_1 = 0.073159$. The short- pulse regions are defined through the following ranges: $\theta_{short} = \pm 0.007$, $\theta_{med} = \pm 0.04$, $\dot{\theta}_{short} = \pm 0.01$, and $\dot{\theta}_{med} = \pm 0.15$. The tracking-fuel weighting variable is $k = 0.005$.

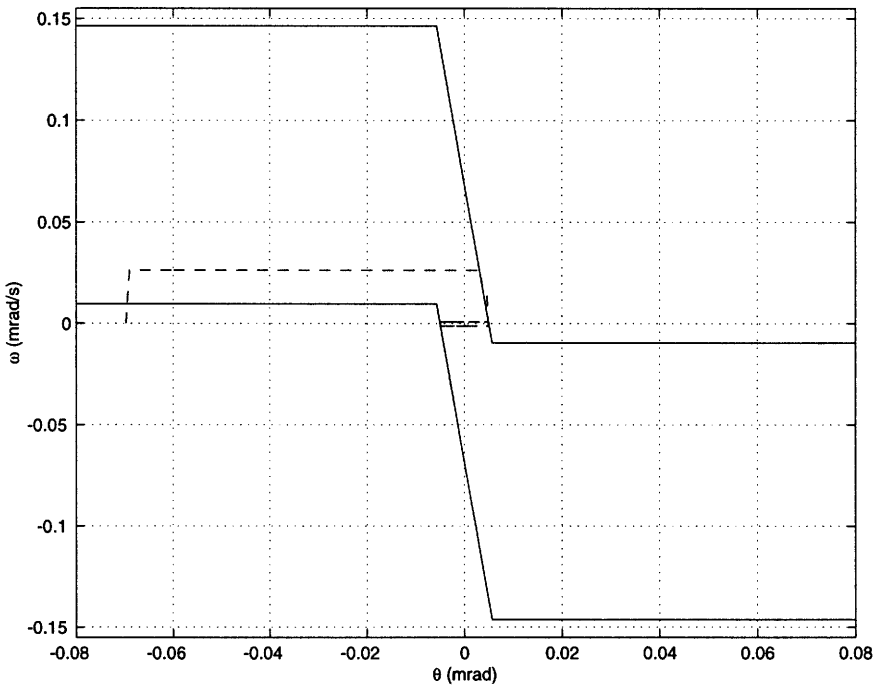

Figure 6-51: Phase plane trajectory for the 69.7 mrad step response of the multiple phase plane optimal controller with tracking-fuel weighting $k = 0.005$. The RLC parameters used are $\theta_{db} = 0.005$ rad, $\theta_r = 0.005071$ rad and $A_1 = 0.073159$. The short-pulse regions are defined through the following ranges: $\theta_{short} = \pm 0.007$, $\theta_{med} = \pm 0.04$, $\dot{\theta}_{short} = \pm 0.01$, and $\dot{\theta}_{med} = \pm 0.15$.

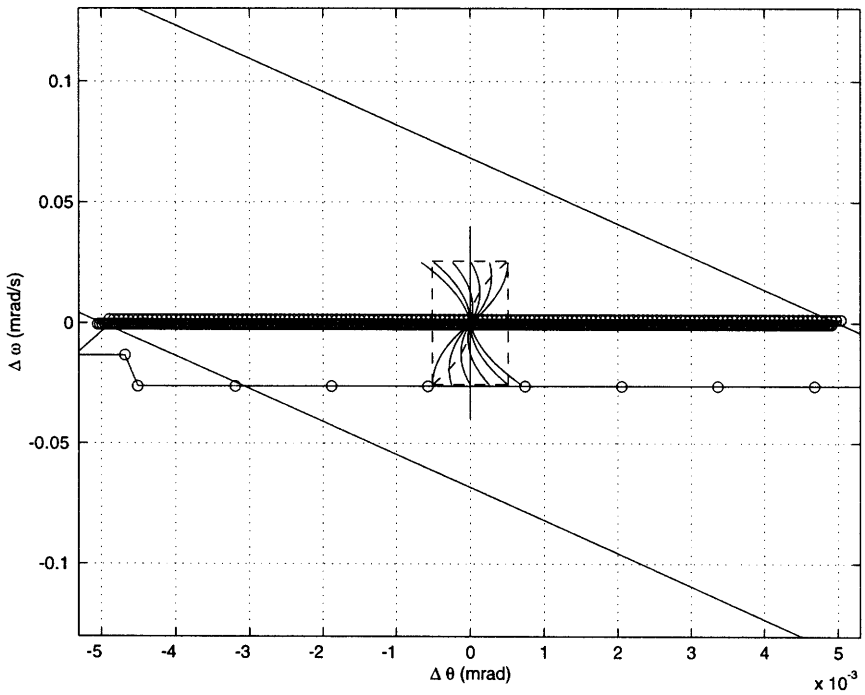

Figure 6-52: Closer look at the phase plane trajectory of Figure 6-51 inside the control boundaries corresponding to the tracking-fuel inner phase plane. Note that the axis are defined differently for this phase plane plot. The $\Delta\theta\Delta\omega$ coordinate system is used to define the tracking-fuel phase trajectories, while the $\theta - \omega$ phase space is a better description for the RLC phase plane.

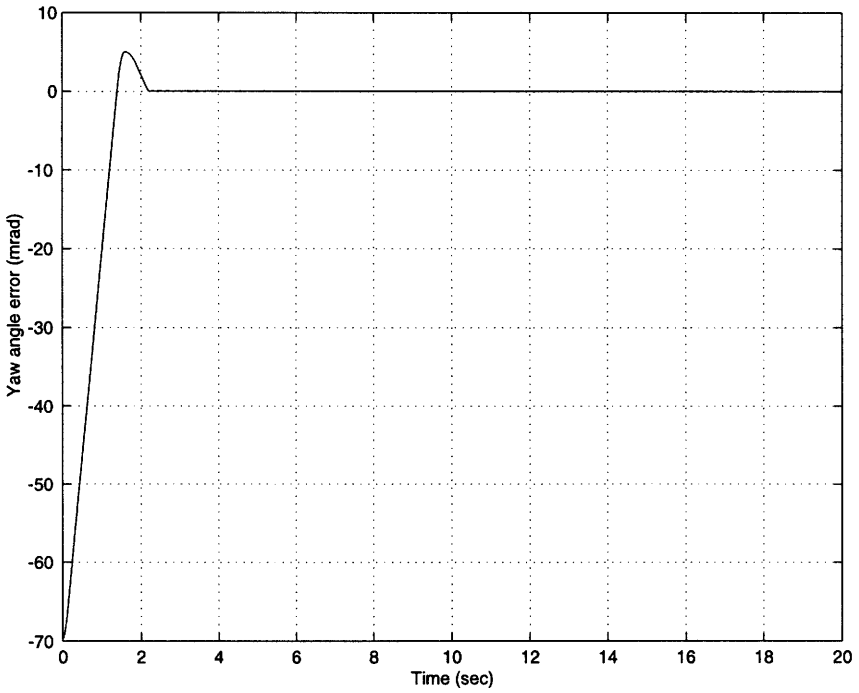

Figure 6-53: Simulated angular error response for the yaw axis using the multiple phase plane optimal controller for a step input command of 69.7 mrad. The RLC parameters used in this simulation are $\theta_{db} = 0.003$ rad,$\theta_r = 0.005$ rad and $A_1 = 0.06326$. The short-pulse regions are defined through the following ranges: $\theta_{short} = \pm 0.007$, $\theta_{med} = \pm 0.04$, $\dot{\theta}_{short} = \pm 0.01$, and $\dot{\theta}_{med} = \pm 0.15$. The tracking-fuel weighting variable is $k = 0.005$.

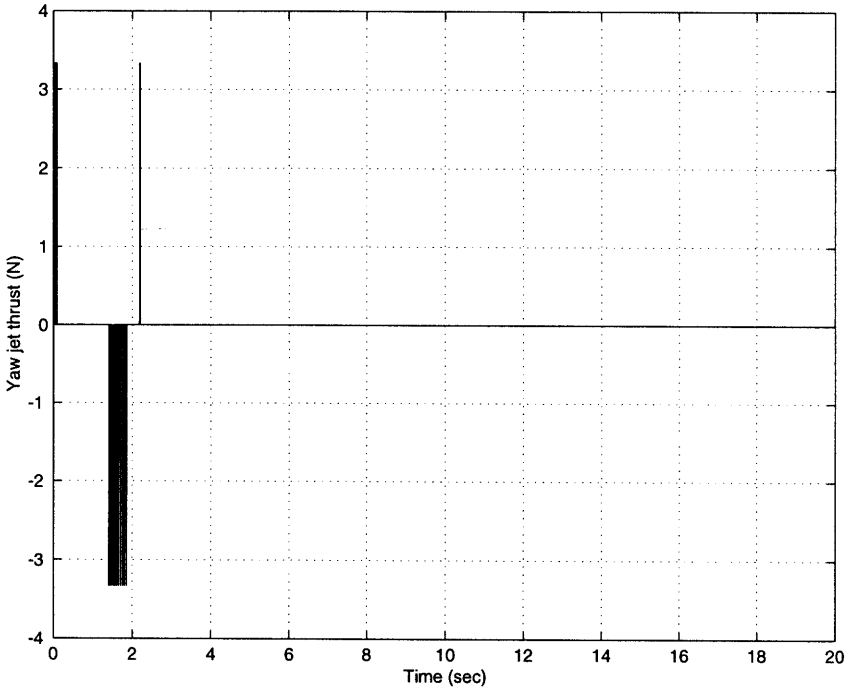

Figure 6-54: Simulated pulse commands for the multiple phase plane optimal controller for a step input command of 69.7 mrad. The RLC parameters used are $\theta_{db} = 0.003$ rad, $\theta_r = 0.005$ rad, $A_1 = 0.06326$. The short-pulse regions are defined through the following ranges: $\theta_{short} = \pm 0.007$, $\theta_{med} = \pm 0.04$, $\dot{\theta}_{short} = \pm 0.01$, and $\dot{\theta}_{med} = \pm 0.15$. The tracking-fuel weighting variable is $k = 0.005$.

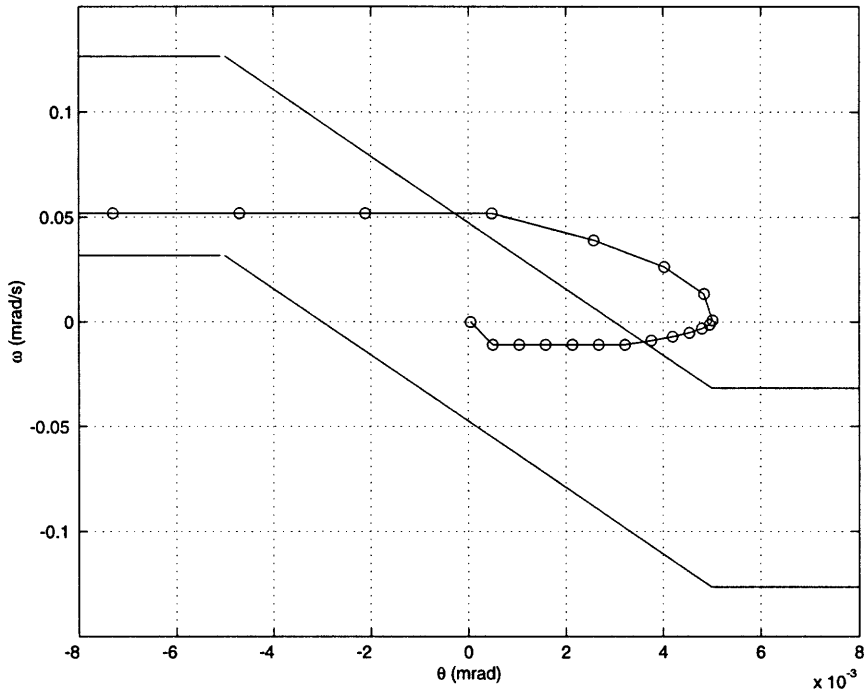

Figure 6-55: Phase plane trajectory for the 69.7 mrad step response of the multiple phase plane optimal controller with tracking-fuel weighting $k = 0.005$. The RLC parameters used are $\theta_{db} = 0.003$ rad, $\theta_r = 0.005$ rad, $A_1 = 0.06326$. The short-pulse regions are defined through the following ranges: $\theta_{short} = \pm 0.007$, $\theta_{med} = \pm 0.04$, $\dot{\theta}_{short} = \pm 0.01$, and $\dot{\theta}_{med} = \pm 0.15$.

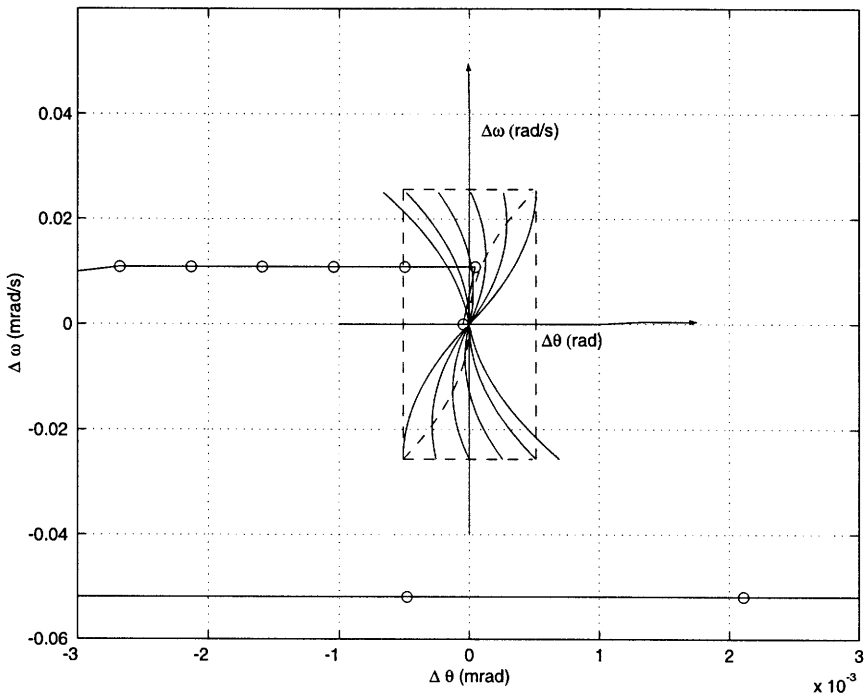

Figure 6-56: Closer look at the phase plane trajectory of Figure 6-51 inside the control boundaries corresponding to the tracking-fuel inner phase plane. Note also the change in coordinate system compared to the outer RLC phase plane.

6.4 Comparison of Experiments and Simulations

In the prior two sections of this chapter, we introduced numerous experimental results and corresponding computer simulations. We described in good detail the responses and characteristic behavior of each controller individually and how they compared to the other algorithms that are explored. We also made conclusions on the favored design in each of the two sections. We did not, however, make any remarks about the relation between the experimental results and the simulation cases that are presented. In this final section we seek to fuse together the first two sections of this chapter and gain significant insight into the dominant characteristics of the four control algorithms explored. We present the discussion as follows:

1. Compare the empirical and simulation data for the PWM/PD control scheme
2. Compare empirical and simulation data for the standard RLC algorithm
3. Compare empirical and simulation data for the short-pulse RLC scheme

4. Compare empirical and simulation data for the multiple phase plane optimal controller

6.4.1 Linear Control with Pulse-Width Modulation Scheme

By comparing the simulation plots with the empirical plots obtained from the experiments on *MicroSat* we can generally conclude that the responses appear to follow similar trends during transient behavior, but are significantly dissimilar in steady state operation. By comparing Figures 6-2 and 6-24 we see the same initial undershoot and overshoot characteristics in the empirical roll response as in the simulated response. This similarity is quite the opposite in the control of the pitch and roll axis where the empirical data indicates a much more damped response than the corresponding simulation. See Figures 6-3, 6-25, 6-7, and 6-26 for the pitch and yaw comparisons, respectively. This added damping is hypothesized to exist because of the old age of the air bearing surface that interfaces with the vehicle. The initial manufacturing tolerances are speculated to be degraded by material wear over the last two years and a half. The damping, however, is favorable in our control system because of its steady state stabilizing properites that are gained without the need to increased cost associated with extra control effort. In the case of this control algorithm, the inter-axis coupling torques do not contribute significant unmodeled dynamics so as to deviate the predicted response substantially. The empirical responses in Figure 6-3 and 6-4 show robustness to coupling torques. This also makes sense because these unmodeled dynamics, because of the high frequency content of the switching actuation, are too high in bandwidth too significantly affect the plant. The roll axis, however, because of its naturally higher bandwidth will not be as robust to similar magnitudes of coupling torques.

6.4.2 Standard RLC control algorithm

Comparing the empirical data with the simulations of the two standard RLC control scheme designs, shows a poor correlation between them. Looking first at Figures

6-9 and 6-32 we notice that the empirical result is significantly less damped. Even though both step responses limit cycle, the overshoot in the empirical step response is about 71% while in the simulation only a 10% overshoot is observed (the overshoot is automatically set by the RLC deadband). Much less discrepancy between empirical and simulated data is seen in the second RLC design. From the step responses of Figures 6-11 and 6-37 we see that the two limit cycles have much less amplitude difference than the first design case. In both these designs one could attribute the apparent discrepancy between the presented data to coupling torque components. This is a very sensible conclusion for both designs since the first design, having a wider deadband, could be more affected by coupling torques than the second design. The wider deadband would produce larger rotational errors in the axes that are not being commanded (i.e. roll and pitch axis for Figures 6-9 and 6-11) thereby increasing the effect of inter-axis torques on the commanded axis. The smaller deadband design, thus, will be less affected by disturbance torques as is observed in Figure 6-11.

6.4.3 Short-Pulse RLC control algorithm

In comparing the experimental step responses with the Matlab simulations, we observe again poor correlation. The first design, with a deadband of $\theta_{db} = 0.01$, is seen to limit cycle at faster frequency than is predicted (see Figures 6-14 and 6-40 for comparison of the first design). The second design, which has a reduced deadband of $\theta_{db} = 0.003$, is seen to limit cycle while the predicted response does not (see Figures 6-16 and 6-44 for the comparison of short-pulse RLC control design 2). This is quite an unusual case, but can be explained by accounting for the control excitation effect of unmodeled inter-axis disturbance torques. The third design with an intermediate deadband value of $\theta_{db} = 0.005$ also shows poor correlation between the empirical and predicted step responses of Figures 6-18 and 6-47. This discrepancy is also speculated to originate from oversensitivity of the RLC scheme (both the standard and the short-pulse) to torque disturbances.

6.4.4 Multiple Phase Plane Opimal Controller

For the two multiple phase plane optimal controller designs explored, some steady state discrepancies are present between the empirical and predicted step response. The first design of this control algorithm resulted in actual small limit cycles as shown in Figure 6-20, while the predicted response, shown in Figure 6-53, converges very near the origin of the state space and does not limit cycle (refer to Figure 6-55 for the phase plane of design 1). The second optimal controller design has both its empirical and predicted step response limit cycling, but these responses are still disparate in the frequency of the limit cycle. The actual step response, shown in Figure 6-22, has a significantly faster limit cycle than the simulated response of Figure 6-49

Chapter 7

Conclusions and Recommendations for Future Work

7.1 Conclusions

Various control laws for reducing the steady-state fuel consumption in spacecrafts with on-off reaction jets are considered. In specific, the aim of this thesis is to develop improved fuel efficiency for the *MicroSat* testbed at Lawrence Livermore National Laboratory (LLNL) in order to lay ground work for future small satellite missions requiring tight pointing and stabilization capabilities. Several attitude control systems from the literature are explored in this work and used to develop a combination time-fuel optimal controller and tracking-fuel optimal controller that can be modelled as multiple phase plane control logic. Three of the four approaches to attitude control taken in the thesis have either been derived in the phase plane or have been transformed to the phase plane via a change of variables or with slight algebraic manipulation. Attitude control systems for spacecraft using reaction jets based on phase plane control logic have been studied widely and are still being studied avidly by researchers and attitude control designers. These techniques have an advantage over most other design techniques. They are simply more intuitive to use and illustrate the physics of the attitude dynamics more clearly than most other methods. This is the main reason why the phase plane approach is adopted in this thesis.

Four different attitude control systems are designed and analyzed in this thesis for small satellite applications at LLNL. The first three designs are "old-hand" techniques and are implemented in the *MicroSat* test vehicle at LLNL. These consist of a proportional derivative controller with a pulse width modulator, a rate ledge controller (RLC), and a short-pulse RLC scheme. Both RLC schemes are based on a time-fuel optimal control law and serve as numerically efficient approximations to the solutions to the optimal control problem. The fourth attitude control design is a multiple phase plane control algorithm that approximates a time-fuel optimal control problem in a region of the phase plane far from the origin and a tracking-fuel optimal controller in a small region close to the origin.

The first attitude control design studied is not a phase plane control algorithm, but instead is a compensator whose output gets transformed into a corresponding pulse width jet command. This controller is used as the benchmark for this thesis. The implementation of this control law on the test vehicle shows that although it has superior disturbance rejection and fast response times, it is not suitable for small satellite applications because it is very fuel inefficient. The standard RLC design is also seen to yield high fuel expenditure due to its inability to eliminate the limit cycle sufficiently. A better design alternative is the short-pulse RLC algorithm and the multiple phase plane optimal control algorithm. Both these designs are shown to yield significant improvements in the steady state limit cycle without sacrificing the time response too much. The short-pulse RLC scheme is seen to be slightly more fuel efficient than the multiple phase plane control scheme. This, however, is in the presence of interaxis disturbance torques. In the absence of these disturbances, the multiple phase plane optimal controller stands out as being a more promising attitude control system in terms of improving both the limit cycle fuel efficiency and the pointing accuracy. Recall that the designer by choosing the time weight λ and the fuel weight k in the corresponding designs has the flexibility to increase or decrease the importance of fast response or fuel efficiency in the system performance. Awareness of the effect of the fuel weighting factor, k, on the steady-state error of the system response is also of primary importance when shaping the desired system

performance.

7.2 Recommendations for Future Work

Two important practical issues have arisen from the results presented in this thesis that need further study before the kind of phase plane control systems developed in this thesis are taken to next level. One issue concerns the selection of the deadband value for the RLC based control algorithms and its effect on actual system performance. The other, equally as significant, is the control of a free rotational mass in the presence of friction in an earth-based testbed or disturbance torques in a spaced-based vehicle. The first issue relates to the "fuel-bump" phenomena that is briefly mentioned in the body of the thesis. The fuel bump is referred to as when a RLC or any other type of phase plane-like deadband has a value such that when it is decreased a subsequent decrease in fuel consumption follows. The best choice for the deadband that minimizes the fuel expenditure can be found from looking at how the fuel consumption varies as a function of the deadband. Currently this optimization of the deadband, if done at all, can only be done empirically. It would be of instrumental help in attitude control applications if a mathematical model could be developed for describing this fuel bump phenomena.

The second main issue identified in this thesis concerns the further development of disturbance rejection techniques that deal with linear attitude dynamics and nonlinear actuation. The use of estimators certainly would be a feasible option in both data filtering and disturbance estimation. Estimation in fuel optimal attitude control of spacecraft could lead to many improved control designs that are currently nonexistent. In addition, techniques for analyzing and designing attitude control systems for highly coupled loops would also open the doors for further improvement of the steady state limit cycle.

A further step in refining the bang-bang performance of attitude control systems would entail the use of a model based on the flexible body modal equations instead of Euler's equation of rigid body rotation. The presence of flight instrumentation

on-board spacecraft will require complete control of the modes of vibration in order to fully model the interaction of the sensors with the actuation of the spacecraft. This thesis is by far not the last word on the improving the fuel inefficient steady state limit cycle behavior specific to spacecraft that use on-off reaction jets. Many promising alternatives are still left to be found.

Appendix A

Calculation of Standard RLC Parameters From Minimum Time-Fuel Control Law

A direct comparison of Figures 3-3 and 3-5 shows a clear similarity between the shapes, and thus the functionality, of the RLC phase plane and the continuous-time minimum time-fuel phase plane switching curves. Superimposing the two phase planes on the same plot gives the schematic shown in Figure A-1.

The variables defined in Figure A-1 will be the basis for the formulation of the mathematical analogy between the minimum time-fuel control law and the RLC. The optimal switching curves shown in Figure A-1 (also in Figure 3-3) are given by the following expressions

$$\left.\begin{array}{lcll} \phi & = & -\frac{1}{2}\dot{\phi}^2 + \phi_{db} & \text{A-B} \\ \phi & = & \frac{1}{2}\dot{\phi}^2 - \phi_{db} & \text{E-F} \\ \phi & = & \frac{\lambda+4}{2\lambda}\dot{\phi}^2 + \phi_{db} & \text{B-C} \\ \phi & = & -\frac{\lambda+4}{2\lambda}\dot{\phi}^2 - \phi_{db} & \text{D-E} \end{array}\right\} \qquad \text{(A.1)}$$

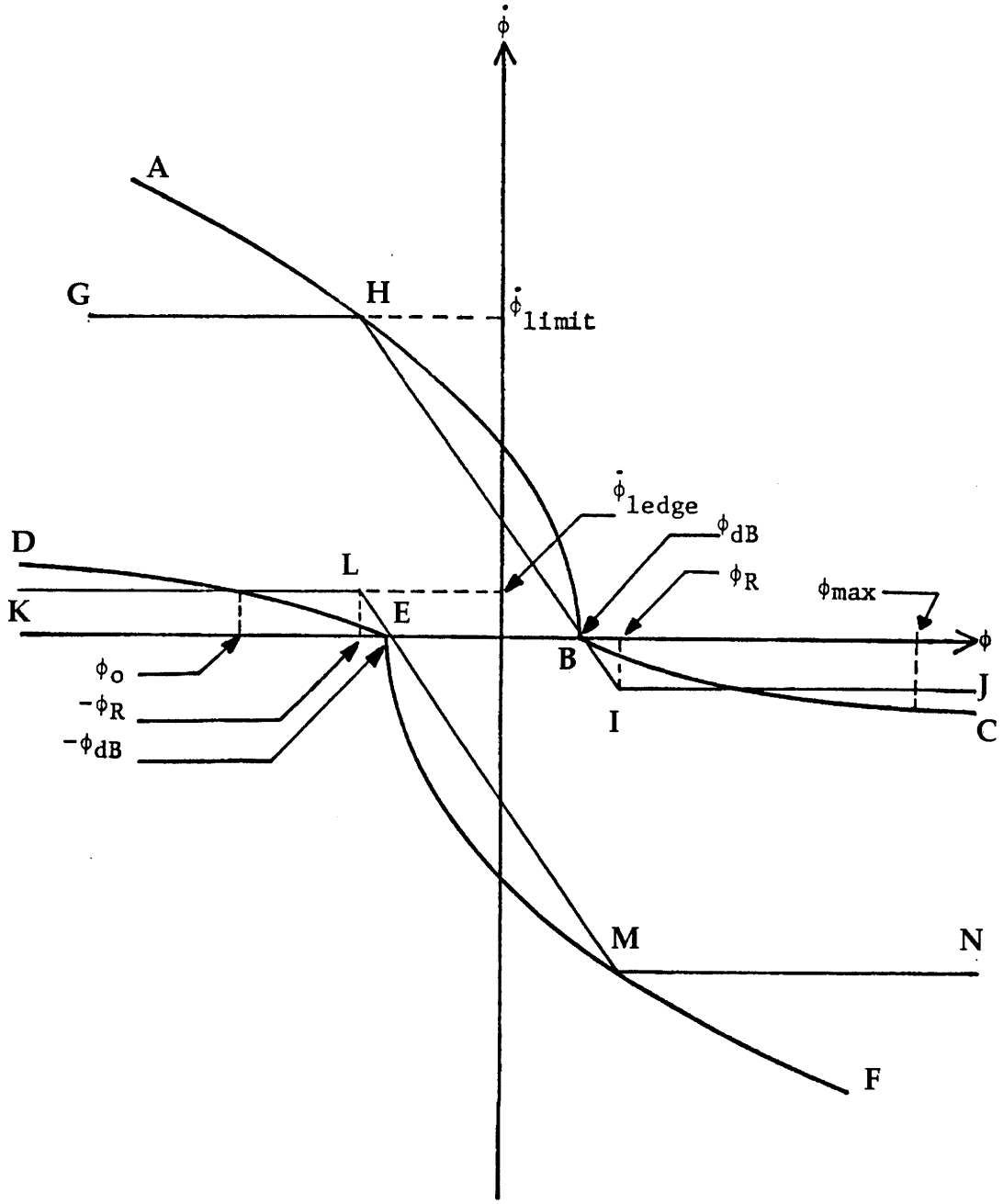

Figure A-1: Diagram showing the similarity of the RLC phase plane to the continuous-time optimal time-fuel switching curves. This schematic is taken from Weisenberg [20].

The RLC, which is defined by curves H-B and L-M in Figure A-1, can be described by

$$\phi + A_1\dot{\phi} = \phi_{db} \qquad \text{H-B} \tag{A.2}$$

$$\phi + A_1\dot{\phi} = -\phi_{db} \qquad \text{L-M} \tag{A.3}$$

Using (A.1), (A.2), (A.3) and Figure A-1, it can be shown that the best RLC approximation to a specific set of minimum time-fuel switching curves is given by

$$A_1 = \sqrt{(\phi_{\mathbf{r}} + \phi_{\mathbf{db}})/\mathbf{2}} \tag{A.4}$$

$$\dot{\phi}_{limit} = \sqrt{2(\phi_r + \phi_{db})} \tag{A.5}$$

$$\dot{\phi}_{ledge} = (\phi_r - \phi_{db})\sqrt{2/(\phi_r + \phi_{db})} \tag{A.6}$$

if and only if the value chosen for ϕ_r minimizes the mean square error, $e = (\dot{\phi}_{optimal} - \dot{\phi}_{rlc})^2$, between the RLC and the corresponding optimal switching curves. To determine this specific value for ϕ_r, the following iterative algorithm is performed:

Initialization:

$$\phi_0 = (-\phi_{db} - \phi_{max})/2 \tag{A.7}$$

$$\phi_r = (-a_1 + \sqrt{a_1^2 - 4a_0})/2 \tag{A.8}$$

$$K_{1d} = k_2\sqrt{\lambda/(\lambda + 4)} \tag{A.9}$$

where

$$a_0 = \phi_{db}^2 + \lambda(\phi_0 + \phi_{db})\phi_{db}/(\lambda + 4) \tag{A.10}$$

$$a_1 = -2\phi_{db} + \lambda\frac{(\phi_0 + \phi_{db})}{(\lambda + 4)} \tag{A.11}$$

$$k_2 = 4(\phi_{max} - \phi_{db})^2 \tag{A.12}$$

Iteration:

$$\left.\begin{aligned}
K_1(k+1) &= \frac{(16/3)(\phi_r(k)-\phi_{db})(\phi_{max}-\phi_{db})^{3/2}-(32/15)(\phi_r(k)-\phi_{db})^{5/2}}{\sqrt{\phi_r(k)+\phi_{db}}} \\
B(k) &= \frac{(\phi_r(k)+\phi_{db})^{1/2}-0.5(\phi_r(k)+\phi_{db})^{-1/2}(\phi_r(k)-\phi_{db})}{\phi_r(k)+\phi_{db}} \\
C(k) &= \frac{2.5(\phi_r(k)-\phi_{db})^{3/2}(\phi_r(k)+\phi_{db})^{1/2}}{\phi_r(k)+\phi_{db}} \\
D(k) &= \frac{0.5(\phi_r(k)+\phi_{db})^{-1/2}(\phi_r(k)-\phi_{db})^{5/2}}{\phi_r(k)+\phi_{db}} \\
K_1' &= \tfrac{16}{3}(\phi_{max} - \phi_{db})^{3/2}B(k) - \tfrac{32}{15}[C(k) - D(k)] \\
\Delta\phi_r(k) &= \frac{K_{1d}-K_1(k)}{K_1'(k)} \\
\phi_r(k+1) &= \phi_r(k) + \Delta\phi_r(k)
\end{aligned}\right\} \tag{A.13}$$

The value found for ϕ_r from this iteration is substituted into the expressions for A_1, ϕ_{limit}, and ϕ_{ledge} to give an RLC phase plane that well approximates the optimal time-fuel solution characterized by the weighting factor λ. Therefore, given a value for λ, ϕ_{db}, and ϕ_{max}, the value of ϕ_r can be computed and used to determine the parameters that characterize the RLC as seen when iterating for ϕ_r.

Once a desired RLC phase plane is designed the block diagram of Figure 3-12 can be used for implementation in a computer environment or in simulation. Note that ϕ_r acts as limiting value for ϕ in the position loop while A_1 is a rate feedback gain. ϕ_{db} is just the deadzone selected around the commanded attitude, ϕ_c. Furthermore, $\pm\dot{\phi}_{lim}$ is the minimum allowable rate, $\pm\dot{\phi}$, by the RLC controller before entering the region $u = 0$, while $\pm\dot{\phi}_{ledge}$ is the maximum.

Bibliography

[1] Michael Athans. Time and fuel optimal attitude control. Technical Report 22G-9, MIT, Lincoln Laboratory, Lexington, Mass, 1963.

[2] Vladimir A. Chobotov. *Spacecraft Attitude Dynamics and Control.* Krieger, Malabar, Fl, 1991.

[3] Robert N. Clark, P. Dumas, and D.C. Fosth. Scheme to improve limit-cycle performance of an attitude control system. *Journal of Spacecraft and Rockets*, 12(4):253–254, April 1975.

[4] Michael A. Floyd. Single-step optimal control of the rpl experiment. *Rocky Mountain Guidance and Control Conference*, February 1985.

[5] George W. Freeman. Limit-cycle efficiency of on-off reaction control systems. Technical report, Boeing Airplane Company, Seattle, WA.

[6] Sir William Rowan Hamilton. Elements of quaternions. 1866.

[7] Peter C. Hughes. *Spacecraft Attitude Dynamics.* J. Wiley & Son, Inc., New York, New York, 1986.

[8] David G. Hull. Conversion of optimal control problems into parameter optimization problems. *Journal of Guidance, Control, and Dynamics*, 20(1):57–60, January/February 1997.

[9] Sanguk Lee and J.E. Cochran Jr. Orbital maneuvers via feedback linearization and bang-bang control. *Journal of Guidance and Control*, 20(1):104–110, January/February 1997.

[10] Frank L. Lewis and Vassilis L. Syrmos. *Optimal Control.* John Wiley & Sons, Inc., Toronto, Canada, second edition, 1995.

[11] Gordon D. Niva. The use of quaternions with an all-attitde imu. *Annual Rocky Mountain Guidance and Control Conference*, January/February 1982.

[12] William H. Press, B.P. Flannery, S.A. Teukolsky, and W.T. Vetterling. *Numerical Recipes in C: The Art of Scientific Computing.* Cambridge University Press, Reading, Massachusetts, second edition, 1992.

[13] David Lawrence Quam. *A No Limit-Cycle Digital Computer Algorithm for Pulsed Attitude Control of a Flexible Spacecraft.* PhD thesis, University of Washington, July 1975.

[14] Singiresu S. Rao. *Engineering Optimization: Theory and Practice.* Wiley Interscience, New York, NY, 1996.

[15] Stanley W. Shepperd. Quaternion from rotation matrix. *Journal of Guidance and Control*, 2(3):223–224, May/June 1978.

[16] Maxwell Smith. *Aviation Fuels.* G.T. Foulis & Co. LTD., Henley-on-Thames-Oxfordshire, England, 1970.

[17] Richard A. Spurrier. Comment on singularity free extraction of a quaternion from a direction cosine matrix. *Journal of Spacecraft*, 15(4):255, July/August 1978.

[18] III Thomas A.W. Dwyer. Exact nonlinear control of large angle rotational maneuvers. *IEEE Transactions on Automatic Control*, AC-29(9):769–774, September 1984.

[19] III Thomas A.W. Dwyer. Bandwidth-limited robust nonlinear sliding control of pointing and tracking maneuvers. *American Control Conference*, 1989.

[20] David Marc Weisenberg. A comparative study of various approaches to the design of on-off thruster attitude control systems. Master's thesis, Mechanical Engineering Dept., Massachusetts Institute of Technology, June 1987.

[21] Larry R. White. Some optimal considerations in attitude control systems. Master's thesis, Electrical Engineering Dept., Auburn University, December 1973.

[22] Bong Wie and Peter M. Barba. Quaternion feedback for spacecraft large angle maneuvers. *AIAA, Dynamics Specialist Conference*, pages 373–380, May 1984.